Sound Attenuation Using MEMS Fabricated Acoustic Metamaterials

by

William Nicholas Yunker

A thesis submitted to the Graduate Faculty of
Auburn University
in partial fulfillment of the
requirements for the Degree of
Master of Science

Auburn, Alabama
May 6, 2012

Keywords: MEMS, acoustic metamaterial, Helmholtz resonator, MEMS gyroscope

Approved by

George T. Flowers, Co-Chair, Professor of Mechanical Engineering
Robert N. Dean, Co-Chair, Associate Professor of Electrical and Computer Engineering
Jeffrey Suhling, Professor and Chair of Mechanical Engineering

Abstract

Unlike traditional rotational gyroscopes, MEMS gyroscopes use a vibrating proof mass rather than a rotational mass to sense changes in angular rate. They are also smaller and less expensive than traditional gyroscopes. MEMS gyroscopes are known to be susceptible to the effects of acoustic noise, in particular high frequency and high power acoustic noise. Most notably this has been proven true in aerospace applications where the noise can reach levels in excess of 120 dB and the noise frequency can reach levels in excess of 20 kHz. The typical resonant frequency for the proof mass of a MEMS gyroscope is between 3 and 20 kHz. High power, high frequency acoustic noise can disrupt the output signal of the gyroscope to the point that the output becomes unreliable.

In recent years, a large amount of research has focused on the fascinating properties found in metamaterials. A metamaterial is an artificially fabricated device or structure that is built to produce desired material responses that can either mimic known behaviors or produce responses that do not occur naturally in materials found in nature. Acoustic metamaterials in particular have shown great promise in the field of sound attenuation. This thesis proposes a method to limit the signal degradation of the MEMS gyroscope in the presence of high power, high frequency acoustic noise by using a new acoustic metamaterial in the form of a one-dimensional array of Helmholtz resonators. The Helmholtz resonators are fabricated on a silicon wafer using standard MEMS manufacturing techniques and are designed to attenuate sound at the resonant frequency of the gyroscope proof mass. The resonator arrays were diced from the

silicon wafer in one inch squares and assembled into a box open on one end in a manner to attenuate sound on all sides of the gyroscope, and to seal the gyroscope inside the box. The acoustic metamaterial was tested in acoustically harsh environments and was found to successfully attenuate sound as much as 18 dB. This attenuation is in the form of a notch filter at and around 14.5 kHz, which was the target frequency of attenuation. The notch filter attenuation occurred over a 700 Hz frequency band with 18 dB being the largest attenuation in the band.

Acknowledgments

The author would like to thank Dr. George T. Flowers and Dr. Robert Dean for their wisdom, guidance, and assistance throughout every stage of this work. Additionally, the author would also like to express his gratitude to Colin Stevens and Pregassen Soobramaney for their assistance in fabrication and testing. The love and support of my family and friends have given me the means and drive to succeed in life, but above all I would like to thank my wife, Laura, for being my inspiration, my role model, and my best friend.

Table of Contents

List of Tables

List of Figures

List of Symbols

a_c	Coriolis Acceleration
Ω	Angular Rate
v_r	Radial Velocity
F_c	Coriolis Force
ω_x	Resonant Frequency of Drive Mode
ω_y	Resonant Frequency of Sense Mode
ξ	Damping Ratio
F_x	Amplitude of Oscillatory Force
x_0	Drive Mode Vibration Amplitude
y_0	Sense Mode Vibration Amplitude
C_x	Damping Along Drive Axis
C_y	Damping Along Sense Axis
ω_d	Drive Frequency
Q	Quality Factor
ε	Permittivity
μ	Permeability
n	Refractive Index
ρ_d	Dynamic Density
β	Compressibility

B	Bulk Modulus
ρ_{eff}	Effective Mass Density
n_a	Acoustic Refractive Index
V	Cavity Volume
L	Neck Length
S	Neck Cross-sectional Area
ω_0	Resonant Frequency of Resonator in rad/s
L'	Neck Effective Length
s	Condensation
k	Stiffness
f	Resonant Frequency in Hz

Chapter 1: Introduction

In recent decades, the advent of microelectromechanical systems (MEMS) technology has allowed for the construction of smaller, more efficient, and cheaper sensor technology. MEMS are devices that unite mechanical systems with electrical components within the scale of 1mm to 1μm [1]. One of the more complicated sensors built using MEMS fabrication techniques is the MEMS gyroscope. Unlike traditional rotational gyroscopes, the MEMS gyroscope uses a vibrating proof mass, which senses angular rotation by measuring the Coriolis effect. MEMS gyroscopes are used in all ranges of environments from extremely harsh to reasonably benign. Some of the harsher environments include: extreme heat or cold, intense vibrations, mechanical shock, and high frequency, high power acoustic noise. This work examines the environment of high frequency, high power acoustic noise to propose a solution to mitigate some of the deleterious effects on gyroscopes present in such environments.

To achieve this end, an acoustic metamaterial was designed and fabricated using MEMS fabrication techniques with the intent of using the attractive properties of the acoustic metamaterial to attenuate noise at the resonant frequency of the MEMS gyroscope. An acoustic metamaterial derives its unique properties through the artificial fabrication of resonators into each unit cell of material. The dimensions and resonant frequency of these resonators can be designed to any specifications.

The acoustic metamaterial created for this experiment consists of a one-dimensional array of Helmholtz resonators fabricated in a silicon wafer. The dimensions of each resonator are designed to attenuate sound at a frequency of 14.5 kHz. MEMS gyroscopes typically have a proof mass resonant frequency between 3 kHz and 20 kHz. MEMS fabrication techniques allow

for the creation of thousands of resonators on a single one inch square piece of silicon. The silicon wafer is diced into one inch squares, and these resonator squares are assembled into a box that is sealed around the gyroscope to lower the sound power level reaching the gyroscope at the desired resonant frequency.

1.1 Motivations and Objectives

The main difference between the traditional rotational gyroscope mentioned and the MEMS gyroscope is the way that the proof mass moves. Rotational gyroscopes use a rotating mass to sense changes in angular rotation, while MEMS gyroscopes use a vibrating proof mass to sense the sinusoidal Coriolis force that is induced along the sense axis of the gyroscope in response to an orthogonal angular rate input and the oscillation of the proof-mass. The advent of MEMS gyroscopes showed significant decreases in cost and size. These achievements came with the downfall of making the sensor more complicated in design and more sensitive to effects such as vibration, temperature, mechanical shock, and acoustic noise. MEMS gyroscopes are known to be highly susceptible to the effects of high frequency and high power acoustic noise. Since MEMS gyroscopes are used in a variety of applications from video game systems to missile guidance systems, it is desirable to investigate any options that could make the MEMS gyroscope more reliable in every environment.

The purpose of this thesis is to determine if an acoustic metamaterial composed of an array of Helmholtz resonators fabricated at MEMS size using MEMS fabrication techniques can be effective in attenuating sound at or near the resonant frequency of a MEMS gyroscope proof mass. There has been little to no research performed on the effectiveness of Helmholtz

resonators on the micro scale. This thesis will show how effective MEMS size Helmholtz resonators are at attenuating acoustic noise.

1.1.1 Review of Previous Works Regarding MEMS Gyroscopes

This section will present a review of research on the subject of MEMS gyroscopes and their susceptibility to high power, high frequency acoustic noise, and other related research on MEMS gyroscopes.

Dean *et al.* proved that the MEMS gyroscopes are susceptible to vibrations at or near the resonant frequency of the proof mass in the medium of air. To mitigate these effects, a passive low-pass filter was fabricated in the printed circuit board [2]. Furthermore, Yunker *et al.* proved that MEMS gyroscopes are susceptible to acoustic noise at or near the resonant frequency of the proof mass in the medium of water [3]. The previous study by Dean was extended with the use of an active filter composed of electrostatic actuators. It was found that the active filter was more successful in mitigating the effects of vibration on the output of the MEMS gyroscope than the passive filters previously used [4].

Dean *et al*. proved that high frequency, high power acoustic noise has a dramatic impact on the performance of MEMS gyroscopes. It was determined that the noise floor of a gyroscope in the presence of high power acoustic noise, near 100 dB, increased as a function of acoustic noise power and angular rate. Dean *et al* also determined that as the acoustic noise power level approached 130 dB, the noise floor of the sensor became so erratic that the data from the sensor became unusable [5]. In a continuation of this study, Castro found that the gyroscope could be

protected from the noise sufficiently to prevent complete corruption of the gyroscope output by surrounding the gyroscope with different types of acoustic foams [6].

Burch *et al*. found that microfibrous cloth could be used to dampen both vibrations and acoustic noise in a MEMS gyroscope assembly. The cloth was composed of a 10% sintered nickel material and was stacked between the PCB and an aluminum fixture. The gyroscope was mounted on the PCB and testing was performed in an acoustic chamber. The output of the MEMS gyroscope was monitored, and it was determined that the noise peak of the MEMS gyroscope significantly decreased with the addition of the cloth from the same test with no cloth [7].

1.1.2 Review of Previous Works Regarding Acoustic Metamaterials

This section will provide a review of research on the subject of acoustic metamaterials, specifically, acoustic metamaterial research in relation to sound attenuation.

Smith *et al.* verified experimentally the negative refractive index, which was an array of split ring resonators fabricated in a periodic medium. The split ring resonators tested successfully for negative values for both permittivity and permeability [8].

The first acoustic metamaterial was proposed by Liu *et al.* which they called locally resonant sonic materials. They fabricated sonic crystals to act as resonant structures within a composite medium. The locally resonant sonic materials proved to be effective only in small frequency bandwidths [9]. Later, Fang *et al.* proposed a new type of acoustic metamaterial which consisted of a one-dimensional array of Helmholtz resonators. The new acoustic metamaterial

was shown experimentally to have a negative dynamic effective modulus. This device was tested ultrasonic frequencies in the range of 31 to 35 kHz [10].

Yang *et al.* successfully demonstrated the creation of a new form of acoustic metamaterial that was effective over a large bandwidth, from 50-1000 Hz. The acoustic metamaterial they fabricated consisted of a thin elastic membrane fixed by a plastic grid. The device proved successful in attenuating acoustic noise and was reported to have attenuated an average of over 40 dB in the 50-1000 Hz frequency range [11].

1.1.3 Review of Previous Works Regarding Helmholtz Resonators

This section will provide a review of research on the subject of Helmholtz resonators and how the resonant frequency of the Helmholtz resonators is best calculated.

Panton and Miller developed a closed form expression of the resonant frequency in a cylindrically shaped Helmholtz resonator. They also determined that the analysis of the resonator is only valid when the length dimension of the resonator is 1/16 the wavelength of the present acoustic noise, not the ¼ that had been quoted in previous research [12].

Chen *et al*. had significant success at acoustic noise attenuation in a duct through the use of Helmholtz resonators. The Helmholtz resonators in this experience were macro-sized with a neck area of .79 cm^2 and were tested only at low frequencies, with the resonant frequency of the resonators at 250 and 500 Hz. The results showed an improvement of 28 dB transmission loss at the designed resonant frequency with the application of the resonators [13].

Han and Rhim conducted an experiment with Helmholtz resonators aimed at lowering the overall noise level in a slim-type optical disk drive (ODD). They used smaller machined arrays

of Helmholtz resonators with a neck diameter between 1 and 1.5mm and tested at a higher frequency with resonant frequencies of 2, 3, and 4 kHz. The most effective test of the arrays of Helmholtz resonators yielded a sound pressure level (SPL) decrease of 1.5 dB [14].

1.2 Thesis Organization

Chapter two is composed of background information on three relevant topics to this thesis. This first topic is a brief history and discussion of traditional gyroscopes and MEMS gyroscopes. The MEMS vibratory gyroscopes are discussed and analyzed in detail along with a brief introduction to MEMS fabrication techniques, the Coriolis effect, and applications of MEMS gyroscopes. The second topic is an introduction to the field of metamaterials. Specifically, electromagnetic metamaterials, optical metamaterials, acoustic metamaterials, and their applications are discussed in detail. The third topic introduces Helmholtz resonators, which are the building blocks of the acoustic metamaterial designed and fabricated for this thesis. The Helmholtz resonator design and modeling is discussed, and the resonant formula for the Helmholtz resonator used in testing for this thesis is derived. The chapter concludes with a section on the applications of Helmholtz resonators in industry and research.

Chapter three describes the process of design and fabrication of the acoustic metamaterial resonator box and the control box. Each step in the fabrication process is outlined and photographed. This section illustrates the construction of each test box from a silicon wafer through the photolithography, mask exposure, etching, anodic bonding, and dicing of the wafer. The process for assembling the boxes from the diced wafers is discussed as well. The resonator and control box were fabricated at Auburn University in the microfabrication lab.

Chapter four discusses the experimental setup in detail. The acoustic testing for this thesis was performed in an acoustic chamber. Each experimental sweep is discussed and photographed along with the hardware and software required to produce the acoustic noise and record the response of the microphone inside the boxes.

Chapter five shows the results of the testing on the acoustic metamaterial resonator box and the control box. This chapter discusses the success of the acoustic metamaterial in achieving thesis objectives, the problems with design, testing issues that were encountered, and describes solutions to prevent future design problems. Testing was performed by varying the sound power level and distance from the sound source during each sine sweep.

Chapter six discusses the future work that can build on this thesis. Improved designs for the new acoustic metamaterial proposed in this thesis are discussed, and new areas for testing and research in the field of sound attenuation using acoustic metamaterials are proposed.

Chapter 2: Background

This chapter provides a brief history of the workings of traditional and current day MEMS gyroscopes. It then offers an explanation of the workings of the MEMS gyroscope and applications in which MEMS gyroscopes are currently being used. The chapter then illustrates a brief history of metamaterials and a detailed discussion of acoustic metamaterials and their applications. Lastly, this chapter provides a description of the workings of the Helmholtz resonator and various applications of Helmholtz resonators today.

2.1 Gyroscopes

Gyroscopes are sensors that measure an object's rotation. The word gyroscope was coined by Léon Foucalt who combined the Greek words "gyros" meaning rotation and "skopeein" meaning to see. The very first gyroscopes came about during the early 19th century and were composed of a rotating wheel attached to a frame called a gimbal [15]. The flywheel has a large angular momentum that counteracts externally applied torques, maintaining the orientation of the spin-axis. These devices were critical navigational instruments for sea travel and were capable of maintaining a fixed orientation despite the rotation of the earth or the ship. These early gyroscopes had a high degree of accuracy for their time [16].

As the years went by, gyroscopes were called upon to become smaller and more precise. The rotating gyroscopes began to encounter problems with bearing friction and wear [15]. Two new types of gyroscopes came on the scene to overcome these disadvantages, the optical gyroscope and the vibrating gyroscope. The optical gyroscopes make use of the Sagnac effect by

utilizing an optical ring and a dual laser system, which produce two beams of light traveling in opposite directions within the ring [17]. The optical gyroscopes eliminate the problems of vibration and friction, but have high associated manufacturing costs. The vibratory gyroscopes operate on the fundamental principle that a sinusoidal Coriolis force will be induced along the sense axis of the gyroscope, in response to an orthogonal angular rate input and the vibration of the proof-mass. Like the optical gyroscope, the vibrating gyroscope also presented an effective solution to the bearing problems because it eliminated rotating parts. The most notable of the vibratory gyroscopes are the MEMS gyroscope, the Tuning-Fork gyroscope, and the Hemispherical Resonator gyroscope [15].

2.1.1 MEMS Technology

Over the past few decades, MEMS gyroscopes have begun to replace the more traditional rotating gyroscopes due to their lower cost and smaller size. MEMS or microelectromechanical systems are devices that unite mechanical systems with electrical components within the scale of 1mm to 1μm [1]. MEMS devices are created using standard integrated circuit fabrication techniques such as photolithography and successive patterning of structural layers. These techniques can be used to build complex mechanical and electrical structures on a substrate, typically silicon. Extremely complicated systems that include the use of proof masses, actuators, dampers, springs, linkages, and many other mechanical devices can be fabricated using these techniques. One of the more complicated MEMS devices fabricated today is the MEMS gyroscope [15].

2.1.2 The Coriolis Effect

The Coriolis effect is a direct result of the motion of a body in a rotating frame of reference. The Coriolis effect gets its name from Gaspard Coriolis, a French physicist, and it appears in nature in weather phenomena such as tornadoes and hurricanes. The Coriolis effect is based on conservation of momentum and generates a force and acceleration, known as the Coriolis force and Coriolis acceleration, on a body in a rotating frame of reference. To understand the Coriolis effect, imagine a body traveling in a straight line on a rotating surface, such as planet Earth. In order for a body to move in a straight line on a rotating surface, such as the Earth, the Coriolis acceleration deflects the body in a counterclockwise manner if the object is in the northern hemisphere or a clockwise manner if the object is in the southern hemisphere [16].

The Coriolis acceleration is

$$\vec{a}_c = 2\vec{\Omega} \times \vec{v}_r \tag{2.1}$$

Where Ω is the angular rate and v_r is the radial velocity of the body. The vector cross product implies that the Coriolis acceleration and the corresponding force and displacement are perpendicular to the oscillation. This is essentially an energy transfer from a primary mode of vibration to a secondary mode that is measured. The excitation of the secondary resonance is the basis for the detection of the Coriolis effect. The Coriolis force is derived from Newton's second law and is

$$F_c = 2m\vec{\Omega}\times\vec{v}_r \tag{2.2}$$

2.1.3 Vibratory MEMS Gyroscopes

MEMS gyroscopes have become widely used over the last two decades because of their small size and cheaper manufacturing costs. The traditional rotational gyroscope can only be shrunk so far before friction and lack of suitable bearings of minute size inflate the manufacturing costs to unsuitable levels. The spinning mass of the rotational gyroscope was replaced by the oscillatory motions of the MEMS gyroscope proof mass. Although the vibratory gyroscope is not the only type of micromachined gyroscope, it is the most common due to the fact that a vibratory gyroscope requires no rotating parts or bearings. Utilizing MEMS fabrication techniques, significant savings can be achieved in the fabrication of gyroscopes in size, cost, and weight [15].

MEMS vibratory gyroscopes are typically composed of a proof mass suspended above the substrate attached to a flexible beam suspension system. The system can be represented as a two degrees-of-freedom spring-mass-damper system. The MEMS vibratory gyroscope operates on the fundamental principle that a sinusoidal Coriolis force will be induced along the sense axis of the gyroscope in response to an orthogonal angular rate input and the vibration of the proof-mass. The proof-mass is usually driven into resonance along the drive axis by an electrostatic actuator, however, electromagnetic and piezoelectric actuators can also be used. The sense axis is orthogonal to both the drive axis and the axis about which the angular rotation occurs [15]. A second electrostatic or electromagnetic actuator lies along the sense axis and measures the Coriolis force after the input of an angular rate. Because of these three orthogonal axes, the

drive, sense, and angular rotation axis, the typical MEMS gyroscope discussed in this thesis can only sense angular rotation about a single axis. That is why early Inertial Measurement Units or IMU's in automobiles consisted of three MEMS gyroscopes and three accelerometers placed at three orthogonal axes. This allows the IMU to sense angular rotation and acceleration in three dimensions. It is now possible to manufacture MEMS gyroscopes that can measure angular rotation about two or three axes [18].

A model for a basic gyroscope is shown below is Figure 2.1. The proof mass is driven into an oscillatory motion at its resonant frequency along the x-axis or drive axis. Any rotation about the z-axis or out of plane axis will cause a corresponding Coriolis force along the y-axis or sense axis. The amplitude of this force will be proportional to the rotational velocity. Motion along the sense axis is measured by the electrostatic actuator, and a corresponding force is applied to cancel out the motion along the sense axis. The magnitude of this force is a measure of the angular rate applied.

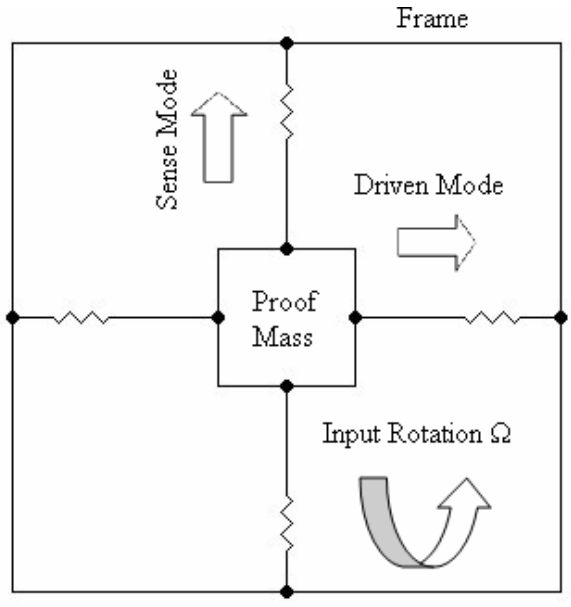

Figure 2.1: Lump model of a simple MEMS gyroscope

2.1.4 Drive and Sense Mode Operation

The Coriolis effect is based on conservation of momentum. The momentum source in a MEMS gyroscope is the drive-mode oscillator, and it consists of a proof mass being driven into resonance by an electrostatic actuator. The drive-mode oscillator can be modeled as a one degree-of-freedom spring-mass-damper system consisting of a suspension system providing stiffness, k_x, a proof mass, m, and the system damping, c_x, which consists of thermoelastic and viscous damping. The sense mode can be modeled in a similar way with suspension system k_y, proof mass, m, and damping c_y. The drive mode is the x-axis and is denoted with subscripts x while the sense mode is the y-axis and is denoted with subscripts y. The model for the MEMS gyroscope used to derive the equations of motion is shown below in Figure 2.2 [15].

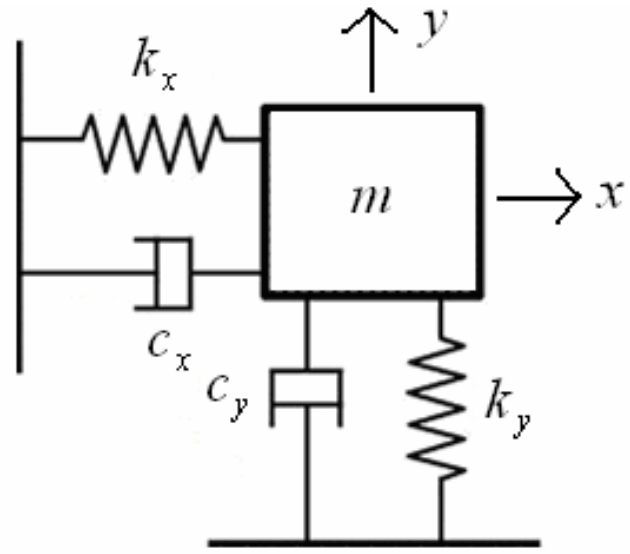

Figure 2.2: MEMS gyroscope model

The equations of motion along the drive axis and sense axis are

$$m\ddot{x} + c_x\dot{x} + k_x x = F_x \sin \omega_x t \tag{2.3}$$

$$m\ddot{y} + c_y\dot{y} + k_y y = -2mx_0\omega_x\Omega_z \cos(\omega_x t + \phi_x) \tag{2.4}$$

Where ω_x and ω_y are the undamped natural frequency along the drive axis and sense axis respectively, ξ_x and ξ_y are the damping ratios along the drive axis and sense axis respectively, and Ω_z is the rate of rotation about the z-axis or out of plane axis. The drive axis equation of motion comes from a simple spring-mass-damper system subjected to an oscillatory force of amplitude F_x [15]. The sense axis equation of motion is excited by the Coriolis force, which is shown below in equation 2.5.

$$F_c = -2m\Omega_z\dot{x} = -2m\Omega_z x_0\omega_x \cos(\omega_x t + \phi_x) \tag{2.5}$$

The amplitude and phase angle of the drive and sense mode steady state response is

$$x_0 = \frac{F_x}{k_x\sqrt{\left[1-\left(\frac{\omega}{\omega_x}\right)^2\right]^2 + \left[\frac{1}{Q_x}\frac{\omega}{\omega_x}\right]^2}} \tag{2.6}$$

$$\phi_x = -\tan^{-1}\left(\frac{\frac{1}{Q_x}\frac{\omega}{\omega_x}}{1-\left(\frac{\omega}{\omega_x}\right)^2}\right) \tag{2.7}$$

$$y_0 = \Omega \frac{\omega_x}{\omega_y{}^2} \frac{2x_0}{\sqrt{\left[1-\left(\frac{\omega_x}{\omega_y}\right)^2\right]^2 + \left[\frac{1}{Q_y}\frac{\omega_x}{\omega_y}\right]^2}} \tag{2.8}$$

$$\phi_y = -\tan^{-1}\left(\frac{\frac{1}{Q_y}\frac{\omega_x}{\omega_y}}{1-\left(\frac{\omega_x}{\omega_y}\right)^2} + \phi_x\right) \tag{2.9}$$

When the drive axis motion is at resonance, the phase of the drive mode is -90° and the amplitude of vibration reduces to

$$x_{0res} = Q_x \frac{F_x}{m\omega_x{}^2} \tag{2.10}$$

The sense mode achieves the highest gain when the resonant frequencies of the drive and sense axis are matched, but the detection bandwidth for this situation is 0 Hz [15]. When $\omega_x=\omega_y$ the phase angle of the sense mode becomes -90° and the amplitude of vibration reduces to

$$y_{0res} = \Omega_z \frac{2Q_y x_0}{\omega_y} \tag{2.11}$$

It is from equation 2.11 where the mathematical proof of improving gyroscope sensitivity is shown [15]. As formula 2.11 shows, the sensitivity of the MEMS gyroscope can be improved by increasing the drive mode vibration amplitude x_0 and increasing Q_y, which is usually

accomplished by decreasing damping through vacuum packaging. The natural frequencies of the drive and sense modes are

$$\omega_x = \sqrt{\frac{k_x}{m}} \tag{2.12}$$

$$\omega_y = \sqrt{\frac{k_y}{m}} \tag{2.13}$$

The Quality factors of the drive and sense modes are

$$Q_x = \frac{m\omega_x}{c_x} \tag{2.14}$$

$$Q_y = \frac{m\omega_y}{c_y} \tag{2.15}$$

The Coriolis force amplitude is directly proportional to the amplitude of the drive-mode oscillation [15]. Shown below in equations 2.16 and 2.17 is the simplified version of the equations of motion using a force balance. These two equations are a coupled system of second order differential equations coupled together by the Coriolis acceleration.

$$\ddot{x} + 2\xi_x\omega_x\dot{x} + \omega_x{}^2 x = \frac{1}{m}F_x - 2\Omega\dot{y} \tag{2.16}$$

$$\ddot{y} + 2\xi_y\omega_y\dot{y} + \omega_y{}^2 = 2\Omega\dot{x} \tag{2.17}$$

2.1.5 Design Rules and Sources of Error for MEMS Gyroscopes

In MEMS gyroscopes, the primary damping mechanism is thermoelastic [19]. This is because fluidic damping is minimized in MEMS gyroscopes due to vacuum packaging [20].

One of the problems in MEMS gyroscopes measuring techniques occurs due to the small amplitude of the Coriolis force in comparison to the driving force. For example, assume the gyroscope is driven by a sinusoidal drive vibration.

$$x(t) = x_0 \sin(\omega_d t) \tag{2.18}$$

Where ω_d is the drive frequency and x_0 is the oscillation amplitude. The Coriolis acceleration is

$$\vec{a}_c = 2\vec{\Omega} \times \vec{v}_r = 2\Omega x_0 \omega_d \cos(\omega_d t) \tag{2.19}$$

To illustrate the size of the Coriolis acceleration, plug in normal values such as x_0=1μm, Ω=1°/s, and ω_d=2π15 kHz. This gives a Coriolis acceleration of 3.3 mm/s^2. Assume that the sensing actuator is a second order spring-mass-damper system with a Quality Factor, Q, of 1. The displacement amplitude along the sense axis is less than one nanometer. However, typical quality factors are many orders of magnitude larger than 1.

Another fundamental problem with MEMS gyroscopes is quadrature error. Quadrature error is derived from manufacturing tolerances and manifests itself in the form of a misalignment of the drive axis. Instead of operating perfectly orthogonal to the sense axis, a small component

of the drive axis can induce motion along the sense axis. Even though this misalignment is typically very small, the minute Coriolis acceleration can often be smaller than the quadrature error [18].

One of the ways to make this displacement larger and thus increase the sensitivity of the sensor is to design the gyroscope with a high Q and to tune the drive frequency and the resonant frequency of the sense axis to match. However, it is difficult to design structures to exact resonant frequency due to manufacturing tolerances. This can be circumvented by designing the sense mode at a higher natural frequency than the drive mode. Then the sense mode natural frequency can be decreased by using the electrostatic forces in the sense actuator to tune the mechanical spring constant. Typically, if these resonant values are within 5% or 10% of each other, it is considered acceptable [18].

Unfortunately, the high Q design of the MEMS gyroscope makes it particularly sensitive to vibrations at or near the resonant frequency of the proof mass [21, 22]. These vibrations have the potential to couple into the proof mass motion along either the drive axis, sense axis, or axis of rotation of the gyroscope. However, vibration coupling into the proof mass motion along the drive axis is not as large of a problem as vibration coupling along the sense axis. This is due to the fact that MEMS gyroscopes are designed with a control loop that continuously corrects the vibration of the proof mass along the drive axis. This is done to ensure constant amplitude of motion of the proof mass along the drive axis. There is no control loop used on the sense axis. MEMS gyroscopes are very stiff along the axis of rotation, or z-axis, so vibrations coupling into proof mass motion along the axis of rotation should cause little to no effect. To minimize these negative effects from outside sources of vibration, the sensor is designed with a detection bandwidth that is significantly below the resonant frequency [23].

The same reasons that make MEMS gyroscope sensitive to the effects of vibration also apply for acoustic noise. There are two ways that acoustic signals can be transferred to the micro-structure of the MEMS gyroscope causing undesirable effects. The acoustic noise can induce mechanical vibrations to the frame of the gyroscope that propagate through the sensors package and into its micro-structure. Additionally, the acoustic signal can enter the device directly by traveling through the fluid medium, typically air or water, and interacting with the sensor's packaging. The packaging is in direct contact with the fluid, and the acoustic wave propagates differently through different fluid mediums [5].

2.1.6 Applications of MEMS Gyroscopes

MEMS gyroscopes continue to replace traditional gyroscopes due to their lower power consumption, lower cost, and smaller size. For this reason, MEMS gyroscopes are being seen in many new applications such as image stabilization in cameras and camcorders, aircraft, automotive rollover detection, and GPS backups. They are also used in underwater applications such as digital compasses and autonomous underwater vehicles. MEMS gyroscopes have been used for some time in commercial applications such as Inertial Measurement Units or IMU's, video games, and cell phones. Although some of the environments in which MEMS gyroscopes are used can be benign, some can be harsh environments that experience high frequency, high power acoustic noise or vibrations, high temperatures, and mechanical shock. These environments have the potential to have an adverse effect the operation of MEMS gyroscopes.

2.2 Metamaterials

In the last decade, interest and research in the area of metamaterials has shown substantial growth. A metamaterial is an artificially fabricated device or structure that is built to produce desired material responses that can either mimic known behaviors or produce responses that do not occur naturally in other known materials. These responses are engineered through fabricating some man-made structure in the host material or medium, which acts like an inclusion or discontinuity within the material. It is known that in particulate composite structures, electromagnetic waves react with the inclusions. This reaction produces magnetic and electric moments, which change the permeability and permittivity of the bulk composite in electromagnetic materials. These properties are analogous to the acoustic properties of dynamic density and compressibility as shown in the next sections [24]. By altering the properties of the material, metamaterials can change how the material reacts to waves, electromagnetic or acoustic, by inserting or replacing molecules in the natural structure with artificial structures significantly smaller than the wavelength of the present waves [25].

The reason these metamaterials have come to the forefront of scientific research is the goal to be able to engineer the optical, electrical, and acoustic properties of materials. These metamaterials have great potential for future improvements in technology including reduction in size, weight, cost of components, and the ability to improve performance of systems. Although there are several classifiable categories of metamaterials, this paper will discuss electromagnetic metamaterials, optical metamaterials, and acoustic metamaterials. This thesis proposes the use of a new type of inertial acoustic metamaterial composed of an array of Helmholtz resonators with

the purpose of attenuating high frequency noise for application as a noise filter in conjunction with a MEMS gyroscope.

2.2.1 Electromagnetic Metamaterials

Veselago first proposed the existence metamaterials in 1968. He hypothesized the existence of materials with both negative effective permittivity (ε) and permeability (μ), which create a negative refractive index. He named them left-handed materials. However, these materials did not exist in nature then, nor do they now. It is only in recent years that these metamaterials, as they are now known, have been artificially fabricated. Veselago concluded that these left-handed materials would have much different wave propagation characteristics than materials with positive values for permittivity and permeability. He hypothesized that such properties as Cherenkov radiation, Snell's law (meaning negative refraction), and Doppler shift would be reversed in these special materials and even the value of radiation pressure could be reversed to radiation tension. These were hypotheses because the material did not exist and could not be experimentally verified, until recently [26].

Electromagnetic metamaterials are effectively homogenous electromagnetic structures fabricated artificially and possess unusual qualities not present in nature. An effectively homogenous structure requires that the average cell size be significantly smaller than the guided wavelength. This characteristic of electromagnetic materials ensures that when a wave propagates inside the metamaterial network refractive phenomena will dominate over the scattering or diffraction phenomena. It means that the metamaterial network can be assigned certain constitutive parameters such as permittivity, ε, and permeability, μ. These values can only

be assigned because the electromagnetic wave that comes in contact with the metamaterial network only reacts with the average constitutive parameters, which can be fabricated as desired by altering the metamaterial unit cell. The wave is forced to observe these average constitutive parameters because the unit cell is significantly smaller than the wavelength of the wave [27].

The permittivity and permeability are related to the refractive index, n by

$$n = \pm\sqrt{\varepsilon\mu} \tag{2.20}$$

This allows for four possible sign combinations of permittivity and permeability: (+,+), (-,+), (+,-), and (-,-). These combinations are illustrated in Figure 2.3 below. The first three combinations are conventional materials found in nature, but the last combination where permittivity and permeability are both negative has not yet been discovered in nature and must be artificially manufactured. When a material has negative permittivity and permeability it is referred to as a left-handed material or a double-negative material. When both permittivity and permeability are negative it appears that the refractive index would be negative, however, it has been shown through causality that the negative square root should be chosen [28]. Although metamaterials are most often left-handed they are not required to be so, many are fabricated that way for the desirable properties that can be gained by using left-handed materials [27].

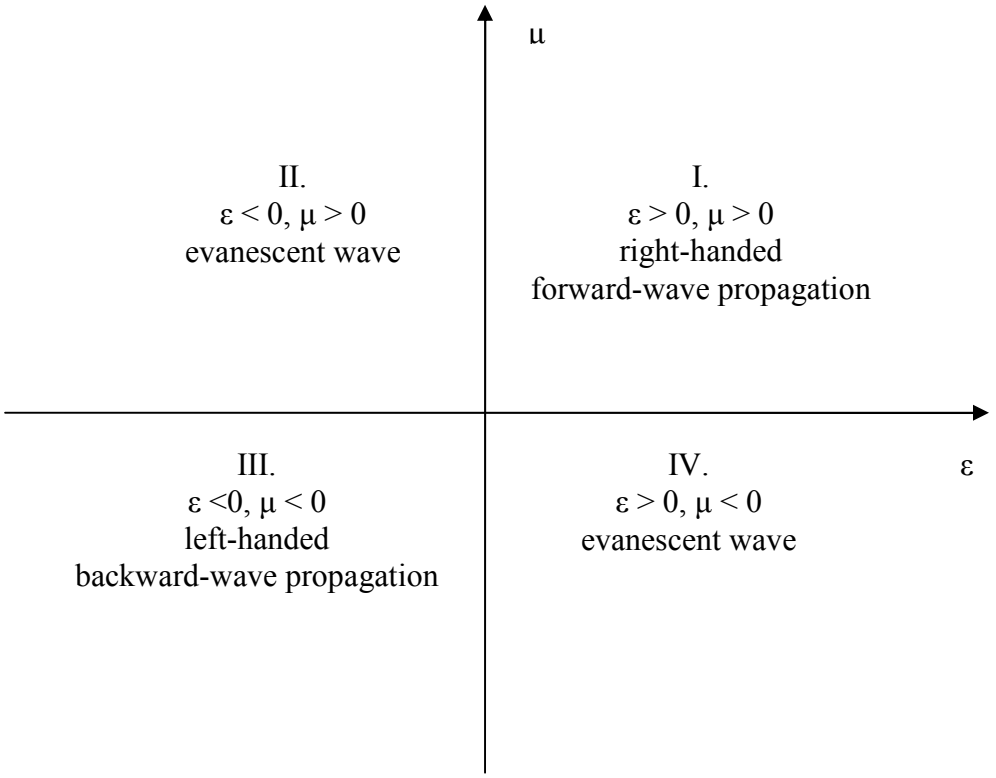

Figure 2.3: Refractive index diagram

The term metamaterial is a much broader term than left-handed materials and does not require negative permittivity and/or negative permeability. A metamaterial may or may not possess these characteristics, but a left-handed material must have negative values of both permittivity and permeability. Left-handed materials also have the disadvantage of large loss and narrow bandwidth restricting their use. This has caused researchers to search for additional uses of metamaterials beyond simply left-handed materials.

Other uses for electromagnetic metamaterials have come in the form of manipulation of electromagnetic waves. Smith *et al* realized a gradient refraction index medium in 2005 that successfully bent electromagnetic waves. The next year, Pendry *et al* proposed the optical

transformation used in the much publicized invisibility cloak that controls electromagnetic wave propagation using metamaterials [29].

2.2.2 Optical Metamaterials

One of the subsets of electromagnetic metamaterials that specifically deals with controlling light propagation is called optical metamaterials. Optical metamaterials have the ability to control the path of light through the manipulation of their high refractive index, which can have a positive or negative sign. This gives these optical metamaterials the ability to slow the speed of light propagation, bend light in any direction, or even reverse the direction of light propagation.

Like all metamaterials, optical metamaterials derive their impressive qualities through the design and fabrication of artificial inclusions within a host material. Where these inclusions are placed in the host material, their geometries, and material compositions all have an effect on the optical properties of the material as a whole. Many materials have been discovered in nature with interesting optical qualities. These optical materials react with the electric field of a passing electromagnetic wave, due to the fact that the material's atoms have a weak reaction with the magnetic field of the wave. Oppositely, optical metamaterials are fabricated in such a way to cause both the magnetic and electric fields to interact with the inclusions that make up the metamaterial. This causes optical metamaterials to possess qualities that have not yet been found in nature [30].

Controlling light propagation through the use of optical metamaterials is important for many different applications. Some of the most notable applications are the invisible cloak [31],

the perfect lens [32], subwavelength imaging [33], and optical data storage [34]. So far, the high losses and limited operational bandwidth in optical metamaterials in comparison to the previously mentioned natural optical materials have limited their use in areas such as imaging and sensing [30].

2.2.3 Comparison Between Electromagnetic and Acoustic Metamaterials

Acoustic metamaterials are a natural transition from electromagnetic metamaterials due to the analogy between light and sound waves. This analogy can be shown by comparing the two waves, electromagnetic and acoustic. The acoustic wave is a longitudinal wave, whereas in electromagnetism, both magnetic fields and electric fields are characterized as transverse waves. However, both of these waves, acoustic and magnetic, do share wavevector, wave impedance, and power flow characteristics. These shared characteristics allow the acoustic and electromagnetic waves to be compared to each other by a simple analogy. This analogy allows for equivalent values between the electromagnetic permeability and permittivity and the acoustic dynamic density and compressibility, where compressibility is the inverse of the dynamic modulus. Through the manipulation of these values in the acoustic metamaterials, various unique structures can be built that have amazing properties [25]. Table 2.1 shows the analogy between acoustic and electromagnetic properties.

Acoustic:	Electromagnetic:
Dynamic Density, ρ_d	Permeability, μ
Dynamic Compressibility, β	Permittivity, ε
Acoustic Pressure, P	Electric Field, E
Particle Velocity, u	Magnetic Field, H

Table 2.1: Analogous acoustic and electromagnetic properties

2.2.4 Acoustic Metamaterials

An acoustic metamaterial derives its unique properties through the artificial fabrication of resonators into each unit cell of material. These resonators can be fabricated at any desirable size, which allows the construction of resonators that are on order much smaller than the wavelength of the present acoustic noise. The resonators can also be designed to have a resonant frequency where desired. This allows the material properties such as modulus and mass density to be ascribed to the material and through the design of the resonators these material properties can be designed to be negative [25]. Such a design allows for acoustic metamaterials to complete the same task that has been accomplished in electromagnetic metamaterials, making a negative refraction index. This has been achieved using double negative acoustic metamaterials [28].

Previously, the analogy between light and sound waves was discussed. This analogy allows for equivalent values between the electromagnetic permeability, μ, and permittivity, ε, and the acoustic dynamic density, ρ_d, and compressibility, β, where compressibility is the inverse of the dynamic modulus. The static elastic modulus and the static density are required to have positive values to maintain a stable structure, but their acoustic dynamic effective properties can become negative at resonance [25].

The bulk modulus, B, is defined as

$$B = -V\frac{\partial p}{\partial V} \tag{2.21}$$

Where the bulk modulus is the inverse of the compressibility, β, and V is the volume, and p is the gauge pressure. It is possible for bulk modulus to have a negative value if the unit cell expands in volume while the gauge pressure is positive [35]. Helmholtz resonators have been shown to have a negative group velocity in response to a negative bulk modulus [10]. Additionally, rubber spheres in water have shown negative bulk modulus over a small bandwidth [28].

Newton's second law defines effective mass density, ρ_{eff}, as

$$\rho_{eff} = \frac{1}{a}\frac{F}{V} \tag{2.22}$$

Where F is the total force, V is the volume, and a is the acceleration. If mass density is negative, it requires that the average acceleration of the unit cell be in the opposite direction of the driving force [35]. Negative mass density has been effectively proven numerically and experimentally [36].

The acoustic refractive index, n_a, is

$$n_a = \sqrt{\frac{B_0\rho_{eff}}{\rho_0 B}} \tag{2.23}$$

Where B_0 and ρ_0 are the reference bulk modulus and reference density respectively. For the acoustic refractive index to be negative, it requires that the mass density and the bulk modulus both be negative. With positive references, if the mass density and bulk modulus are both negative then the term under the radical will be positive [35]. However, as in electromagnetic metamaterials, it has been shown that the negative square root should be selected due to causality [28]. The acoustic negative refractive index has been demonstrated theoretically [28], but as yet it has not been proven experimentally.

Since these acoustic metamaterials are relatively new, most were created within the last decade, they have only recently begun to emerge as potential devices that can manipulate sound waves. An earlier device, the phononic crystal, is the precursor to the acoustic metamaterial and has been successful at manipulating sound waves. Acoustic metamaterials can currently be divided into two classes: intrinsic acoustic metamaterials and inertial acoustic metamaterials [37].

2.2.5 Phononic Crystals

Phononic crystals are the precursor to acoustic metamaterials. As with metamaterials, the phononic crystals gained widespread attention due to the large amount of research being performed on how elastic waves propagate through inhomogeneous media. The phononic crystal is a type of inhomogeneous media whose elastic coefficients vary in a periodic fashion. Using phononic crystals, it is possible to create frequency regions that are not capable of propagating elastic waves, making them in theory a perfect mirror. This frequency region is known as a

phononic gap. This property of phononic crystals makes these devices well suited to applications such as waveguides or acoustic filters [38].

Phononic crystals were first proposed in the 1990s with the intent of creating a large frequency band gap. The success of these materials in creating this band is due to phenomena known as Bragg scattering [37]. Bragg scattering occurs when subatomic particle waves or electromagnetic radiation, with wavelengths on the same order as the atomic spacing of the crystalline media through which the waves are traveling, interact with interstitial voids or defects that cause a scattering of the wave in accordance with Braggs law. Within a certain frequency band gap, the transmitted waves are suppressed in intensity by the phononic crystals due to diffraction caused by Bragg scattering. The size and effect of these band gaps is dependant on the mass density and the elastic constants of the crystal material [39].

The dependence of the phononic crystals on Bragg scattering is their main weakness as a material. Bragg scattering requires the atomic spacing of the material to be on the same order as the wavelength of the transmitted wave. Acoustic waves have long wavelength at low frequency making these devices impractical for some purposes [37]. These limitations in the phononic crystal can be improved upon using acoustic metamaterials. Due to the ability to manufacture acoustic metamaterials on an order significantly smaller than the acoustic wavelength, the acoustic metamaterial can be described using such effective material properties as mass density and bulk modulus [25].

2.2.6 Intrinsic Acoustic Metamaterials

In an intrinsic acoustic metamaterial, the inclusions are created from a material with a significantly lower phase velocity than the surrounding matrix. The most common example of this type of acoustic metamaterial is a soft, silicon rubber sphere [28]. This soft rubber sphere has phase velocities that are nearly two orders of magnitude smaller than ordinary solids. The low phase velocity materials are necessary because of the wavelength of the matrix at resonance. Typically, the lattice constant is on the order of the inclusion size. In an inclusion, the eigenmodes of the lowest order occur when the wavelength inside the inclusion is two times greater than the size of the inclusion. When the inclusion reaches resonance, the unit cell is much smaller than the matrix wavelength.

2.2.7 Inertial Acoustic Metamaterials

The inertial form of acoustic metamaterials does not require materials of slow phase speed like the intrinsic metamaterials. Instead inertial acoustic metamaterials create local resonances by fabricating inclusions in the material that function as spring-mass-damper systems. These inertial oscillators can attenuate sound and affect waveforms based on their design characteristics. The two most common inertial acoustic metamaterials are the Helmholtz resonator and coated spheres. The Helmholtz resonator is discussed in detail in subsequent sections. The coated spheres are dense spheres that are coated in a silicon rubber and encased in an epoxy. The resulting structure that is created is a spring-mass-damper system. The epoxy casing acts as a spring, and the sphere oscillates inside the casing at resonance [37].

2.2.8 Applications of Acoustic Metamaterials

Acoustic metamaterials are a new and emerging field, but already they show promise in military and civilian applications such as acoustic cloaking, medical imaging, and noise reduction. One of the most promising areas is the acoustic cloak. Similar to the invisibility cloak using electromagnetic metamaterials, an acoustic cloak has been proposed [40]. This acoustic cloak has the potential to manipulate sound waves in such a way as to allow sound waves to propagate around an object as if it were not there. The acoustic cloak has successfully been tested using a network of acoustic circuit elements, which effectively bent ultrasound waves around an object and remained effective over a 12 kHz band [41]. The cloak also has potential military applications such as hiding a submarine from conventional sonar. The acoustic cloak and other acoustic metamaterials have potential applications in ultrasound imaging in medicine where certain areas of the body can cause scan interference. Acoustic metamaterials have the potential to clear up ultrasound interference by hiding the problem areas and allowing the desired areas to be visualized with ultrasound.

A network of Helmholtz resonators can be used to create an acoustic superlens to focus sound waves underwater [42]. An acoustic hyperlens has also been experimentally proposed [43]. Such a lens composed of acoustic metamaterials has the ability to overcome the diffraction limit that hinders other types of lens. This has the potential to improve the resolution in areas such as non-destructive testing, medical ultrasound imaging, and underwater sonar systems.

Additionally, acoustic metamaterials have been used to attenuate sound in situations where a high level of noise at certain frequencies is undesirable. The ability to fabricate the

inclusions in acoustic metamaterials to resonate at certain frequencies allows acoustic metamaterials to be designed to attenuate sound at desired frequencies. Acoustic metamaterials have been successfully used to attenuate sound in a low frequency band from 50-1000 Hz [11]. In this experiment, the acoustic metamaterial was successfully attenuated sound at an average of 40 dB over the 50-1000 Hz frequency range. This thesis proposes to test a MEMS fabricated acoustic metamaterial whose purpose is to attenuate sound at the resonant frequency of a MEMS gyroscope, which can be anywhere between 10-20 kHz depending on manufacturing tolerances. For the purposes of this experiment, the acoustic metamaterial has been designed to attenuate sound at 14.5 kHz.

2.3 Helmholtz Resonators

The Helmholtz resonator was named after Herman von Helmholtz, who designed the first resonator bearing his name in the 19th century. Since then, the Helmholtz resonator has been studied extensively and has been used in industrial applications for many years. A Helmholtz resonator can take many forms, but in its simplest design it consists of a large cavity that contains a fluid sealed to its environment except for a small neck. The resonator acts like a spring-mass-damper system where the stiffness is the result of the compression of the fluid in the cavity. The mass is a combination of the fluid in the neck, which moves as a unit, and the sound radiating from the neck, which has both radiation mass and radiation resistance. The resistance or damping of the system is a combination of the sound radiating from the neck as well as the viscous losses that occur at the neck walls [44].

When in the presence of acoustic noise, the fluid in and around the neck begins to oscillate. As the fluid in the neck oscillates, the fluid inside the cavity vibrates at a resonant frequency that is determined by the type of fluid present in the resonator and the dimensions of the resonator. The oscillating air in the neck of the resonator induces viscous dissipation at the surface of the neck causing the acoustic noise to lose energy at the resonant frequency of the Helmholtz resonator. For Helmholtz resonator designs, it should be noted that to minimize the creation of standing waves within the resonator, the length dimension of the resonator should be less than 1/16 of the wavelength [12].

2.3.1 Helmholtz Resonance

The Helmholtz resonator shown below in Figure 2.4 consists of a rigid walled cavity with a volume of V as well as a neck length L and area S. A Helmholtz resonator can have necks and cavities of various shapes and sizes; however, a cylindrical neck and cavity were used in these experiments and derivations.

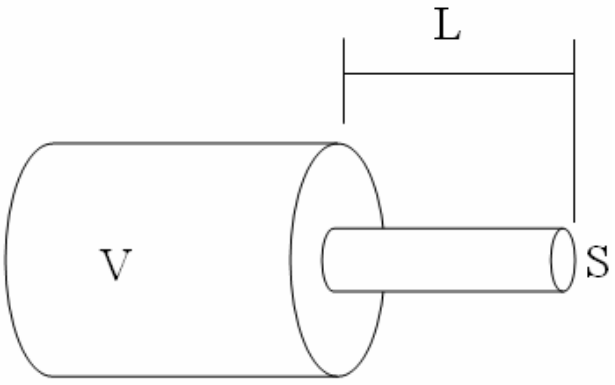

Figure 2.4: Diagram of a Helmholtz resonator

As previously stated, the Helmholtz resonator is analogous to a spring-mass-damper system. This simplification is known as an acoustic lumped element. Acoustic lumped elements is a simplification of the behavior of sound occurring when sound interacts with structures that are significantly smaller than the acoustic wavelength of the sound. Researchers in the mechanical and electrical sciences have long been using electrical models analogously with mechanical models, and as such the mechanical spring-mass-damper system is analogous to the electrical RLC circuit as shown in Figure 2.5.

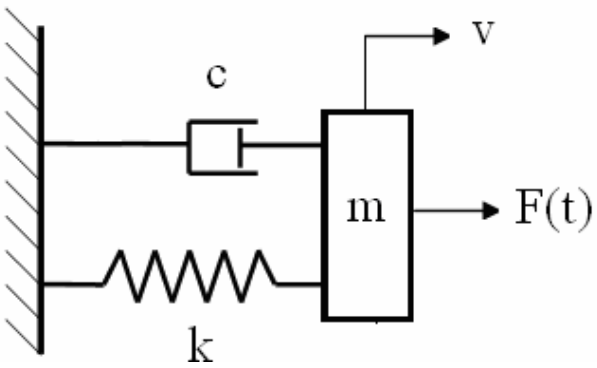

Figure 2.5: Mechanical representation of a Helmholtz resonator

The overall goal is to design the resonator to attenuate sound at a certain frequency. This frequency is the resonant frequency of the Helmholtz resonator. The resonant frequency of a spring-mass-damper system, ω_0, is

$$\omega_0 = \sqrt{\frac{k}{m}} \tag{2.24}$$

Where k is the stiffness of the system and m is the mass of the system. To determine the total mass of the Helmholtz resonator, one must consider both the mass of the fluid in the neck moving as a unit as well as the sound radiating from the neck, which has both radiation mass and radiation resistance. The combination of these two masses is the total effective mass denoted as m and is equivalent to the product of the density, ρ, of the fluid and the volume of the neck.

$$m = \rho_0 SL' \tag{2.25}$$

The effective length, L', used in this experiment is the well known end correction proposed by Rayleigh, which uses a model of a piston radiating into half-space [45]. Panton and Miller [12] found that the Rayleigh end correction and resonance equation gave satisfactory results with their testing of Helmholtz resonators. The L' length correction proposed by Rayleigh is

$$L' = L + \Delta_o + \Delta_i \tag{2.26}$$

Where Δ_0 is the outside end length correction and Δ_i is the inside end length correction. Rayleigh proposed the end correction should be

$$\Delta_0 = \Delta_i = \frac{8r_0}{3\pi} \tag{2.27}$$

In equation 2.27, r_0 is the radius of the neck. The stiffness of the system can be determined by modeling the neck as fitted with a sealed piston, which represents the total mass of the fluid in the neck. If this piston is pushed down compressing the fluid inside a distance x, this produces a decrease in volume inside the neck and an increase in the pressure. The change in volume, ΔV, is

$$\Delta V = -Sx \tag{2.27}$$

This change in volume also results in a proportional change in density, which is known as a condensation, s.

$$s = \frac{\Delta\rho}{\rho} = \frac{-\Delta V}{V} = \frac{Sx}{V} \tag{2.28}$$

The force, f, needed to create and maintain the displacement of the piston is equivalent to the product of the acoustic pressure increase, p, and the area of the piston, or neck.

$$f = kx = pS \tag{2.29}$$

The acoustic pressure can be written as

$$p = \rho c^2 s = \rho c^2 \frac{\Delta\rho}{\rho} = \rho c^2 \frac{Sx}{V} \tag{2.30}$$

The speed of sound in air is denoted by the variable c. The stiffness of the system, k, can be found by rearranging equation 2.29 and substituting the acoustic pressure found in equation 2.30 and simplifying.

$$k = \frac{pS}{x} = \frac{\rho c^2 S^2}{V} \tag{2.31}$$

Plugging this value for stiffness of the Helmholtz resonator and the total mass of the resonator into equation 2.24 and simplifying, determines the resonant frequency of the Helmholtz resonator in rad/s.

$$w_0 = c\sqrt{\frac{S}{VL'}} \tag{2.32}$$

The equation can be further simplified to give the resonant frequency in Hz [44].

$$f = \frac{c}{2\pi}\sqrt{\frac{S}{VL'}} \tag{2.33}$$

This equation is the same well-known equation developed by Rayleigh [45].

2.3.2 Applications of Helmholtz Resonators

The Helmholtz resonator is a device that can have positive effects while costing very little to manufacture due to its simple design. They have been studied extensively since Hermann von Helmholtz's initial study on musical tones. The Helmholtz resonator has already found commercial uses in the construction, automobile, and aerospace industries. These uses include: damping vibrations associated with building acoustics, damping noise associated with aircraft, and tuning the internal combustion engine to reduce noise in the exhaust or improve efficiencies in the intake.

Research on Helmholtz resonators has been performed extensively for a multitude of intended purposes. A periodic array of Helmholtz resonators has been used to destroy shock waves in a closed tube [46]. Helmholtz resonators have also been used as a noise control device to dampen the noise of compression waves emanating from the exit of high-speed train tunnels [47]. Micro-Perforated Panels (MPP) have been used to reduce noise in several applications due to their robustness, ease of manufacture, and the extreme environments in which they can be operated [48]. Additionally, Helmholtz resonators have been used at the MEMS scale for tunable acoustic absorption where the resonant frequency of the resonator can be adjusted to account for various frequencies [49]. MEMS scale Helmholtz resonators have also been used in the area of micro propulsion where the resonators are fabricated on the walls inside the nozzle to improve thrust performance [50] and many other uses.

Chapter 3: Fabrication

This chapter describes how the devices were fabricated using MEMS fabrication techniques and how the resonator and control boxes were assembled for use in the testing stage.

3.1 Resonator Box Design

Each Helmholtz resonator was designed to resonate at 14.5 kHz. The dimensions of the resonator were selected using equation 2.33. Equation 2.33 shows that the values that determine the resonant frequency of the Helmholtz resonator are the volume of the cavity, the effective length of the neck, and the cross sectional area of the neck. The resonators were fabricated on a 1000 μm thick silicon wafer. The length of the neck was set at 500 μm and the length of the cavity was set at 500 μm. The neck and cavity each have a cylindrical cross section and share a common centerline. The diameter of the neck was designed to be 50 μm and the diameter of the cavity was designed to be 362 μm, as shown in Figure 3.1. Figure 3.2 shows the dimensions for the entire one inch square array of resonators, the actual number of etched resonators is more than 30 times the number depicted.

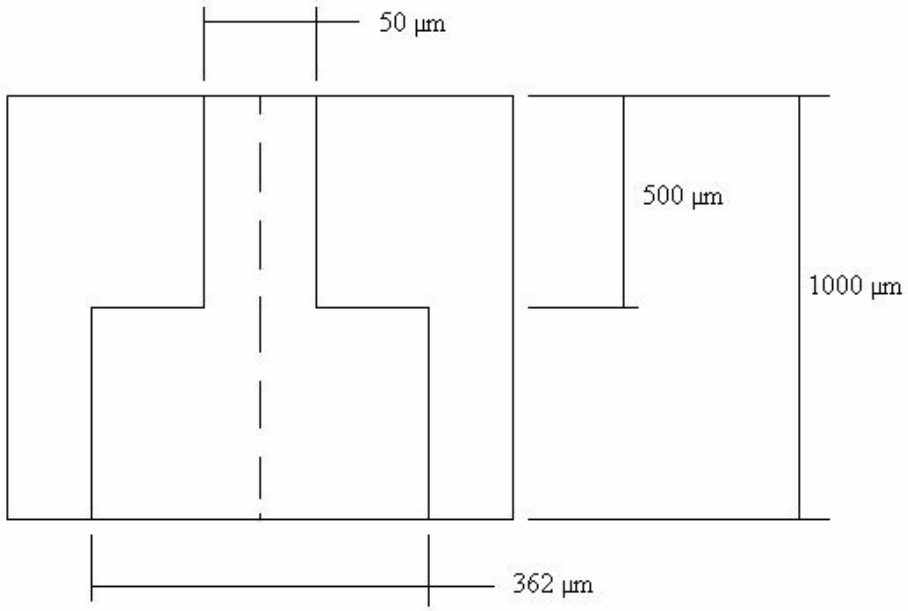

Figure 3.1: Cross section of individual resonator

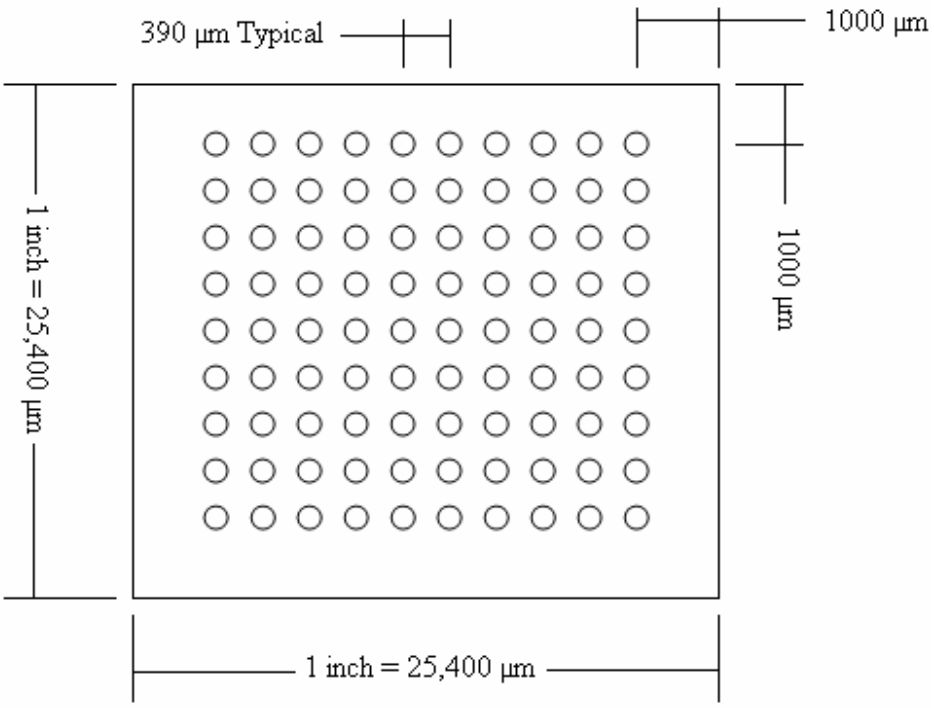

Figure 3.2: Dimensions for array of resonators

3.2 Resonator Box Fabrication

The resonator box was fabricated using standard MEMS fabrication techniques with a silicon wafer as the substrate. The resonators are etched into the silicon substrate at the desired dimensions. The resonators were fabricated at Auburn University in the microfabrication lab. The acoustic metamaterial is referred to as the resonator box after the devices have been fabricated and assembled into a box. The control box is a box of the same materials, dimensions, and characteristics with no resonators.

3.2.1 Photoresist, Pattern, and Exposure

The resonator box fabrication begins with a four inch diameter 1000 μm thick silicon wafer. The wafer surface is cleaned and the positive photoresist type AZ4620 was spun in a thick layer onto the wafer surface. The photoresist was then baked on a hot plate to ensure dehydration. The pattern, shown in Figure 3.3, was used as a mask to etch the resonator neck of the resonator. A similar pattern was used on the back side of the wafer to etch the resonator cavity. The pattern is placed in the photoresist layer on the silicon wafer. The wafer and mask are then placed in the Karl Suss MA6/BA6 mask aligner, see Figure 3.4, which aligns the mask to the wafer and then exposes the photoresist using high intensity ultraviolet light. The mask blocks the exposure of photoresist where etching is not desired. The photoresist on the wafer is then developed for one minute in a chemical solution that is three parts deionized water and one part developer AZ 400K. This washes away the exposed photoresist leaving only the unexposed

photoresist in the desired pattern and bare silicon where etching is desired. The wafer and photoresist are then baked one more time to harden the remaining photoresist and to improve the adhesion of the photoresist to the wafer surface. The wafer then travels to the Surface Technology Systems M/PLEX ICP, or advanced silicon etcher, to etch the resonator necks.

Figure 3.3: Pattern used to etch resonator necks

Figure 3.4: Picture of exposure device

3.2.2 Advanced Silicon Etcher

The cavity and neck of the resonators each consist of a cylindrical hole etched halfway through the wafer, 500 μm deep. The cavity and neck were etched using the Advanced Silicon Etcher. This device utilizes the process known as DRIE, Deep Reactive Ion Etching. The DRIE process revolutionized the fabrication of MEMS devices. It allows deep trenches to be etched with high aspect ratios and vertical sidewalls.

The DRIE process is an expansion of the Bosch process, which was first developed in the 1980s. The Bosch process etches channels in a two step process that takes place in an ICP, or inductively-coupled plasma chamber. The first step begins the trench with a plasma etch, and the second step coats the sidewalls with a passivation layer to protect the sidewalls from the next etch. This way the trench can be etched down while maintaining straight sidewalls.

DRIE expands on the Bosch two step process and consists of three distinct phases. The first phase is the passivation cycle, which uses C_4F_8 plasma to deposit a protective polymer on all surfaces. The second phase uses directionally accelerated ions to eliminate the passivation layer from the bottom of the trench while leaving the passivation layer on the sidewalls. The third phase uses SF_6 plasma to etch the exposed silicon in the bottom of the trench. The second and third phases make up the etch cycle. The two cycles, passivation and etch, are repeated until the correct depth of the trench is reached [15]. Figure 3.5 shows the Advanced Silicon Etcher used to etch the resonators in the microfabrication lab at Auburn University, and Figure 3.6 shows the etched necks on one side of the wafer.

Figure 3.5: Advanced silicon etcher at Auburn University

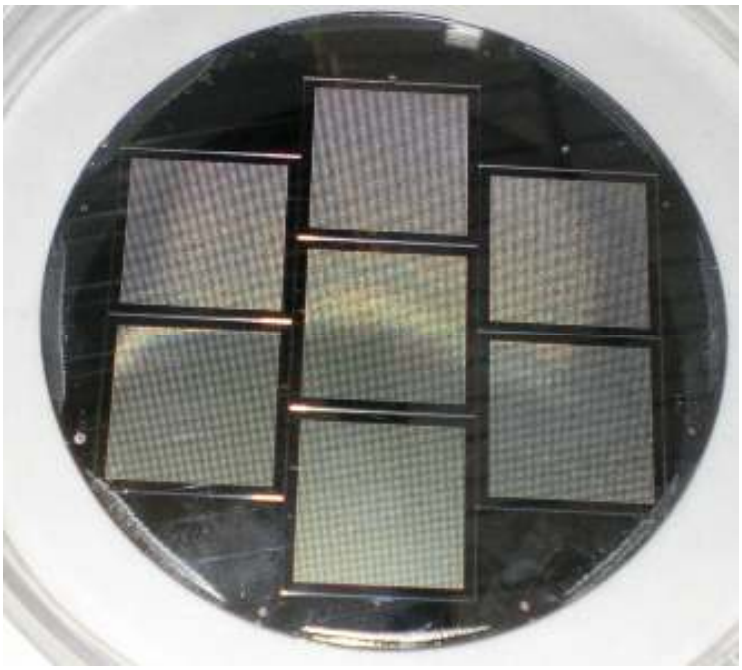

Figure 3.6: Necks that have been etched in the advanced silicon etcher

3.2.3 Backing Wafer

Now that the resonator necks have been etched halfway through the wafer, the same process must be repeated on the backside of the wafer. However, there are now hundreds of etched necks on the other side of the wafer. To apply the photoresist for the etching of the cavities, the neck side of the wafer has to be attached to the photoresist spinner without damaging the necks. This is accomplished by attaching a backing wafer to the neck side of the resonator wafer with a layer AZ5214 photoresist. The photoresist holds the two wafers together and allows photoresist to be spun on to the other side of the resonator wafer by attaching the backing wafer to the photoresist spinner. The photoresist that holds the backing wafer to the resonator wafer can then be etched away, and the backing wafer can be removed without damaging the necks. A standard four inch diameter silicon wafer was used as the backing wafer.

3.2.4 Dicing

The resonator squares on the wafer were in a pattern that is complicated to dice. So during the DRIE, the area that separates the squares was etched through the entire wafer so the one inch squares could be assembled into a box. The control box did not require any etching, so it was diced from a standard four inch diameter 1000 μm thick wafer. The control box squares were diced using a dicing machine type DAD3220, shown in Figure 3.7, into five identical one inch squares. In addition to the control box, the Pyrex used for anodic bonding discussed in the next section had to be diced into one inch squares from Pyrex wafers.

Figure 3.7: Dicing saw used to dice the completed squares from the wafer

3.2.5 Anodic Bonding and Box Assembly

At this point in the process the neck and cavity have each been etched through the wafer and the one inch squares have been diced or etched into individual squares. The neck is 500 μm deep and the cavity is 500 μm deep allowing for manufacturing tolerances. For the resonator to behave as desired, the cavity must be sealed. This is accomplished through a process called anodic bonding.

Anodic bonding allows for silicon and borosilicate glass to be bonded together. It is the most common bonding method utilized in microfabrication. To seal the cavities on the back side of the wafer, a pane of glass is anodically bonded to the back of the wafer. The bond is created through the simultaneous use of electrostatic attraction and temperature. To accomplish the bond, a voltage source is used to apply a large voltage between an anode weight on top of the silicon wafer and a cathode weight under the glass pane. The silicon and glass are bonded together by the applied electric field [15].

Advantages of anodic bonding include the low bonding temperatures, usually in the range of 200°C to 500°C. Also, the anodic bond provides a good hermetic seal. It should be noted that it is necessary to select a glass that has a coefficient of thermal expansion similar to silicon. For this process, Pyrex wafers are usually chosen [15]. For the resonator box fabrication, a diced Pyrex wafer was used to seal the cavities and the voltage source used was a HP 6448B DC Power Supply. Figure 3.8 below shows the magnified wide view of the array of etched resonators, while Figure 3.9 shows a closer view of the etched resonators from the cavity side. The resonator necks can be seen through the cavities.

Each square that made up the resonator box had a one-dimensional array of Helmholtz resonators consisting of 3600 microresonators etched into the silicon. These five one inch squares were assembled into a box using Krazy Glue to bond the edges together. The box was used to completely enclose a microphone in the experimental test setup. The microphone simulated a MEMS gyroscope, and the acoustic response of the microphone was recorded to see if the resonators successfully attenuated sound at the desired frequency of 14.5 kHz. The completed assembled resonator box is shown in Figure 3.10.

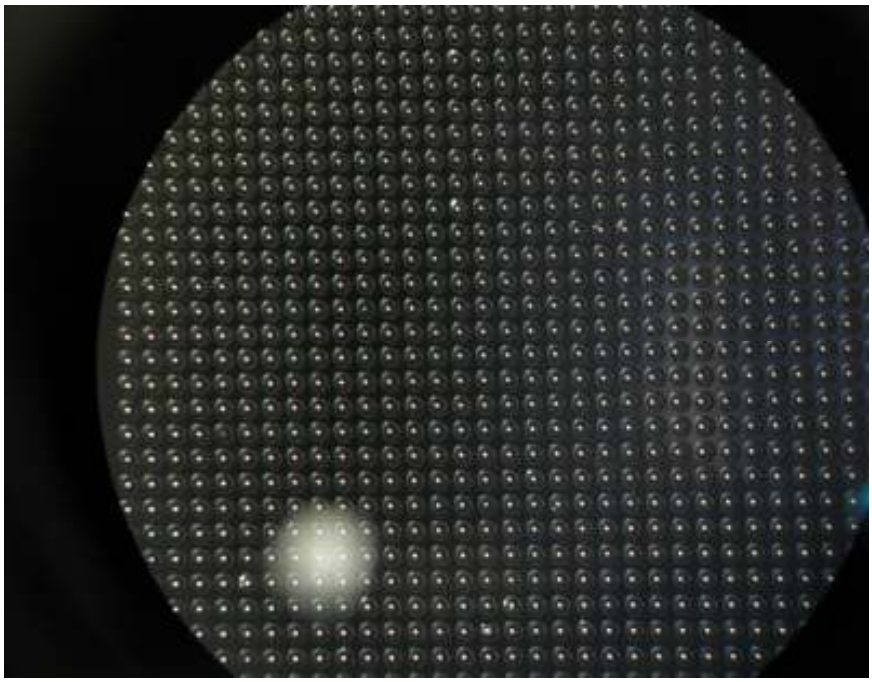

Figure 3.8: Magnified wide view of array of etched resonators from cavity side

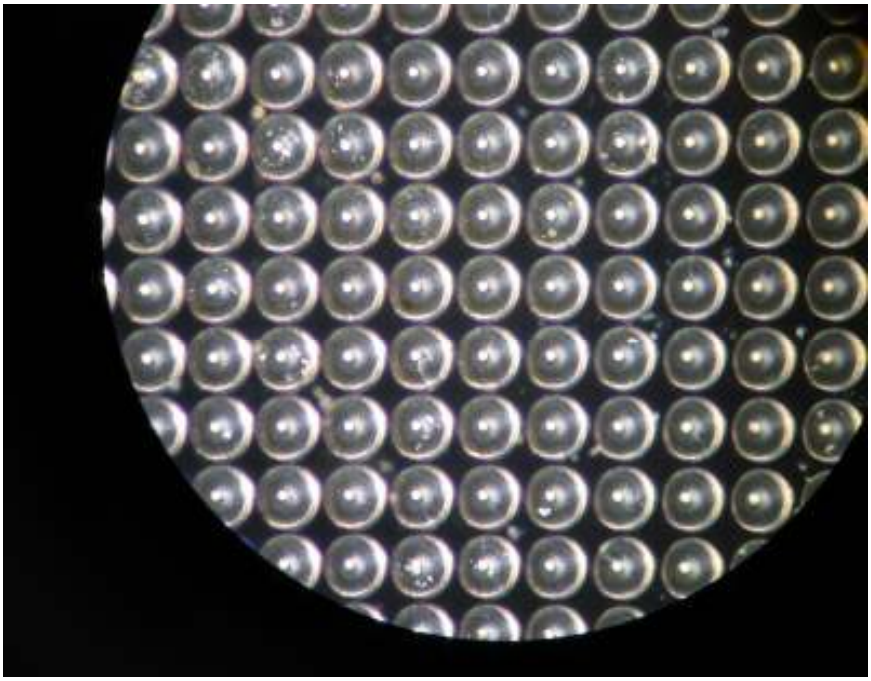

Figure 3.9: Closer view of resonator cavities and necks

Figure 3.10: Picture of resonator box

3.3 Control Box Fabrication

The control box was fabricated using fewer steps, but used the same techniques as the resonator box. One inch squares were diced from a standard 1000 μm thick wafer. The glass was anodically bonded to the unetched silicon wafer squares, and the squares were assembled into a box shape using Krazy Glue. The completed assembled control box is shown in Figure 3.11.

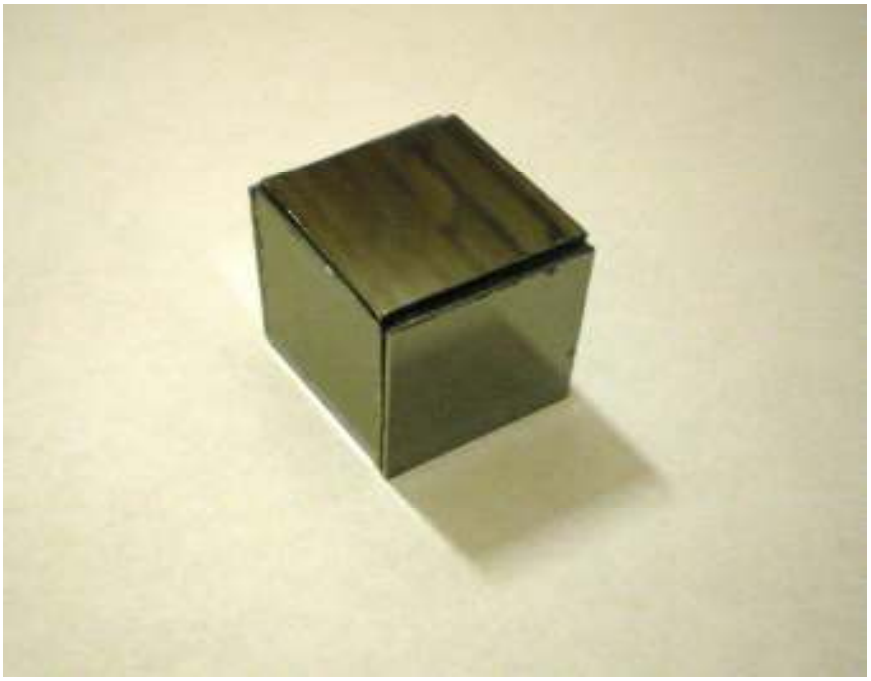

Figure 3.11: Picture of control box

‘

Chapter 4: Experimental Setup

This chapter describes the equipment used to conduct the various tests on the resonator and control boxes.

4.1 Evaluation Procedure

The experiments were all performed in an acoustic isolation chamber as shown in Figure 4.1. Inside the chamber, the experimental test setup consisted of a large stand upon which one quarter inch diameter microphone was placed in a drilled hole in the bottom of a steel plate on top of the stand. This setup allowed the diaphragm of the microphone to be placed inside the one inch square boxes used for testing. The microphone was placed under the boxes to simulate a MEMS gyroscope being surrounded by the acoustic metamaterial filter composed of a one-dimensional array of Helmholtz resonators.

Figure 4.1: The acoustic isolation chamber

4.2 Rate Table

The boxes were sealed to the steel plate by using putty as shown in Figure 4.2. The putty used in this experiment was DAP Blue Stik reusable adhesive putty. A. The large stand mentioned previously is an Aerotech Single-axis Rate Table with a large aluminum baseplate mounted to the device for stability, shown in Figure 4.3. For the purposes of this experiment, the rate table was not moving; it was only used as a convenient stand with sufficient mass to minimize vibrations.

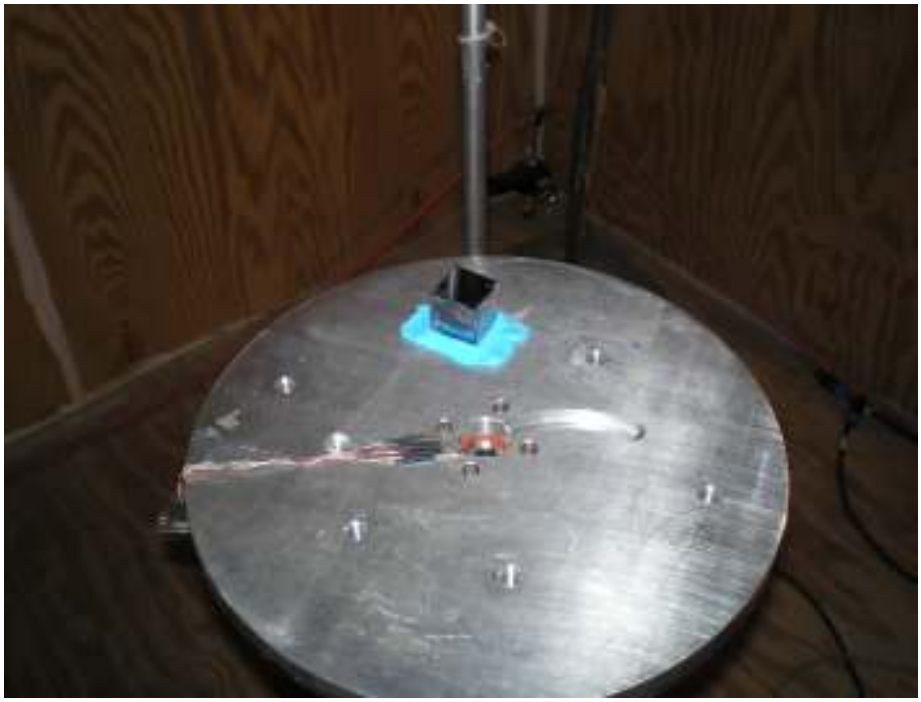

Figure 4.2: Control box sealed to test stand with putty

Figure 4.3: Test stand and speaker

4.3 Microphone

The microphone used was a Brüel & Kjaer Type 4135 ¼" Free-field microphone. This microphone has a frequency range from 4 Hz to 100 kHz and a dynamic range from 28 dB to 164 dB and a sensitivity of 4 mV/Pa [51]. This microphone, shown in Figure 4.4, was completely covered by the resonator and control box during testing. Due to the limitation of only having one microphone, the resonator box and control box were tested separately. This meant picking up one box and replacing it with another to perform testing.

The gap between the aluminum baseplate and the resonator box and the gap between the microphone base and the drilled hole in the baseplate was sealed with putty. These holes were

sealed at the top and bottom using putty to reduce sound transmission into the box as much as possible.

Figure 4.4: Brüel & Kjaer type 4135 microphone on test stand

4.4 Data Collection

The experiment was controlled from a station outside of the acoustic isolation chamber as shown in Figure 4.5. One computer was used to control the noise input and the laptop was used to read the data from the microphone. The noise was generated using a software package known as NCH Tone Generator, shown in Figure 4.6. This is a diverse software package that allows many different forms of noise to be selected, as well as sweeps across frequency spectrums using multiple tones. The hardware the microphone was connected to was a Brüel & Kjaer type 2827-

002, shown in Figure 4.7 on top of the amplifiers. This hardware was connected directly to the laptop shown in Figure 4.6 where the software package Brüel & Kjaer PULSE Labshop version 10.1 collected and recorded the response of the microphone. The PULSE Labshop software is shown in Figure 4.8.

Figure 4.5: Control station for the experiments

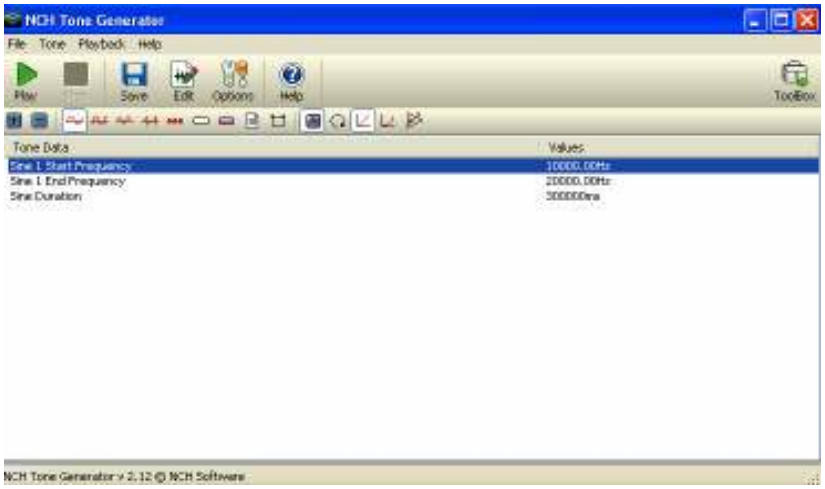

Figure 4.6: NCH Tone Generator software

Figure 4.7: Brüel & Kjaer type 2827-002 on top of Crown XTi-1000 amplifiers

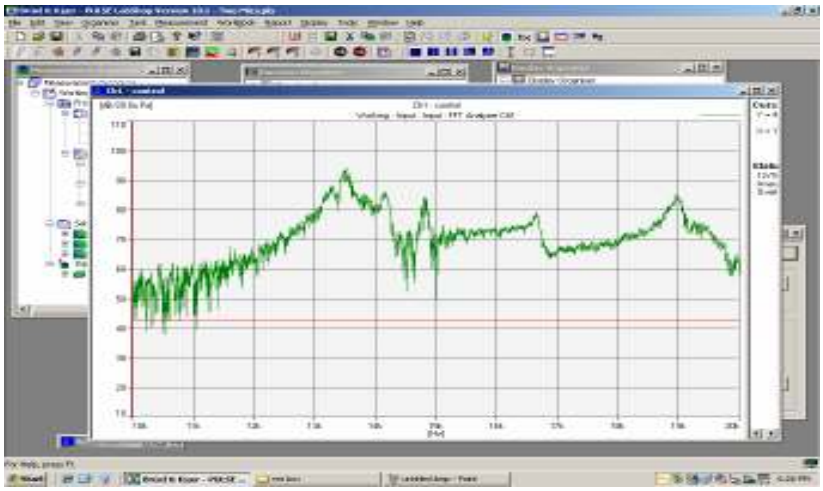

Figure 4.8: Brüel & Kjaer PULSE Labshop version 10.1 software

4.5 Amplifier

The acoustic noise was generated in the NCH Tone Generator and then routed electrically through the computer's sound card where it was then routed to a Crown XTi-1000 Amplifier. This amplifier was used to control the power level of the noise generated by the NCH Tone

Generator. The amplifier was connected to the speaker that was suspended above the boxes. The amplifier used is shown in Figure 4.7 below the Brüel & Kjaer type 2827-002. Although two amplifiers are shown in Figure 4.7 only one was needed for the testing in this thesis.

4.6 Speaker

A speaker was used to transmit the acoustic noise from the NCH Tone Generator software to the boxes and microphone. The type of speaker used was a VHF-100 Driver made by Community Speakers. This speaker is capable of producing sound up to 140 dB in power at frequencies larger than 12 kHz. The speaker is shown suspended above the test boxes in Figure 4.9.

Figure 4.9: Community Speakers VHF-100 Driver used to generate noise

Chapter 5: Evaluation

This chapter describes the testing performed on the resonator and control boxes to determine how effective the acoustic metamaterial is at attenuating sound at and around the designed resonant frequency of 14.5 kHz.

5.1 Sine Sweep

To test the effectiveness of the acoustic metamaterial at sound attenuation, the resonator and control boxes were first subjected to a sine sweep across the acoustic spectrum from 10 kHz to 20 kHz. The area of most significance is the area around 14.5 kHz where the resonators are designed to attenuate sound. The sine sweep was performed two ways. The first sine sweep set of tests involved varying the power level of the sine sweep, and the second sine sweep set of tests involved varying the distance of the sound source from the boxes.

5.1.1 Sine Sweep at Varying Power Levels

The first sine sweep test involved varying the power level of the sine sweep to determine if the resonators behaved differently when subjected to different sound power levels. The sound source was maintained at a constant distance of 36 inches directly above the boxes.

Figures 5.1 through 5.5 show the response of the acoustic metamaterial resonator box to a sine sweep of five different power levels. Figures 5.6 through 5.10 show the response of the control box to the same set of tests. Both the resonator and control box maintained near identical

responses as the sine sweep increased in power level five times. It does not appear that an increase in power level has any significant effect on the response of the microphone inside the box. However, the power level was not varied over a large scale due to limitations in the hardware available. The power level was only varied about 20 dB from power level 1 to power level 5.

Figures 5.1 through 5.5 show the response of the resonator box to varying power levels. These figures demonstrate an interesting dip in the sound power level around 14.5 kHz. The control box also shows a similar dip around 14.5 kHz, shown in Figures 5.6 through 5.10; however, the dip shown for the resonator box shows a significantly greater attenuation. The control box shows a dip of at most 16 dB, while the resonator box shows a dip of at most 34 dB. This shows the resonator box is 18 dB more effective in attenuating noise at the target frequency of 14.5 kHz than the control box. The drop in sound power level is noticeable and repeatable through each experiment as the power level was increased. The bandwidth of attenuation is in the form of a notch filter with the largest attenuation occurring at approximately 14.4 kHz with gradually decreasing attenuation on either side as shown in Figure 5.1.

The micro version of the Helmholtz resonators seem to be successful at attenuating sound, but do not share the same limitation as their macro counterparts, and the same limitation of many acoustic metamaterials, a relatively narrow band of attenuation. Oppositely, this acoustic metamaterial has a much larger bandwidth of attenuation, approximately 700 Hz. The most likely reason for this large band is the tolerances of the microfabricated resonators. Even a small change in the length of the neck or cavity creates a slight change in the resonant frequency of that individual resonator. For this reason it seems likely, due to manufacturing tolerances, that each resonator would not resonate at precisely the same frequency. This tolerance error appears

to work in a positive way causing a large bandwidth of attenuation. Table 5.1 below shows the tabulated results from each test performed in this thesis.

Test	Box	Figures	Configuration	Greatest Attenuation near 14.5 kHz	Resonator Attenuation
0	Resonator	5.1-5.5	Increasing Power Levels	34 dB	18 dB
0	Control	5.6-5.10	Increasing Power Levels	16 dB	
1	Resonator	5.11-5.14	Increasing Distance From Sound Source	34 dB	14 dB
1	Control	5.15-5.18	Increasing Distance From Sound Source	20 dB	
2	Resonator	5.23-5.26	Increasing Distance From Sound Source	27 dB	Inconclusive
2	Control	5.27-5.30	Increasing Distance From Sound Source	0 dB	
3	Resonator	5.31-5.33	Increasing Distance From Sound Source	11 dB	Inconclusive
3	Control	5.34-5.36	Increasing Distance From Sound Source	9 dB	
4	Resonator	5.37-5.39	Increasing Distance From Sound Source	17 dB	Inconclusive
4	Control	5.40-5.42	Increasing Distance From Sound Source	26 dB	
5	Resonator	5.44-5.46	Increasing Distance From Sound Source	10 dB	Inconclusive

Table 5.1: Table of results

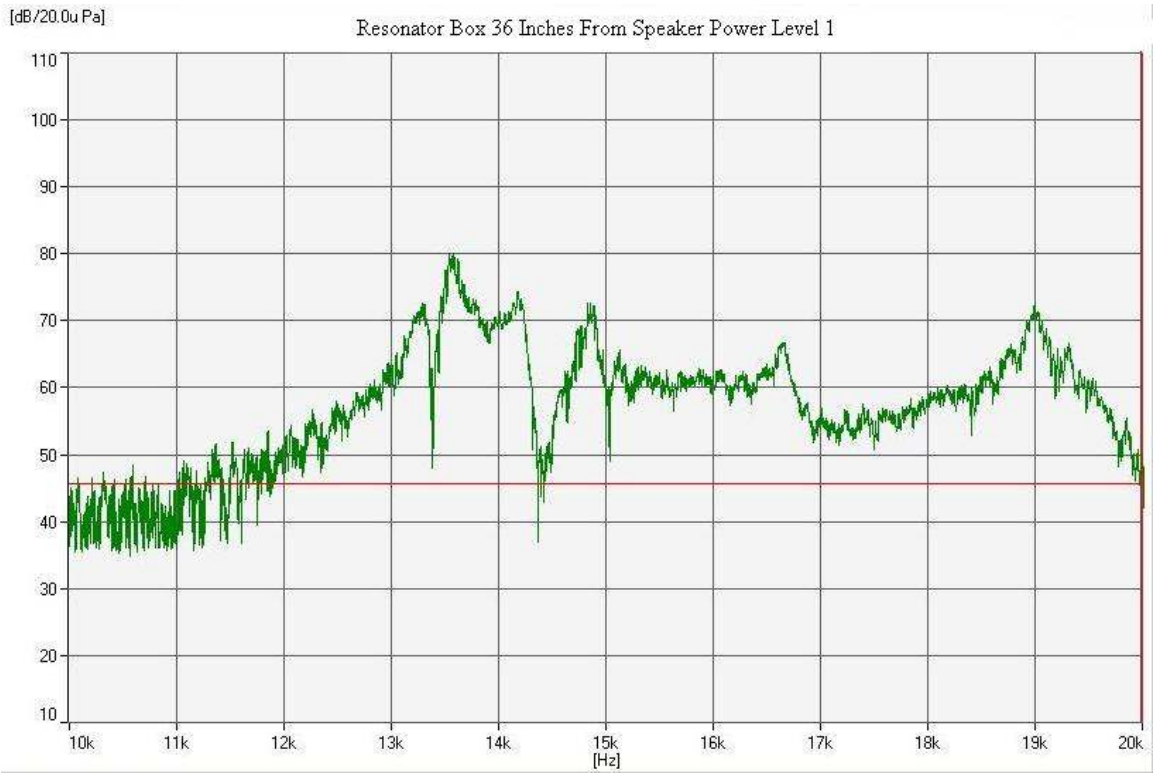

Figure 5.1: Resonator box 36 inches from sound source power level 1

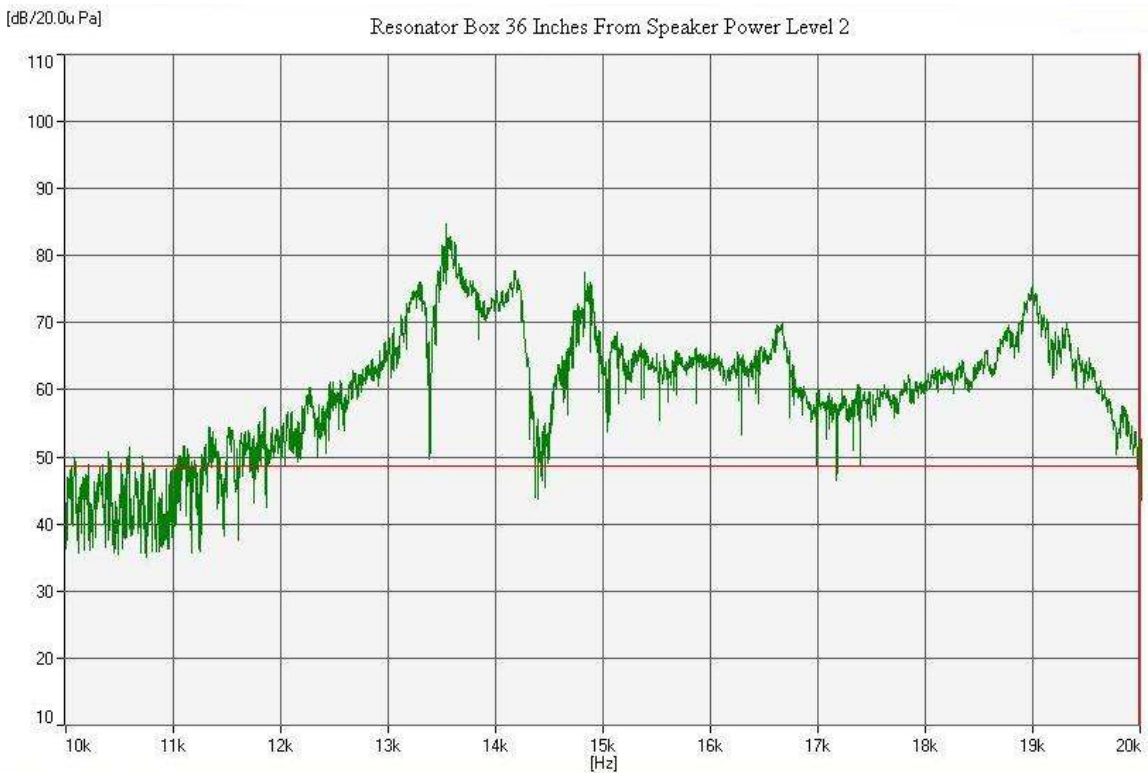

Figure 5.2: Resonator box 36 inches from sound source power level 2

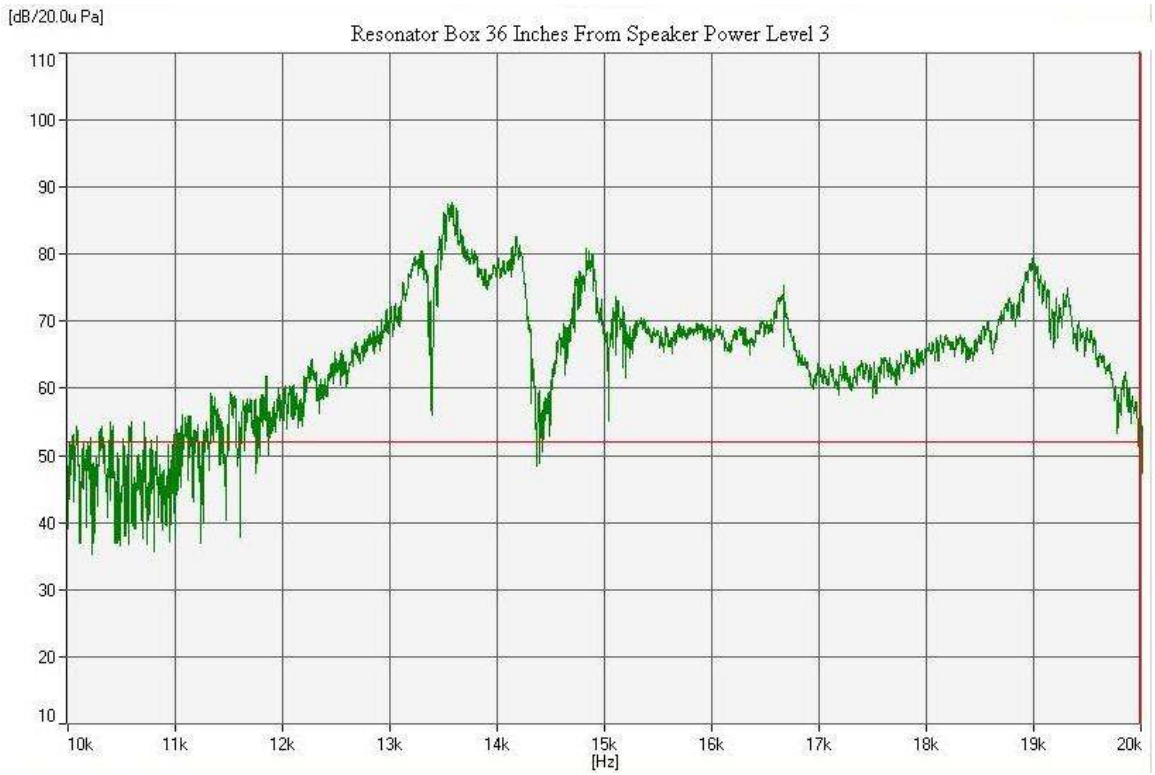

Figure 5.3: Resonator box 36 inches from sound source power level 3

Figure 5.4: Resonator box 36 inches from sound source power level 4

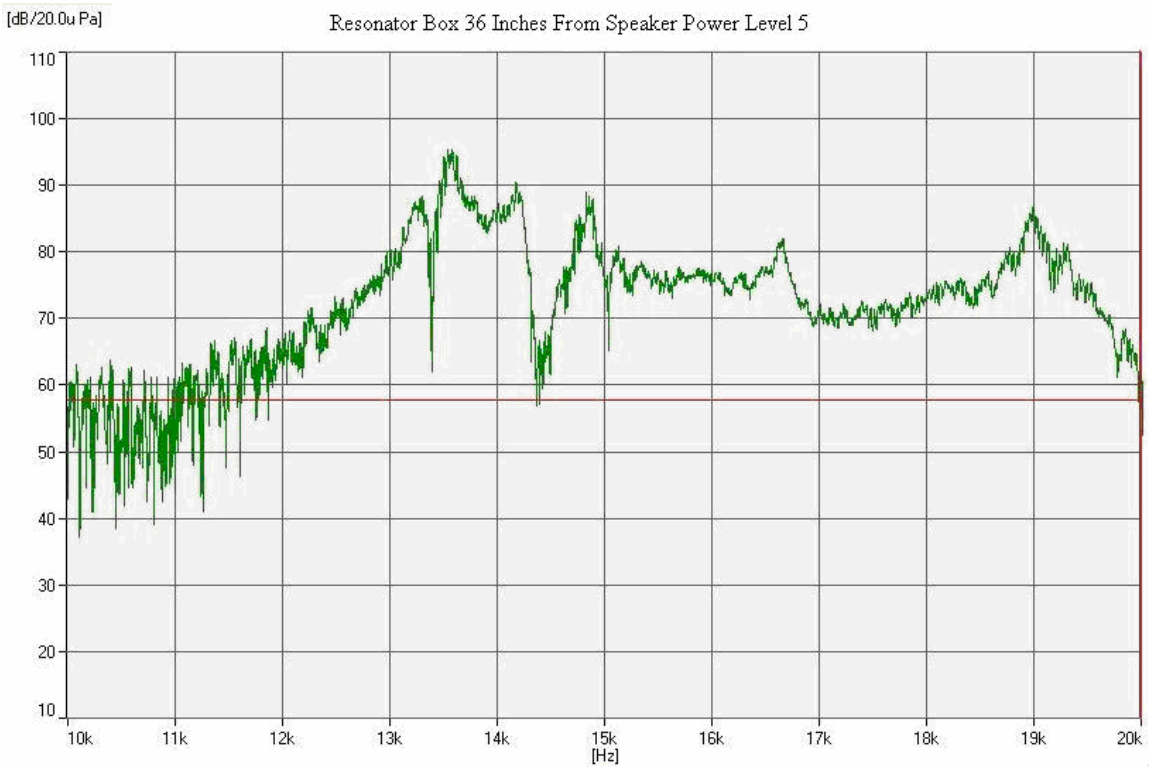

Figure 5.5: Resonator box 36 inches from sound source power level 5

Figure 5.6: Control box 36 inches from sound source power level 1

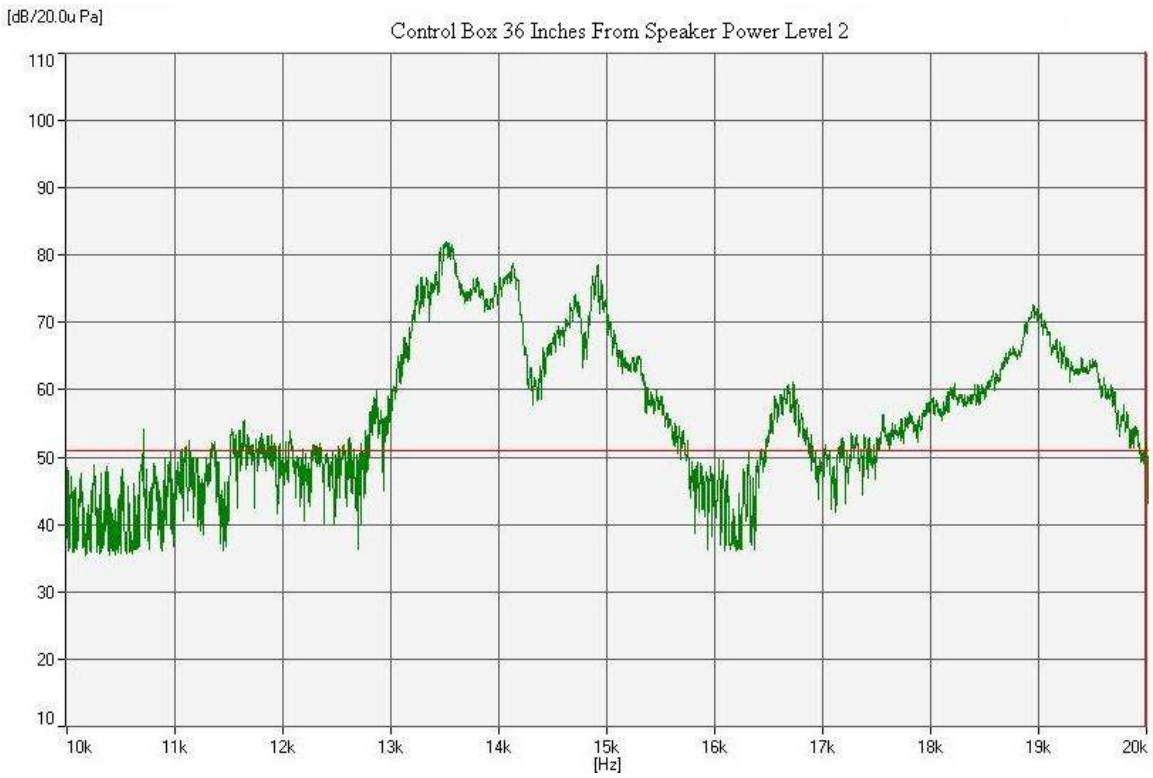

Figure 5.7: Control box 36 inches from sound source power level 2

Figure 5.8: Control box 36 inches from sound source power level 3

Figure 5.9: Control box 36 inches from sound source power level 4

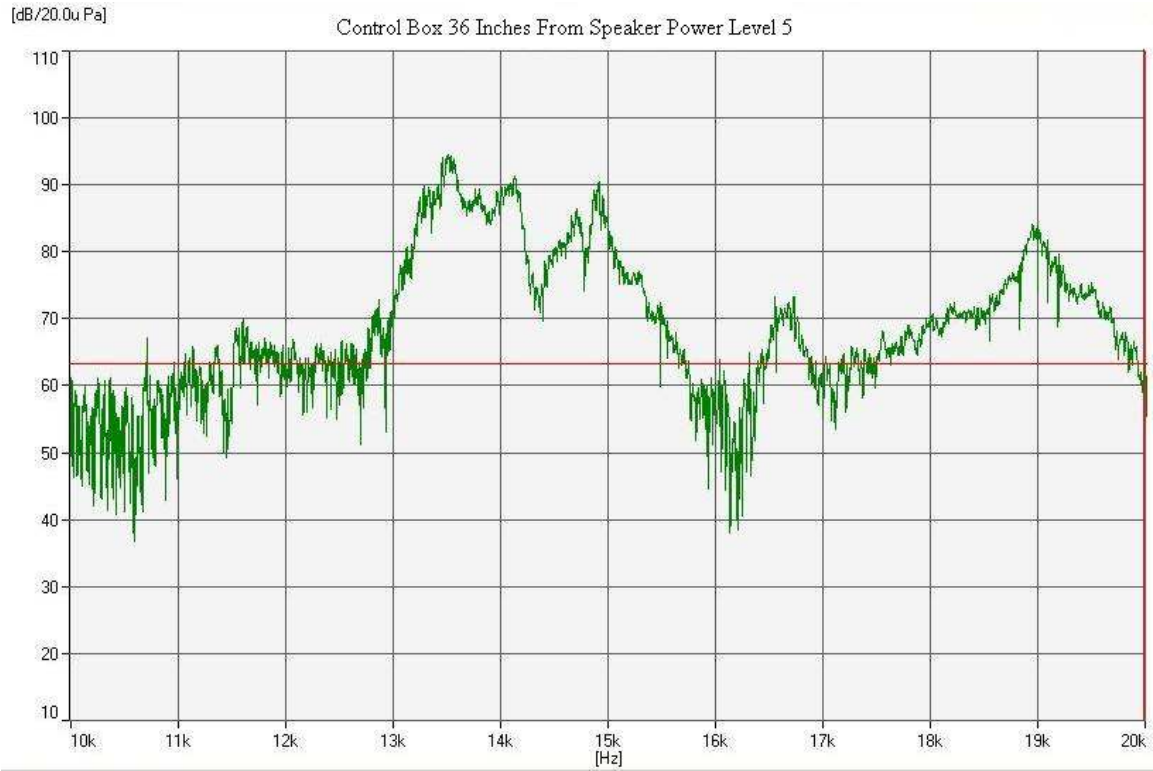

Figure 5.10: Control box 36 inches from sound source power level 5

5.1.2 Sine Sweep at Varying Distances From Noise Source

The next test performed with the sine sweep function was to see if the acoustic metamaterial resonator box would perform differently depending on the distance of the box from the sound source. The speaker acting as the sound source was mounted on a stand that allowed the height of the speaker above the test stand and the boxes to be adjusted. The sine sweep was performed at a constant power level from four varying distances: 12 inches, 24 inches, 36 inches, and 48 inches away from the sound source.

Figures 5.11 through 5.14 show the resonator box at varying distances from the sound source, and Figures 5.15 through 5.18 show the control box at varying distances from the sound source. The acoustic metamaterial again attenuates sound near the 14.5 kHz goal. The most attenuation in the tests occurred at the 48 inch distance. At this distance the resonator box showed an attenuation of 34 dB. However, the attenuation at 12 inches was still 28 dB. The distance from the sound source does appear to have a small effect on the attenuation amount, but only about 6 dB over a distance change of 36 inches.

The resonator box shows a similar response as the sound source is moved away, but not an identical response as seen in Figures 5.1 through 5.10 where the power level is increased each time, but the response remains nearly identical. In Figures 5.11 through 5.18, the response changes as the sound source is moved further away. Many peaks and valleys remain the same, but not all. This holds true for both the resonator and control box.

The control box does not have the same response as the resonator box. However, it does have similar peaks and valleys, and the sound attenuation that occurs near the designed resonant frequency of 14.5 kHz is also shown on the control box, but the attenuation is consistently

smaller. For example, at 48 inches the resonator box shows an attenuation of 34 dB over a 700 Hz bandwidth, while the control box at the same distance shows an attenuation of 20 dB over the same 700 Hz bandwidth. The resonator box attenuated noise 14 dB more than the control box at the target frequency of 14.5 kHz. The bandwidth of attenuation remained very nearly the same over each distance for both the resonator and control box.

Figures 5.19 through 5.22 show the response of the microphone without a box placed over it at varying distances from the sound source. The noise of the signal varies as the distance between the microphone and the source changes, but the signal maintains the same approximate shape. The microphone maintained this same type of response for every batch of tests conducted, however, only one set of tests is shown.

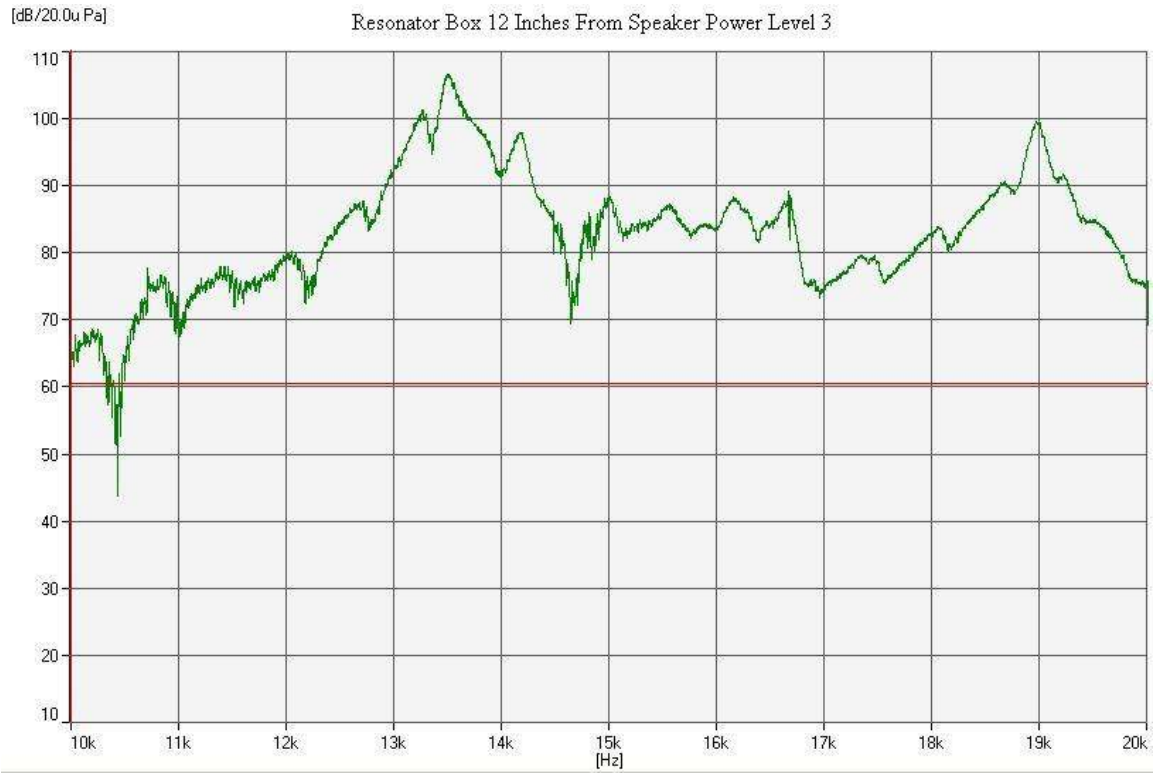

Figure 5.11: Resonator box 12 inches from sound source test 1

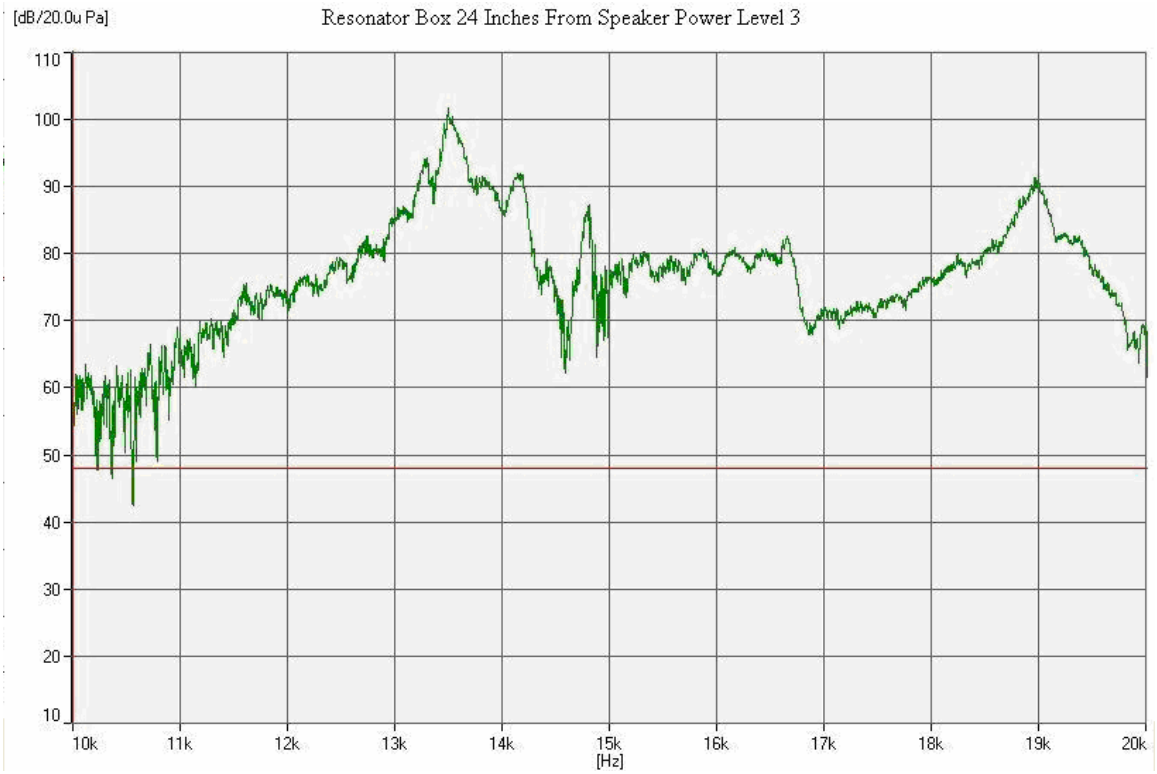

Figure 5.12: Resonator box 24 inches from sound source test 1

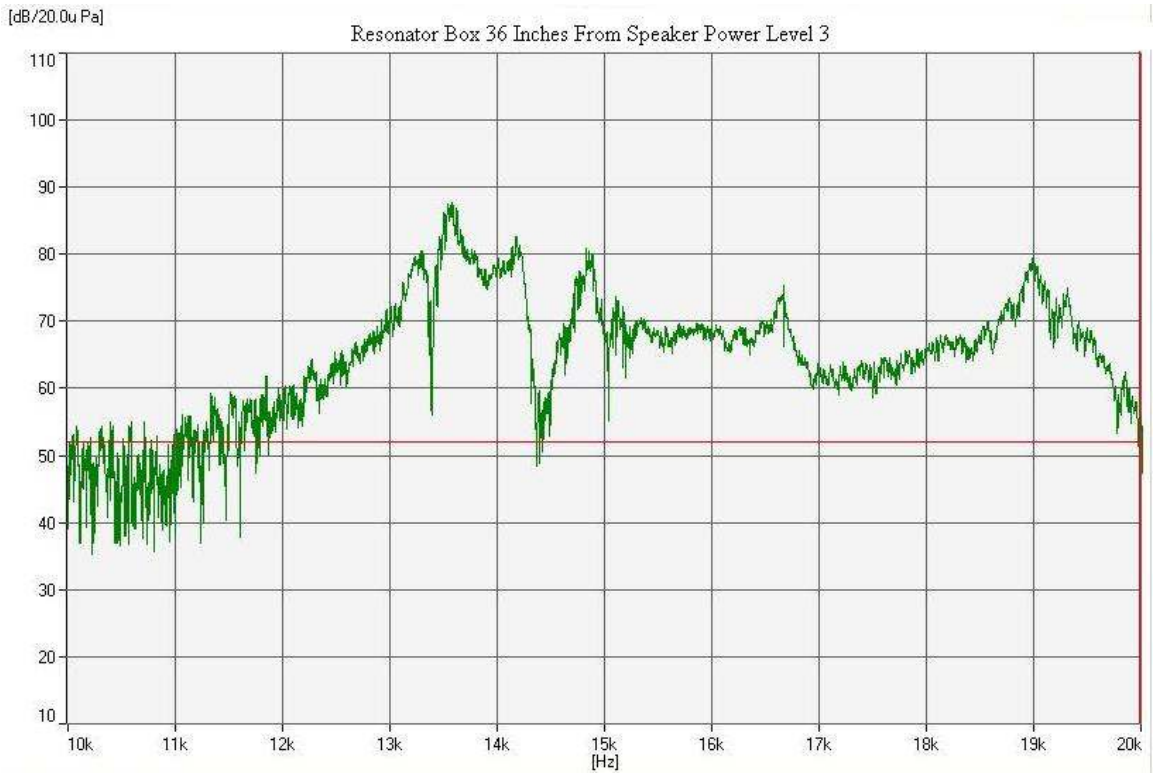

Figure 5.13: Resonator box 36 inches from sound source test 1

Figure 5.14: Resonator box 48 inches from sound source test 1

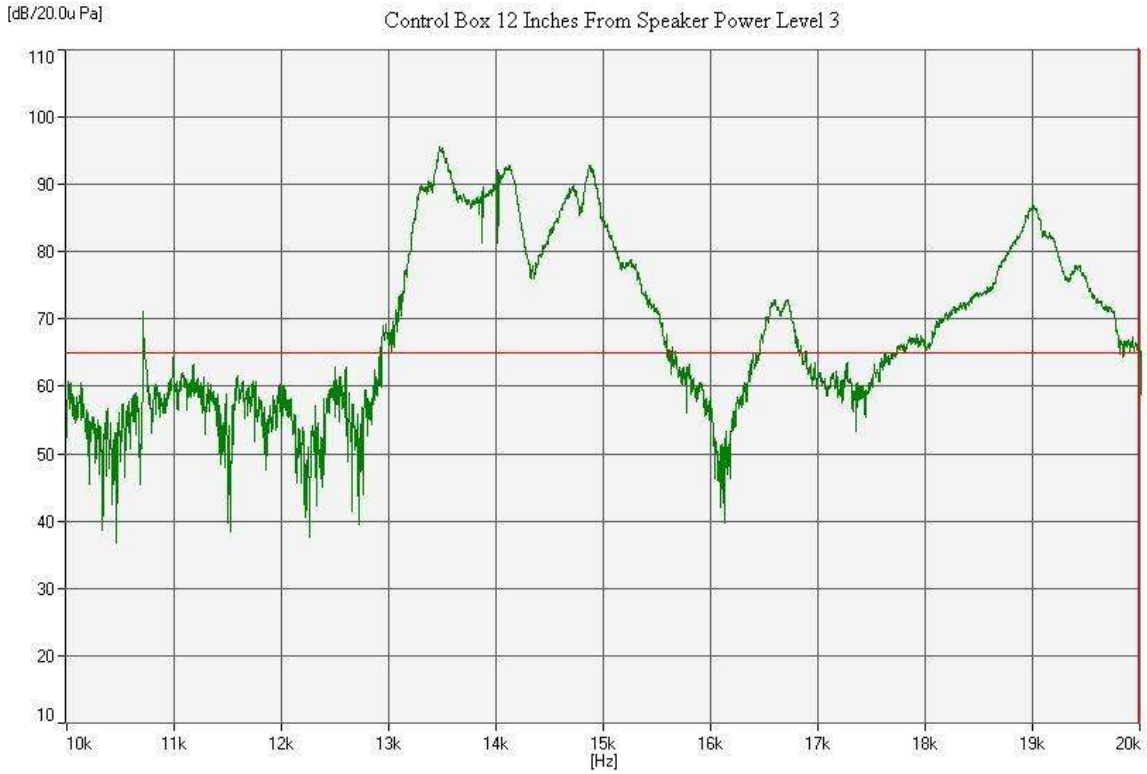

Figure 5.15: Control box 12 inches from sound source test 1

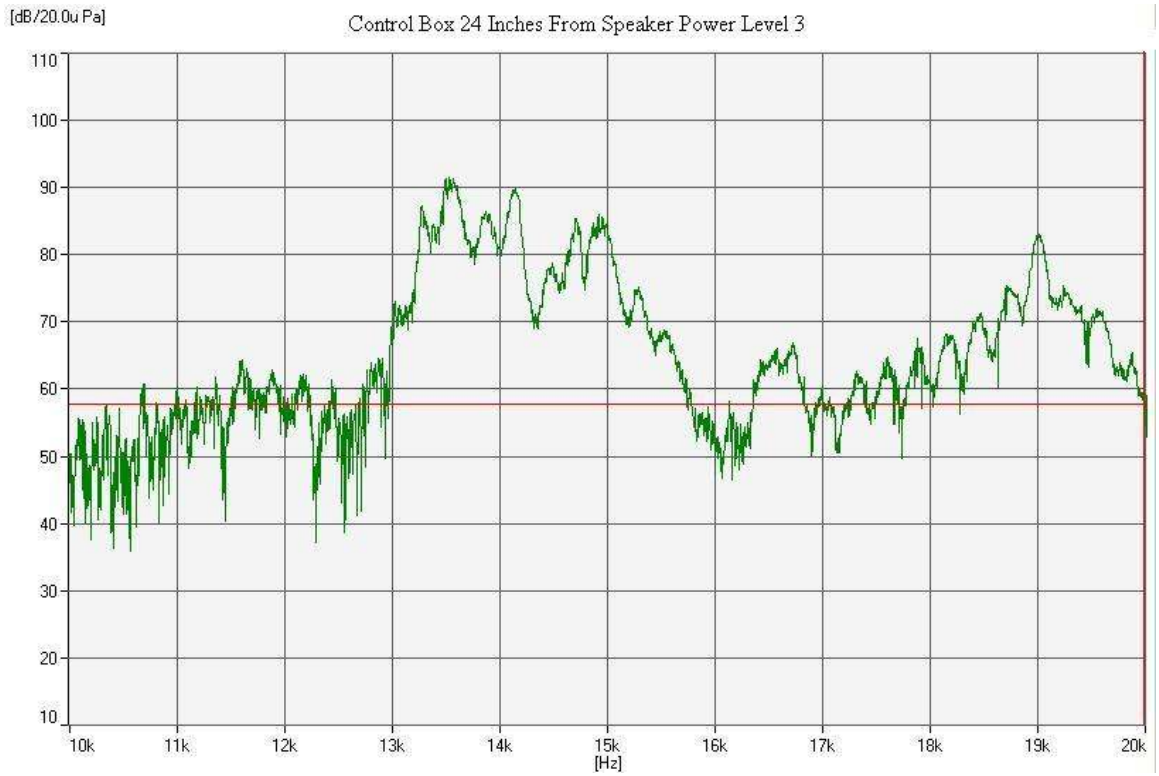

Figure 5.16: Control box 24 inches from sound source test 1

Figure 5.17: Control box 36 inches from sound source test 1

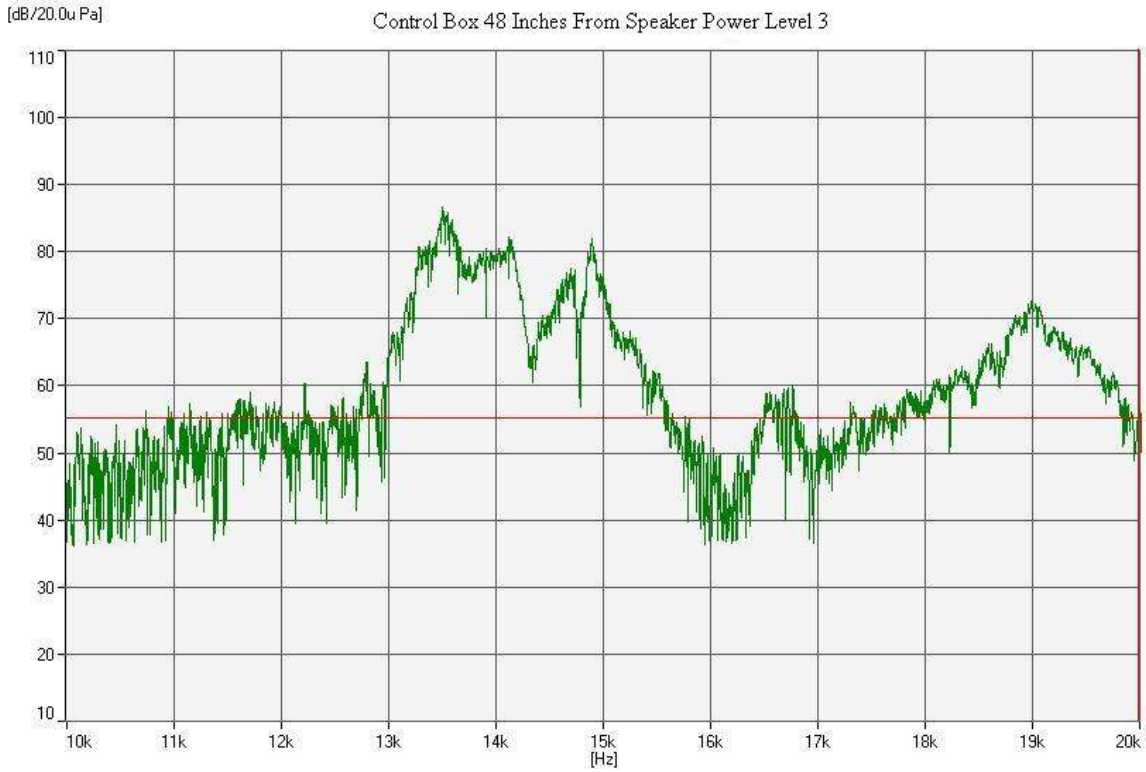

Figure 5.18: Control box 48 inches from sound source test 1

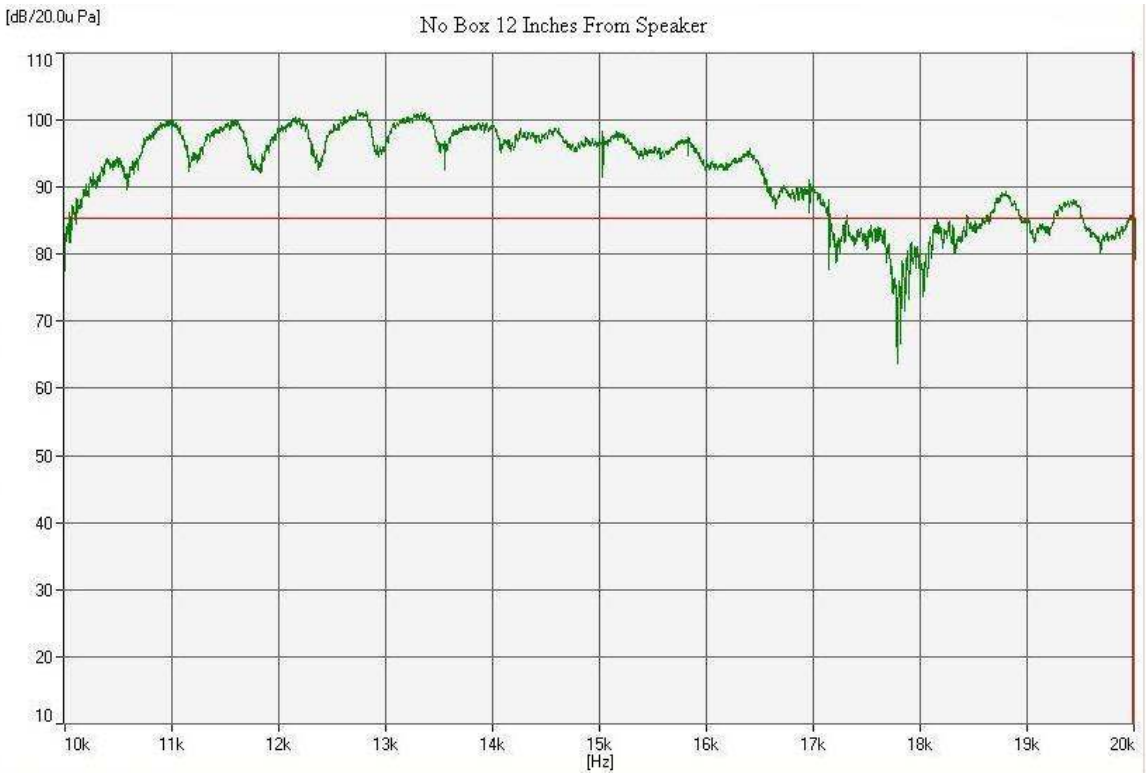

Figure 5.19: No Box 12 inches from sound source

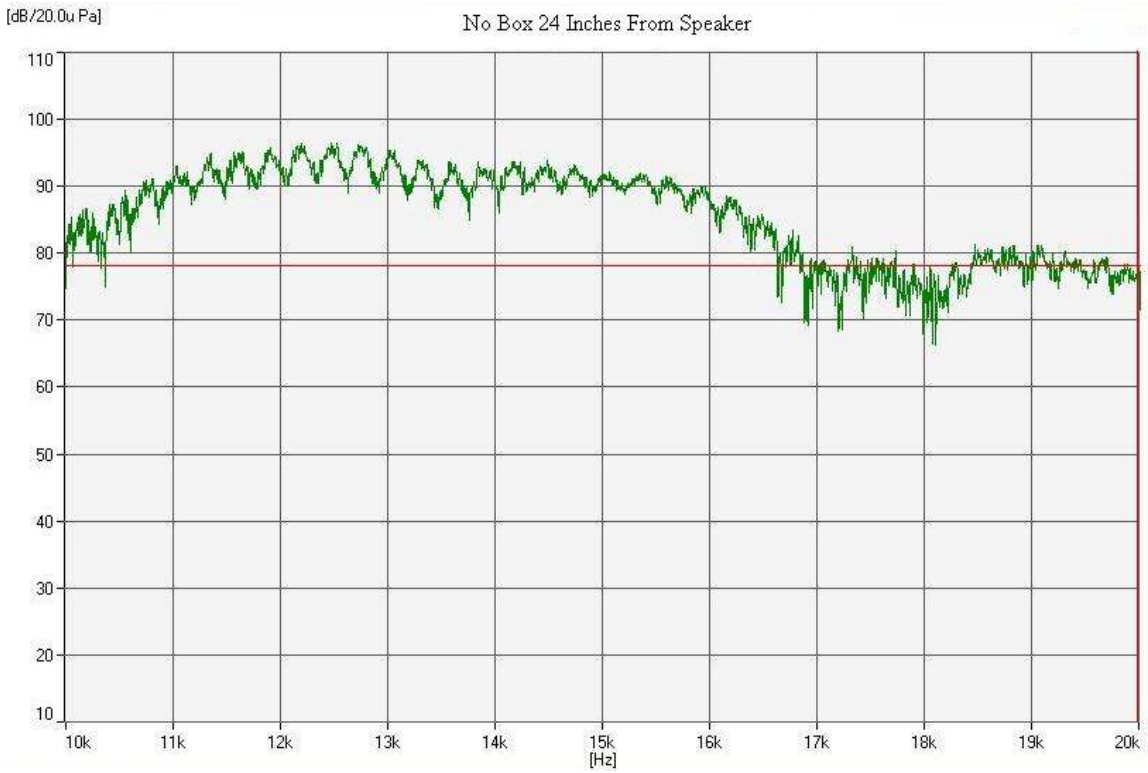

Figure 5.20: No Box 24 inches from sound source

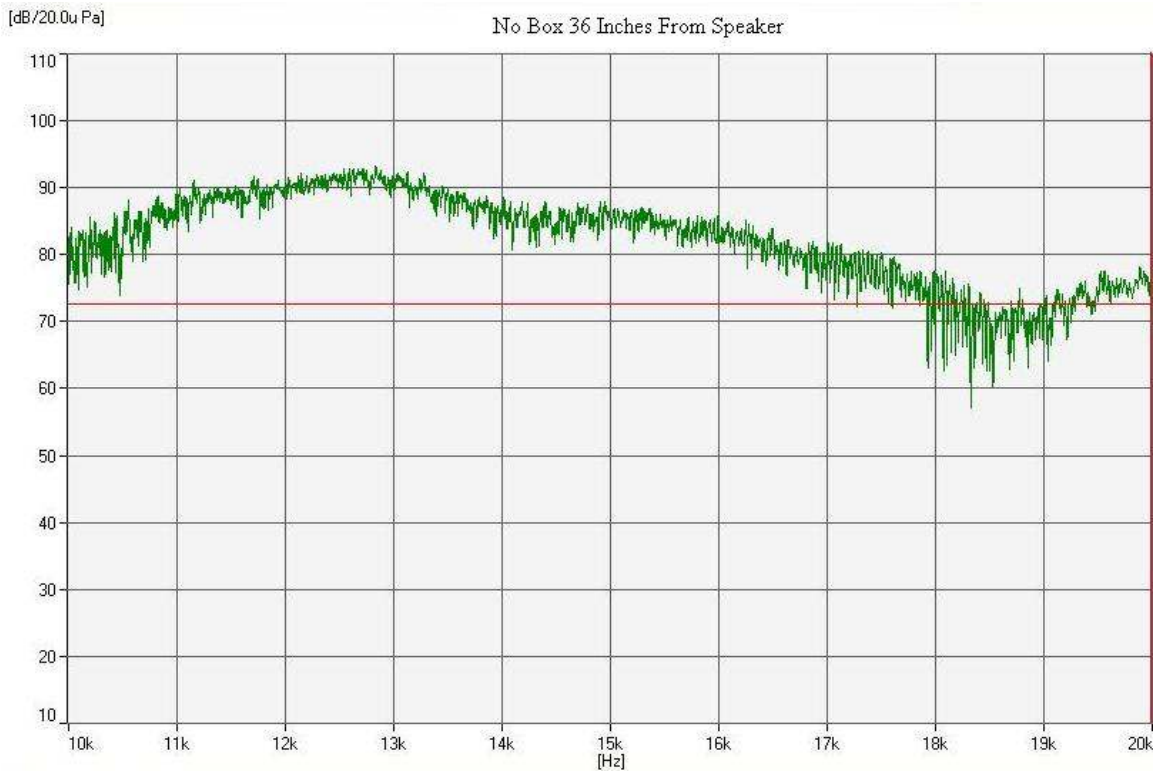

Figure 5.21: No Box 36 inches from sound source

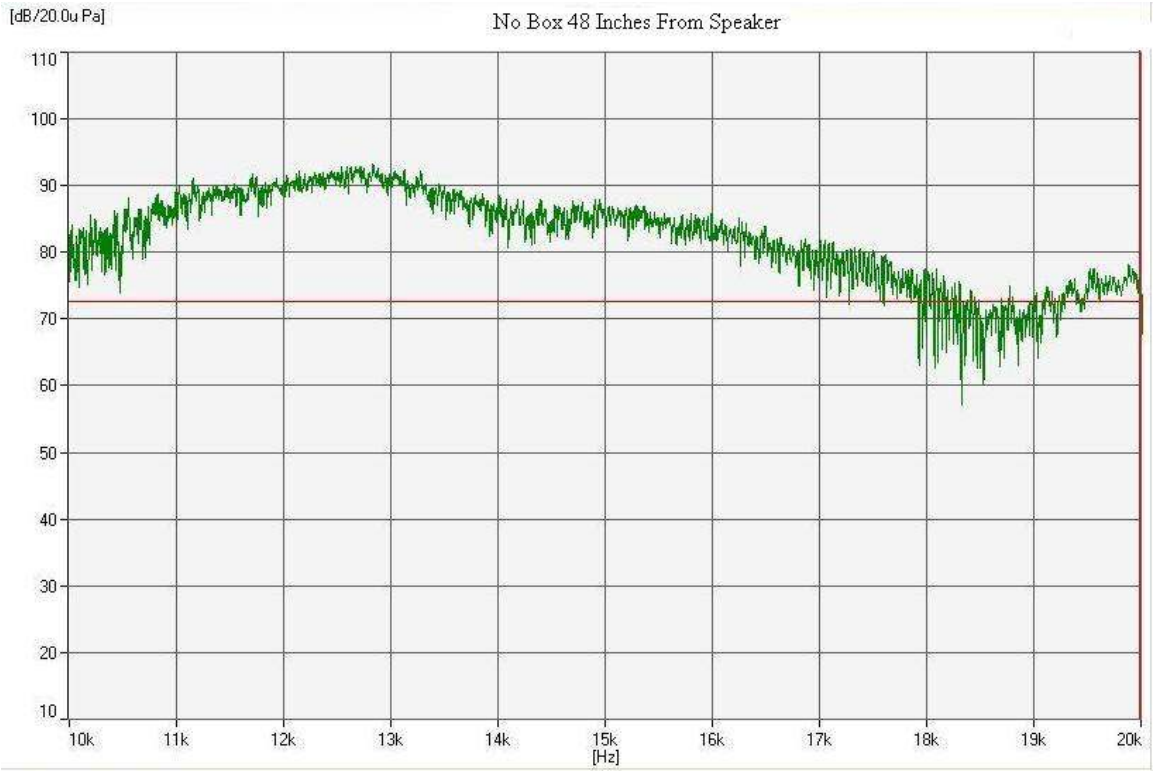

Figure 5.22: No Box 48 inches from sound source

5.2 Effect on Response of Moving the Boxes

Through the course of testing, an unexpected effect was observed as the boxes were taken off the putty and replaced for another identical test. The response of the box was significantly different after being removed from the putty and test stand and then replaced; despite the same distances, orientation, and power level being applied. Tests 2 through 5 shown below in Figures 5.23 through 5.49, show that the resonator box shows less attenuation for each subsequent test. For test 2, shown in Figures 5.23 through 5.30, the resonator box still shows a significant effect around 14.5 kHz, as much as 27 dB attenuation. This is less than the 36 dB recorded in the previous test. Additionally, the bandwidth of attenuation is smaller, it dropped from approximately 700 Hz in test 1 to approximately 400 Hz in test 2. The control box response is also significantly different; it does not show the same dip at 14.5 kHz that it showed in previous tests.

For test 3 and beyond, the 12 inch distance test was left out because it was determined the response for each box was largely inconclusive when the source was too close to the boxes. The resonator box became progressively worse at accomplishing the task of attenuating noise at 14.5 kHz, which it accomplished in test 1 and test 2. In test 3, shown in Figures 5.31 though 5.36, the resonator box showed no effect in the 14.5 kHz range. In fact, it is nearly identical with the control box response near 14.5 kHz.

It was hypothesized that the boxes may be failing from fatigue due to either being continually removed from the putty and replaced, or due to the high frequency high power acoustic noise that the boxes were being subjected to. This could account for the changing response of the resonator and control boxes. A thorough investigation was undertaken. It was

determined that a significant design flaw is present in the size of control and resonator boxes. The box size allowed for the creation of standing waves within the box due to the wavelength of the acoustic noise corresponding closely and exactly at some frequencies with the dimensions of the box, which were one inch square. This effect is shown in Figure 5.43.

The formation of standing waves inside the box is also apparent when looking at any of the graphs that show the response of the microphone over the entire spectrum from 10 kHz to 20 kHz. According to Figure 5.43, the wavelength corresponds with the length dimension of the box near 12 kHz. Near this frequency the sound power level recorded by the microphone begins climbing substantially. This could be due to the fact that standing waves being formed inside the box are causing an increase in sound power level inside the box.

The fatigue resulting from the formation of standing waves inside the boxes caused the glue that holds the individual MEMS fabricated squares to come apart. Glue was reapplied to the boxes and another set of tests was performed on the boxes. The results of these tests for the resonator box are shown in Figures 5.44 through 5.46. It was found that reapplying the glue to the boxes had some positive effect. For example, the distances of 36 and 48 inches for the test before reapplication of the glue, Figures 5.38 and 5.39, and the test after reapplication of the glue, Figures 5.45 and 5.46, show a drop in sound power level around 14.5 kHz of nearly 10 dB. The boxes were tested at the same power level for each of these tests and show similar peaks and valleys, but resealing the boxes showed a drop in power level. This could be due to the performance of the resonators or simply due to the fact that sound was completely kept out of the box. Without a proper seal, the resonators would not perform correctly.

From this conclusion, it is recommended in future designs that the wavelength of the noise be considered during the design process to prevent the formation of standing waves inside

the box, which leads to rapid fatigue of the glue bonds holding the boxes together. The glue used in this experiment was Krazy Glue. For future experiments another type of glue should be considered to reduce or eliminate the need to reapply glue to boxes during testing.

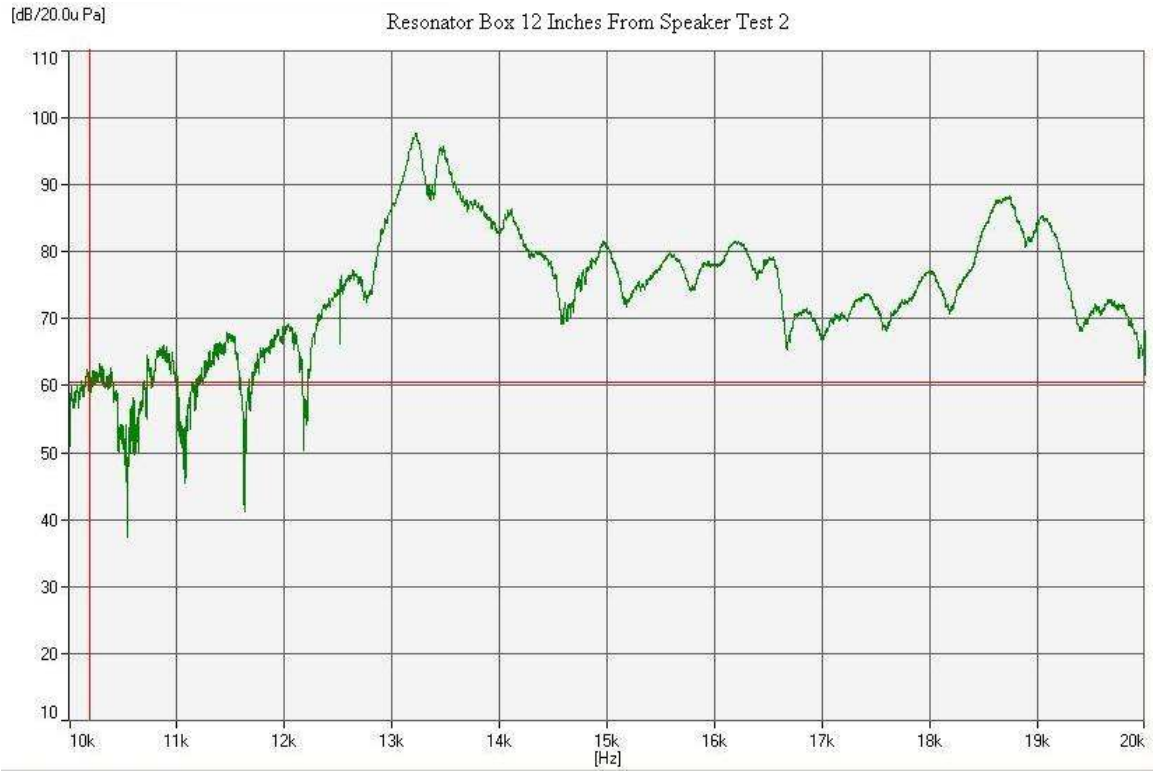

Figure 5.23: Resonator box 12 inches from sound source test 2

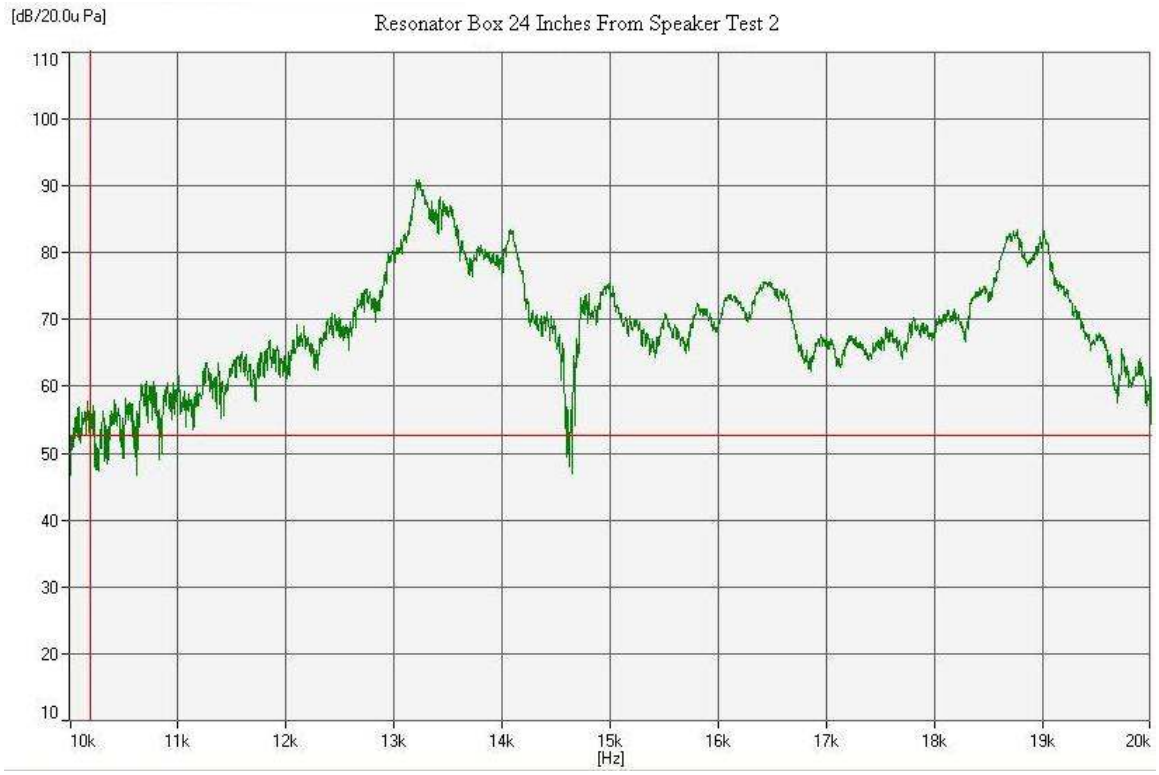

Figure 5.24: Resonator box 24 inches from sound source test 2

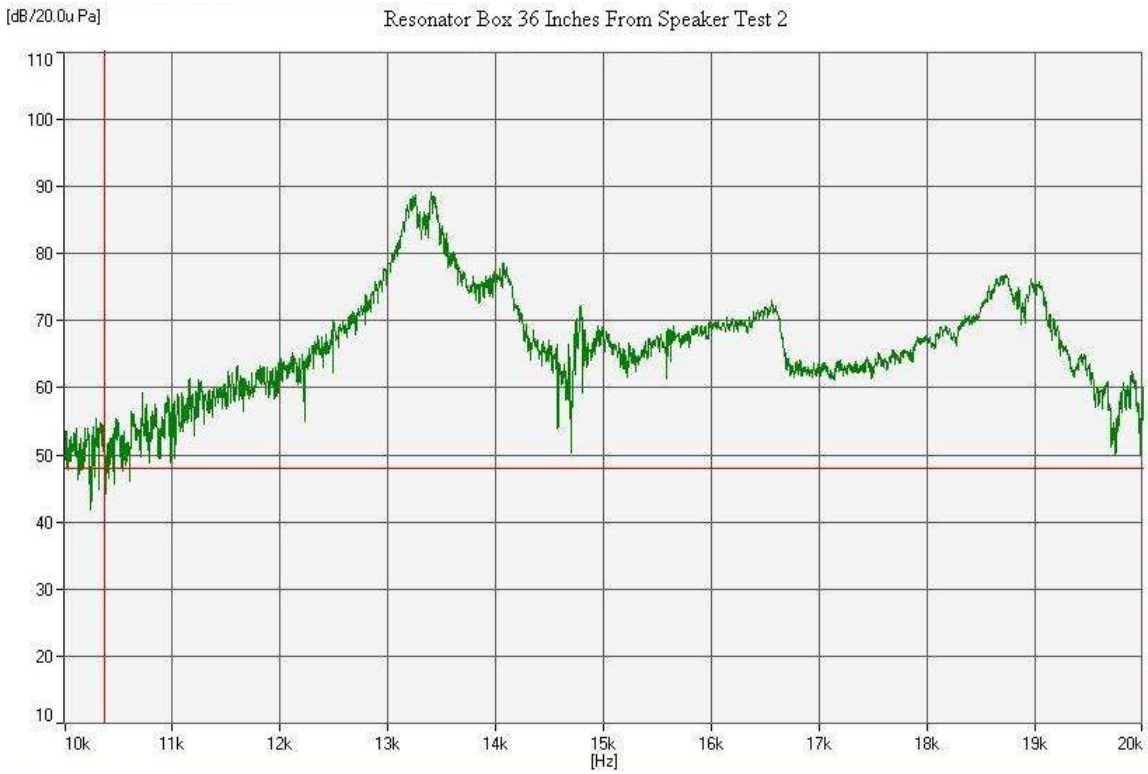

Figure 5.25: Resonator box 36 inches from sound source test 2

Figure 5.26: Resonator box 48 inches from sound source test 2

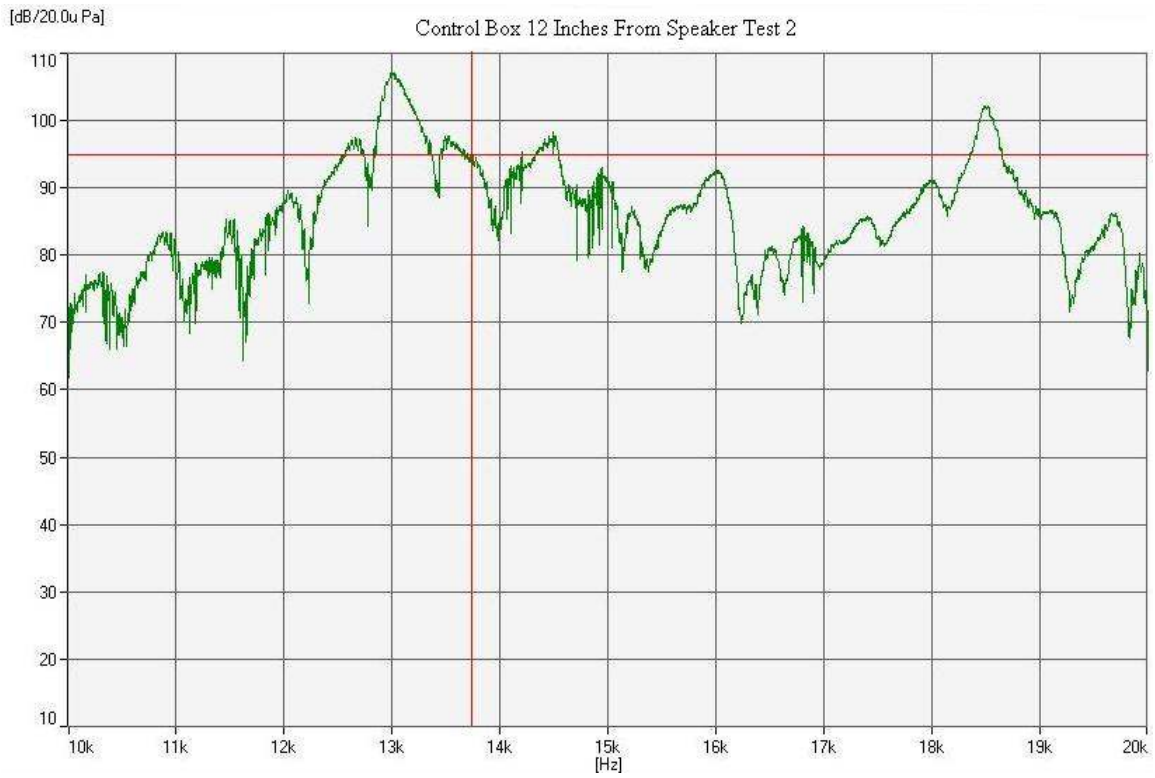

Figure 5.27: Control box 12 inches from sound source test 2

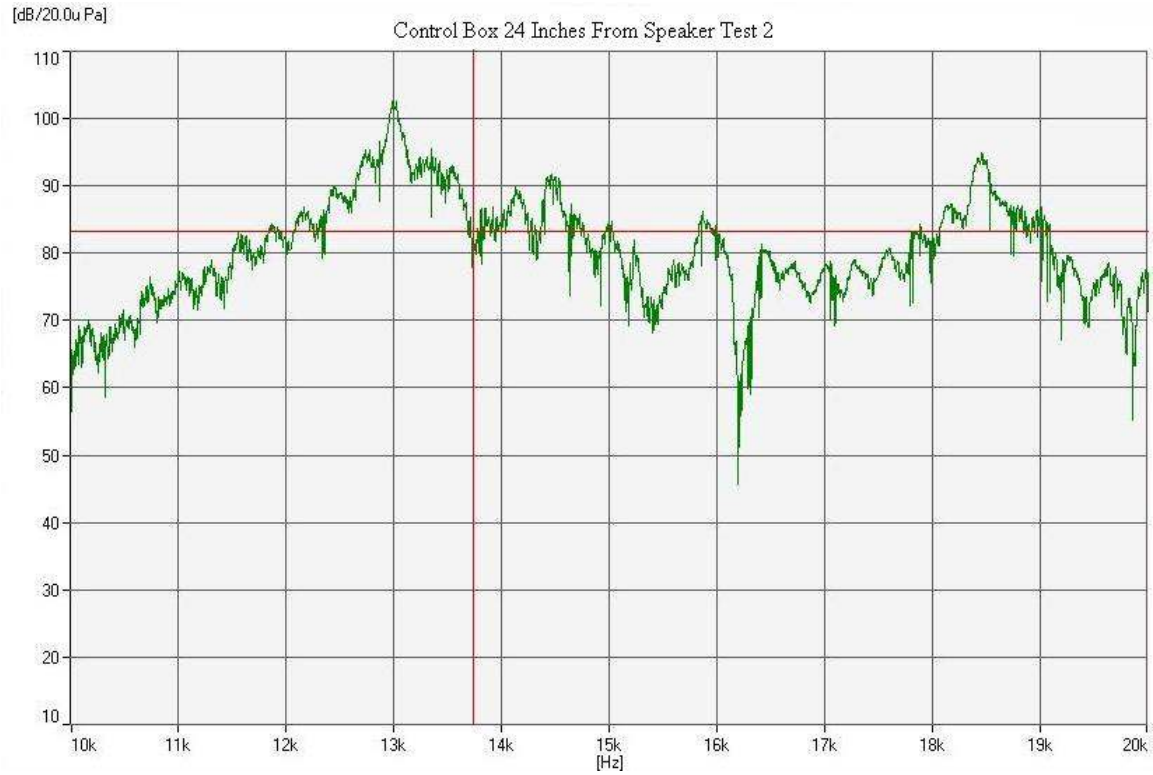

Figure 5.28: Control box 24 inches from sound source test 2

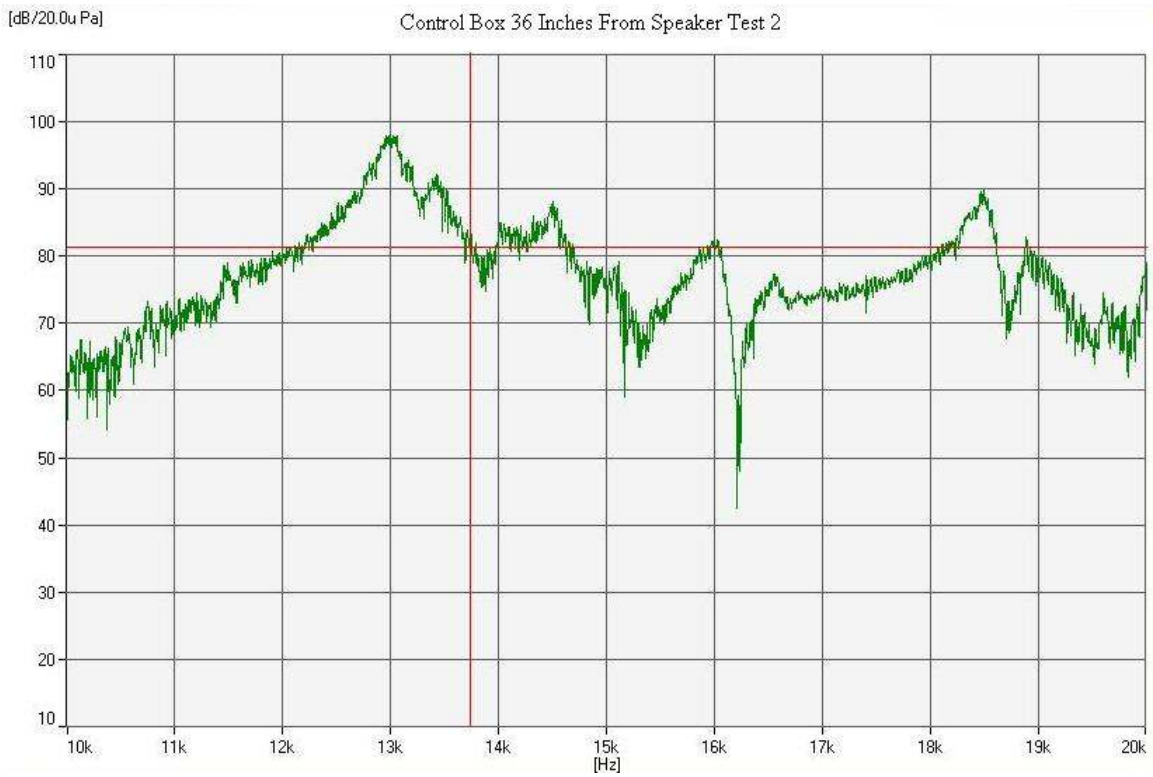

Figure 5.29: Control box 36 inches from sound source test 2

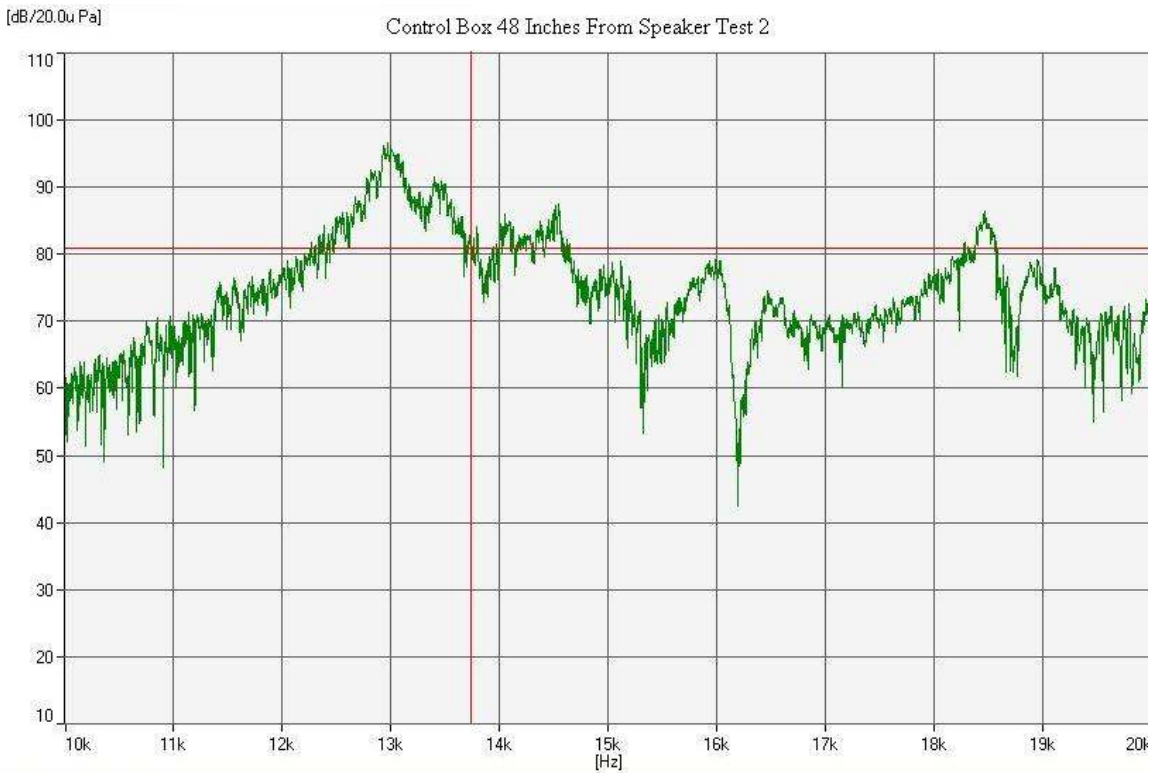

Figure 5.30: Control box 48 inches from sound source test 2

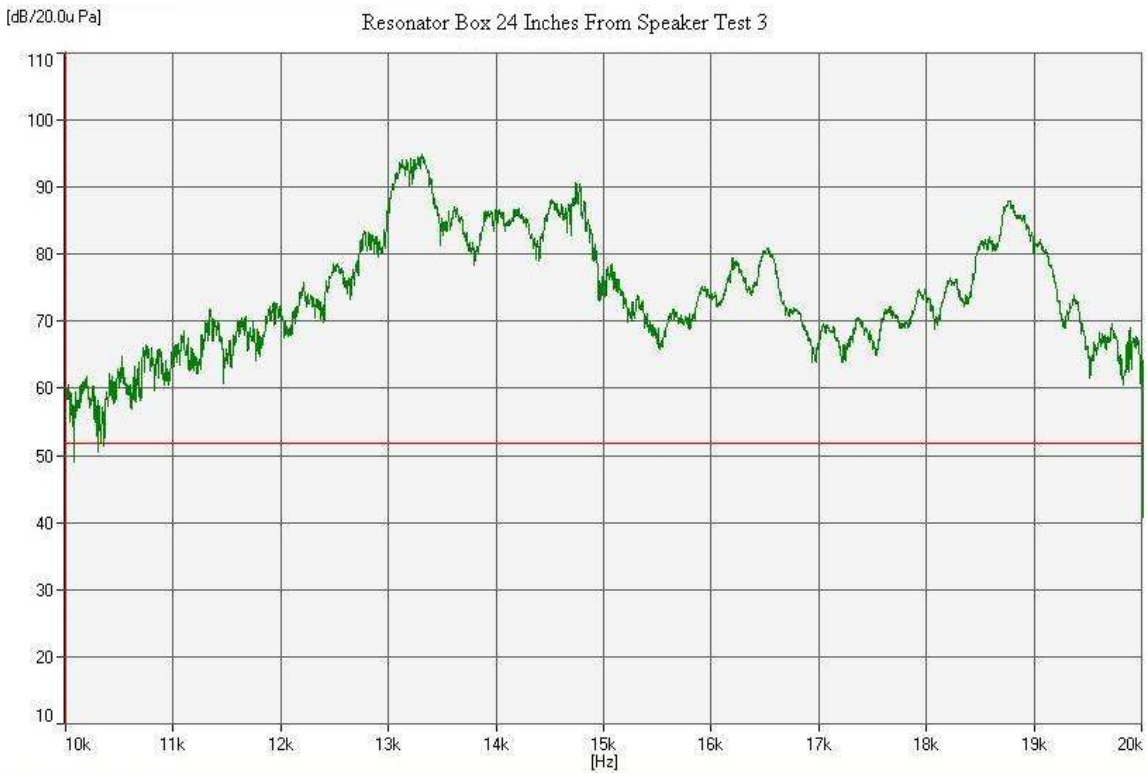

Figure 5.31: Resonator box 24 inches from sound source test 3

Figure 5.32: Resonator box 36 inches from sound source test 3

Figure 5.33: Resonator box 48 inches from sound source test 3

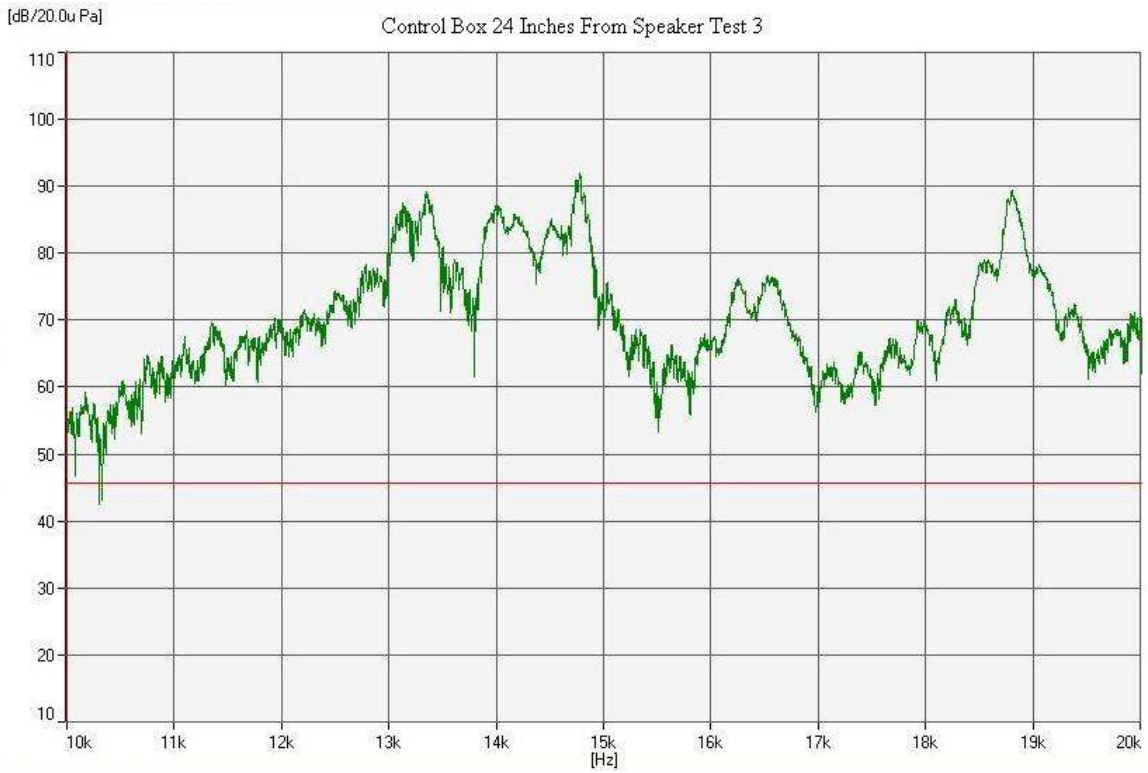

Figure 5.34: Control box 24 inches from sound source test 3

Figure 5.35: Control box 36 inches from sound source test 3

Figure 5.36: Control box 48 inches from sound source test 3

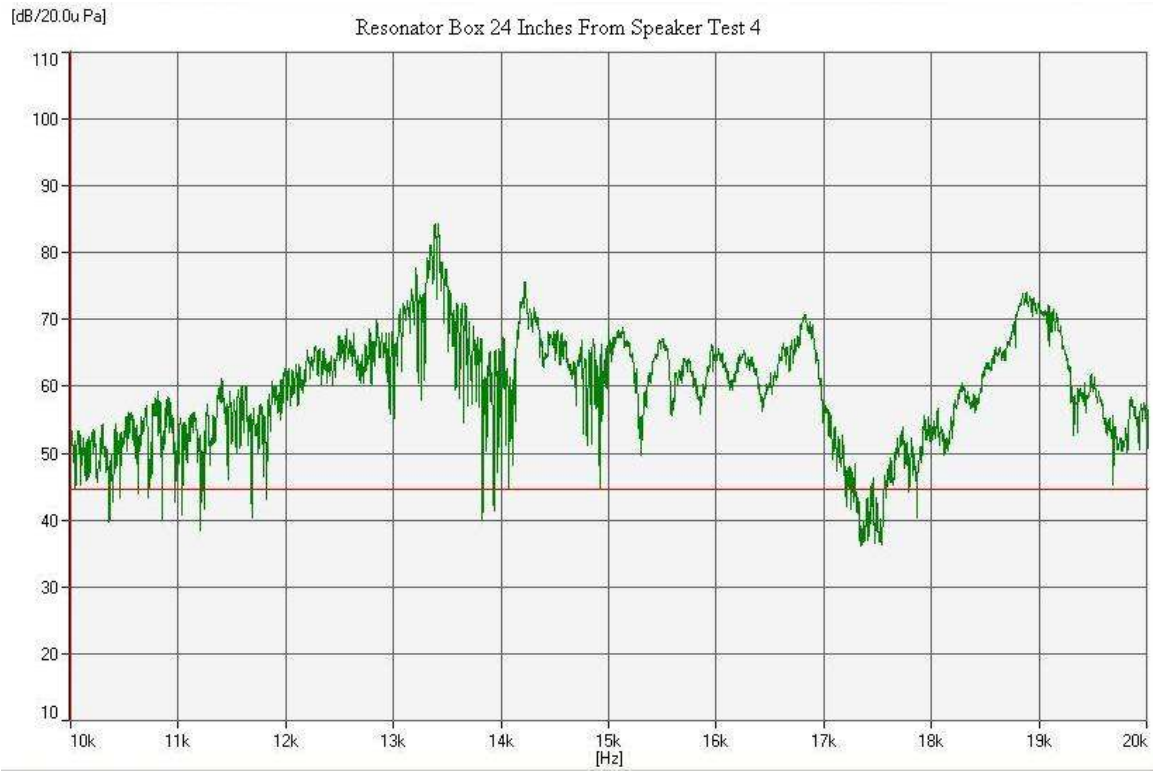

Figure 5.37: Resonator box 24 inches from sound source test 4

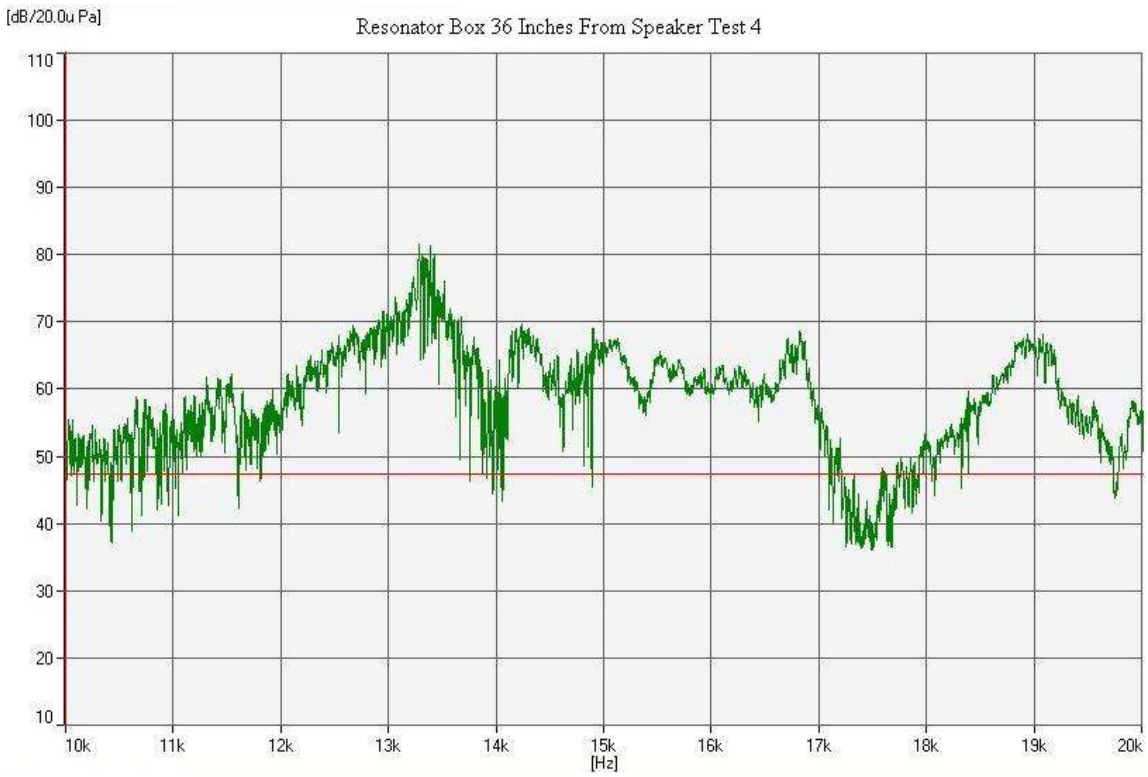

Figure 5.38: Resonator box 36 inches from sound source test 4

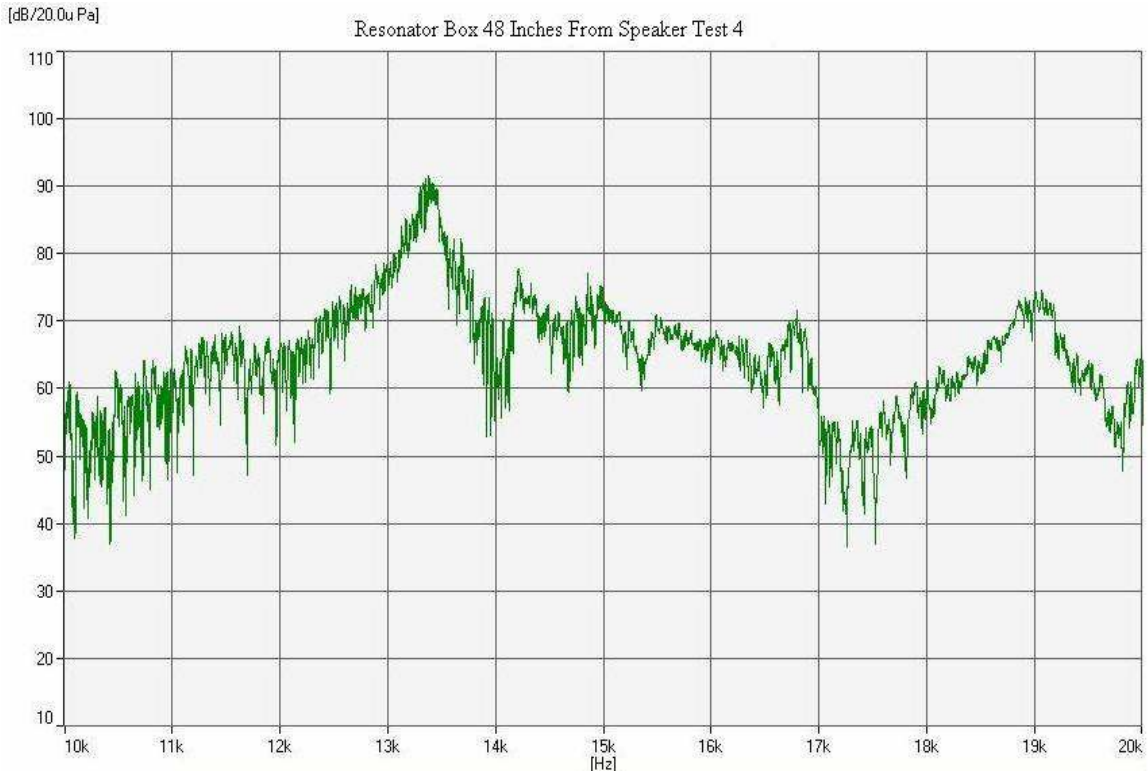

Figure 5.39: Resonator box 48 inches from sound source test 4

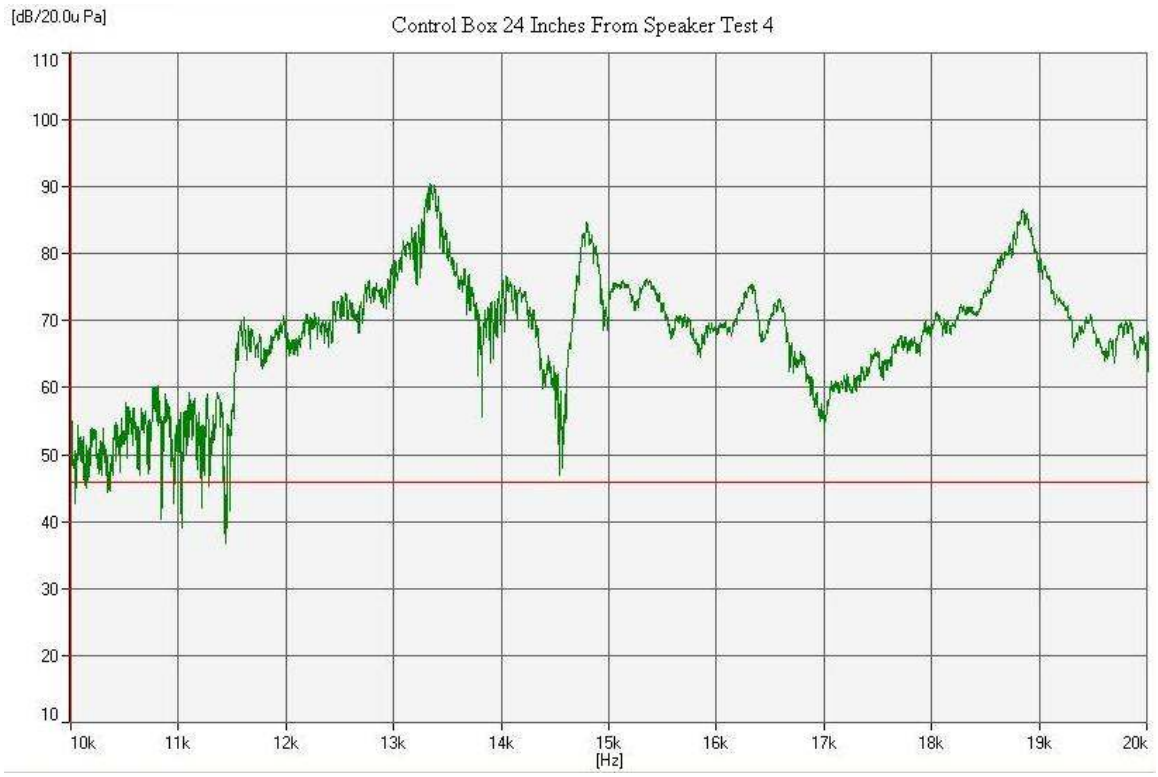

Figure 5.40: Control box 24 inches from sound source test 4

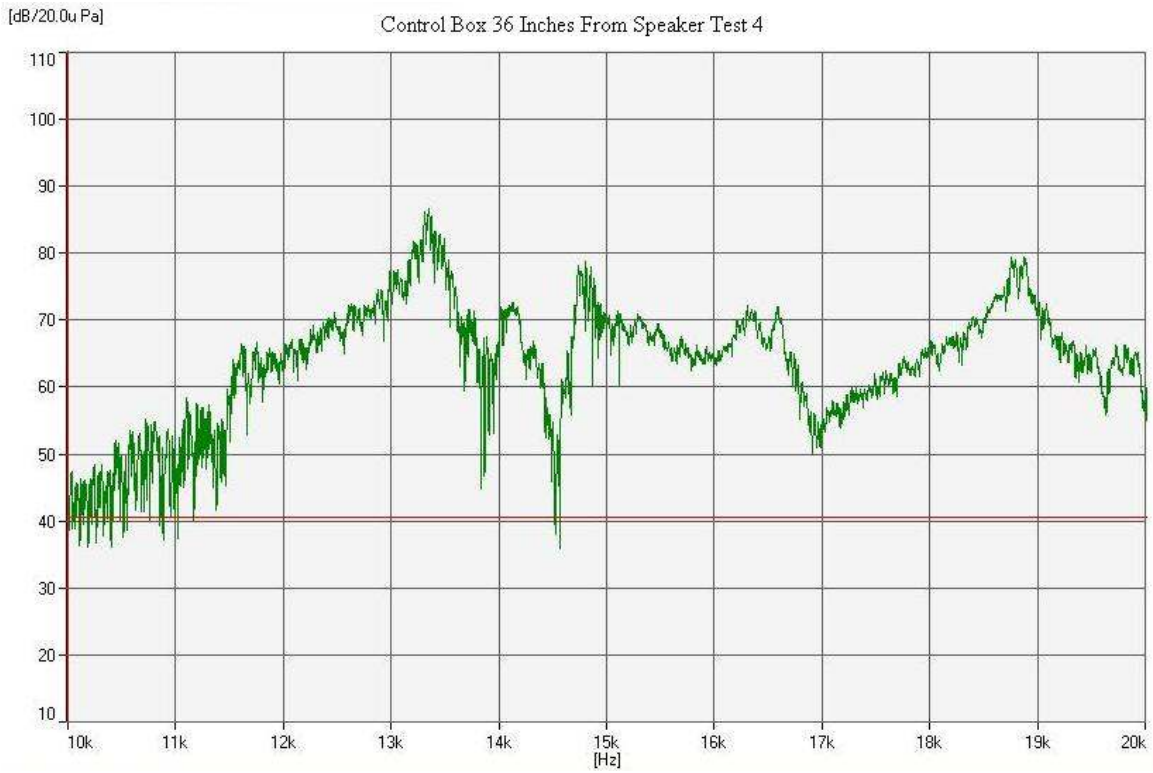

Figure 5.41: Control box 36 inches from sound source test 4

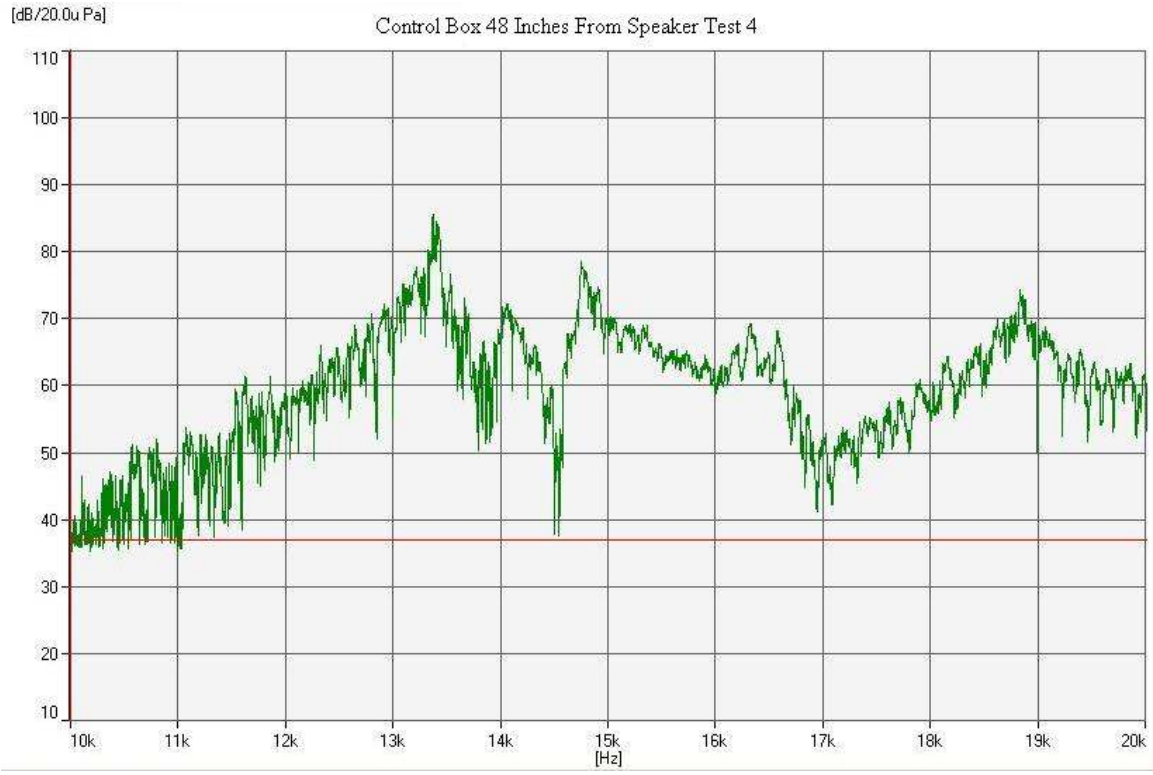

Figure 5.42: Control box 48 inches from sound source test 4

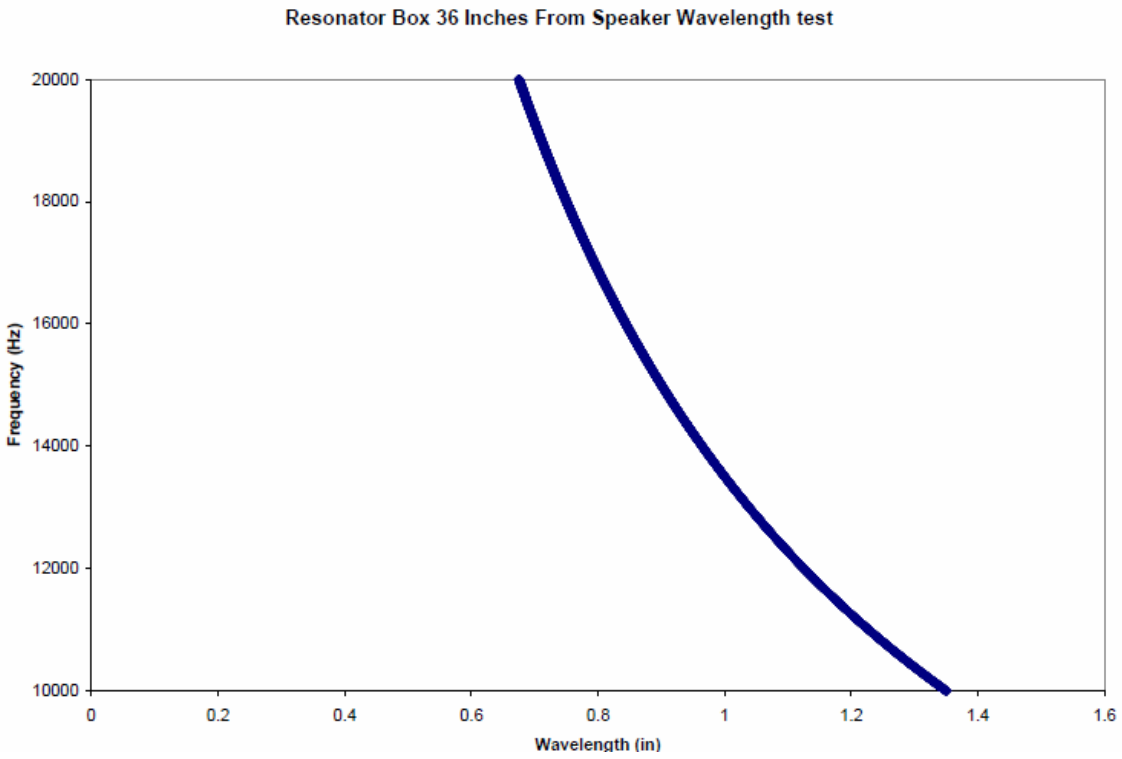

Figure 5.43: Wavelength of acoustic noise spectrum used during sine sweep tests

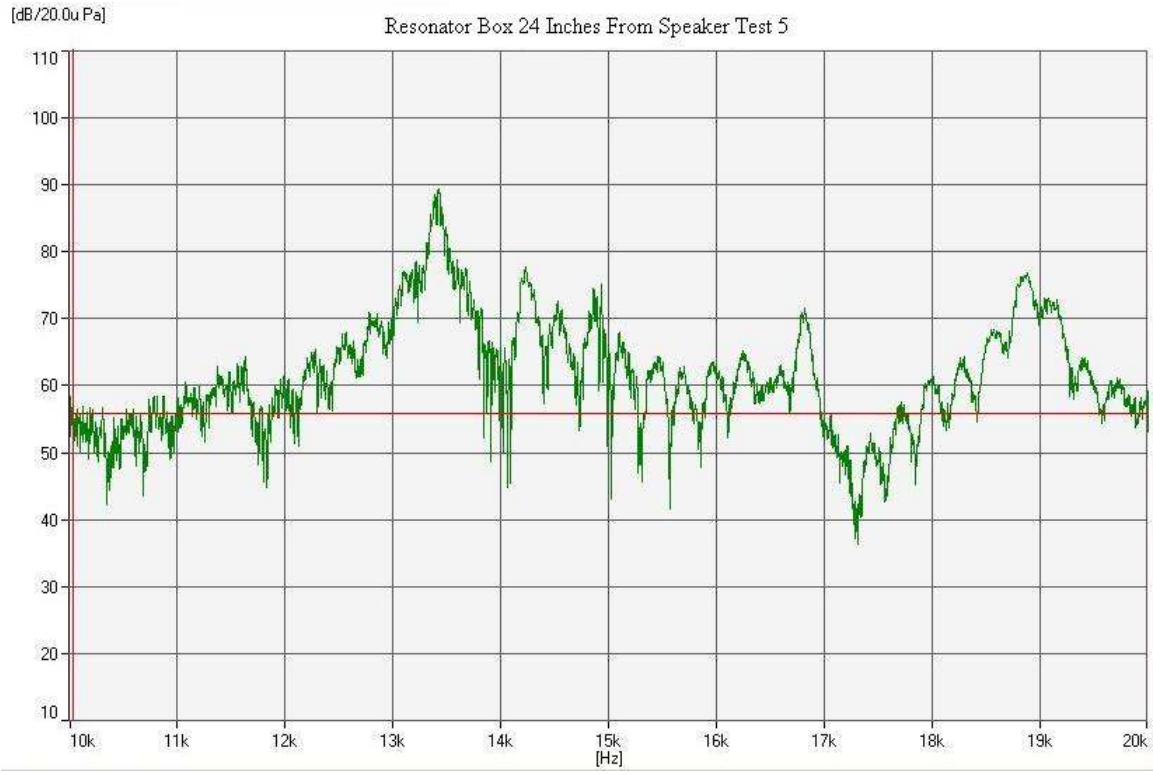

Figure 5.44: Resonator box 24 inches from sound source test 5

Figure 5.45: Resonator box 36 inches from sound source test 5

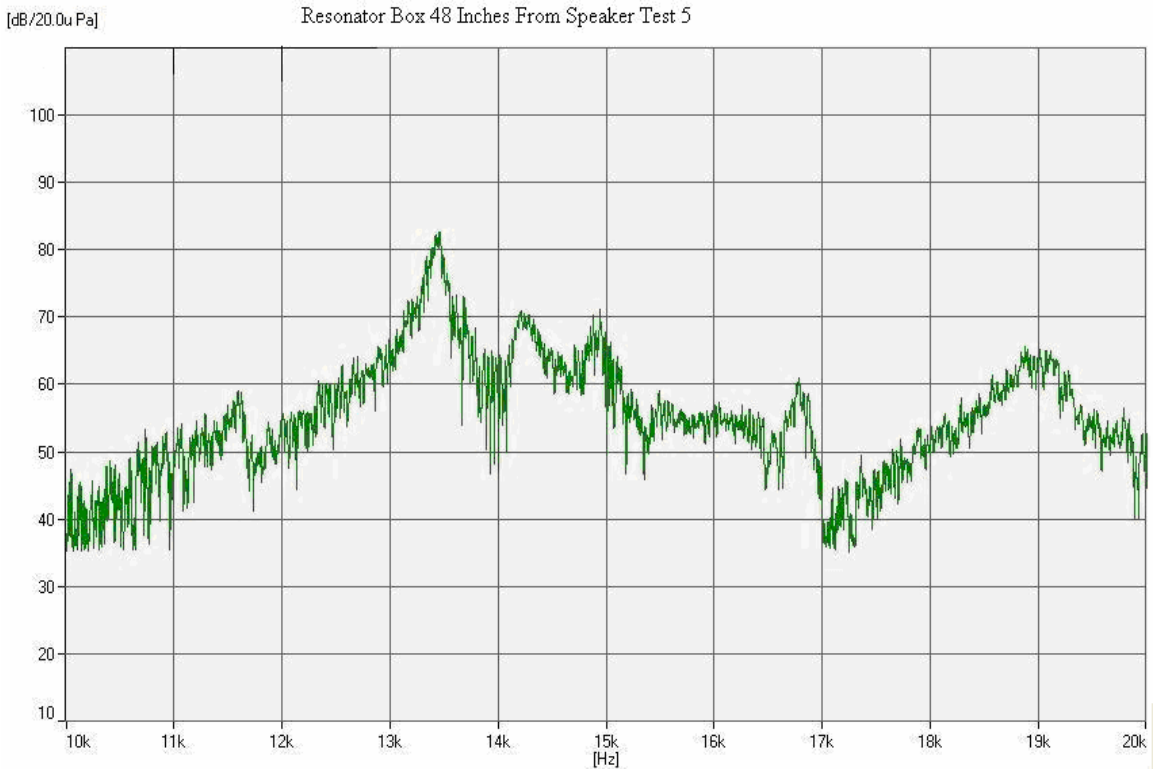

Figure 5.46: Resonator box 48 inches from sound source test 5

5.3 Determination of Resonant Frequency of the Resonator and Control Boxes

The resonant frequency of the individual resonators is important to the design and data evaluation. However, the natural frequency of the box assembly as a whole should not be neglected in data evaluation. If the box assembly natural frequency is in the same range as the testing frequencies, it will have an adverse effect on the data. To determine the natural frequency of the two boxes, the boxes were each placed on a small shaker, LDS model V408 Shaker, equipped with two Polytec Laser Vibrometers model OFV 353. The response of the box was measured by an HP 35665A Dynamic Signal Analyzer. The natural frequencies of the resonator and control boxes were found to be approximately 1200 Hz for each box. This natural frequency is well outside the testing bandwidth of 10 kHz to 20 kHz and should not have an effect on the data. The results of the vibration testing are shown in Figures 5.50 through 5.53.

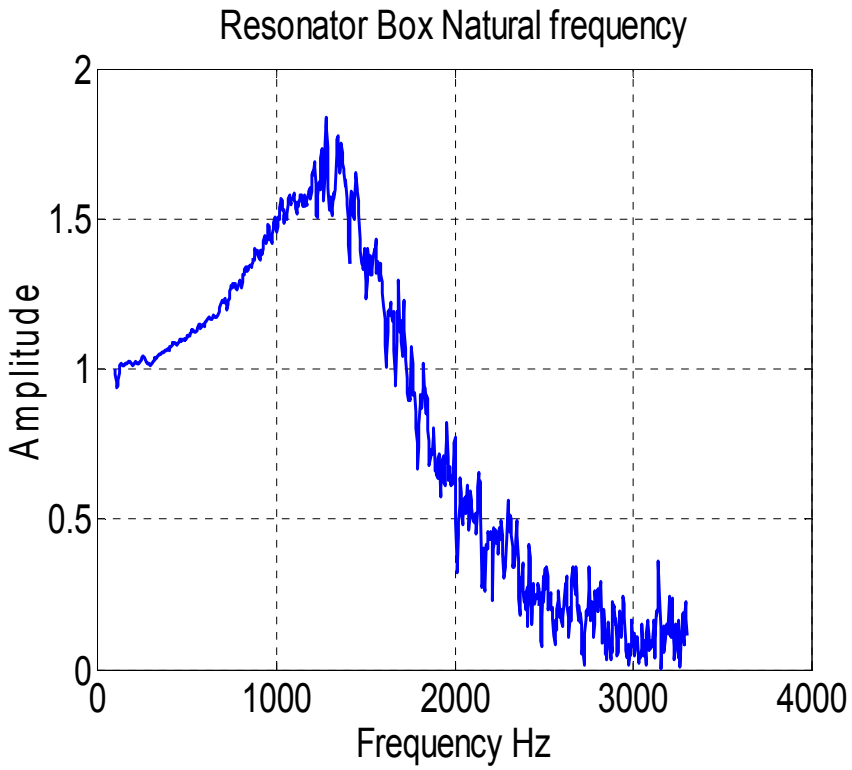

Figure 5.47: Natural frequency of resonator box from vibration testing

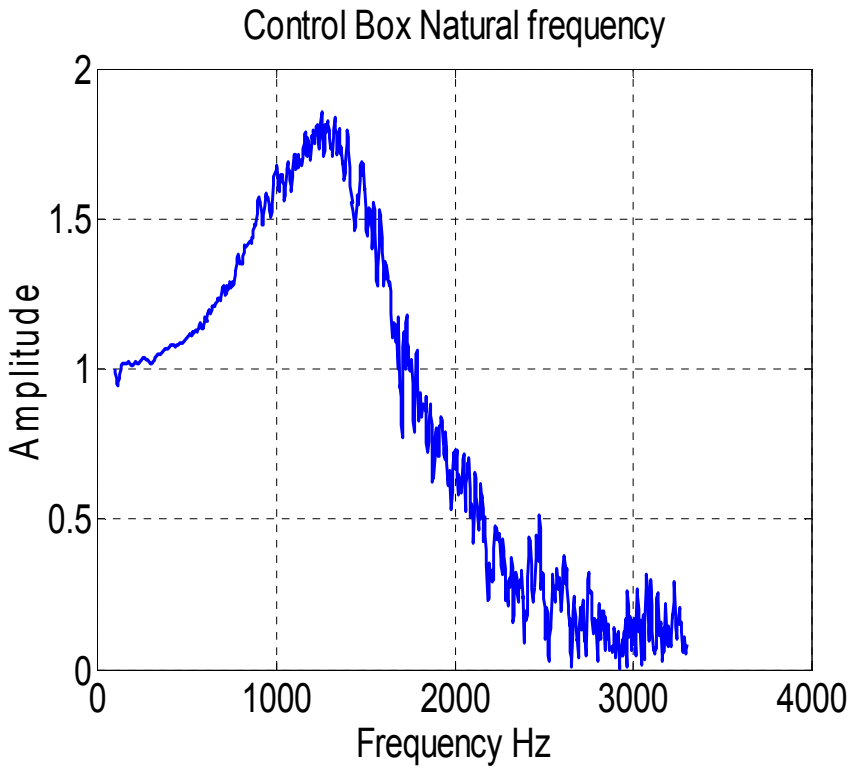

Figure 5.48: Natural frequency of control box from vibration testing

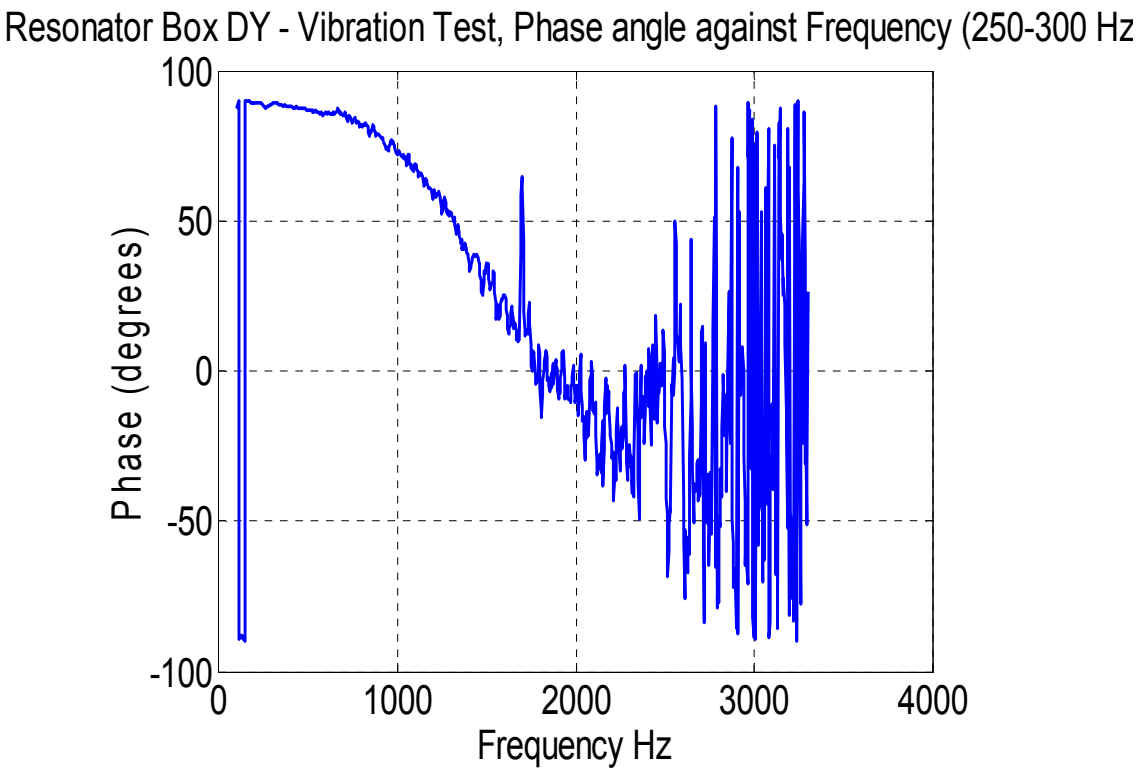

Figure 5.49: Phase angle of resonator box from vibration testing

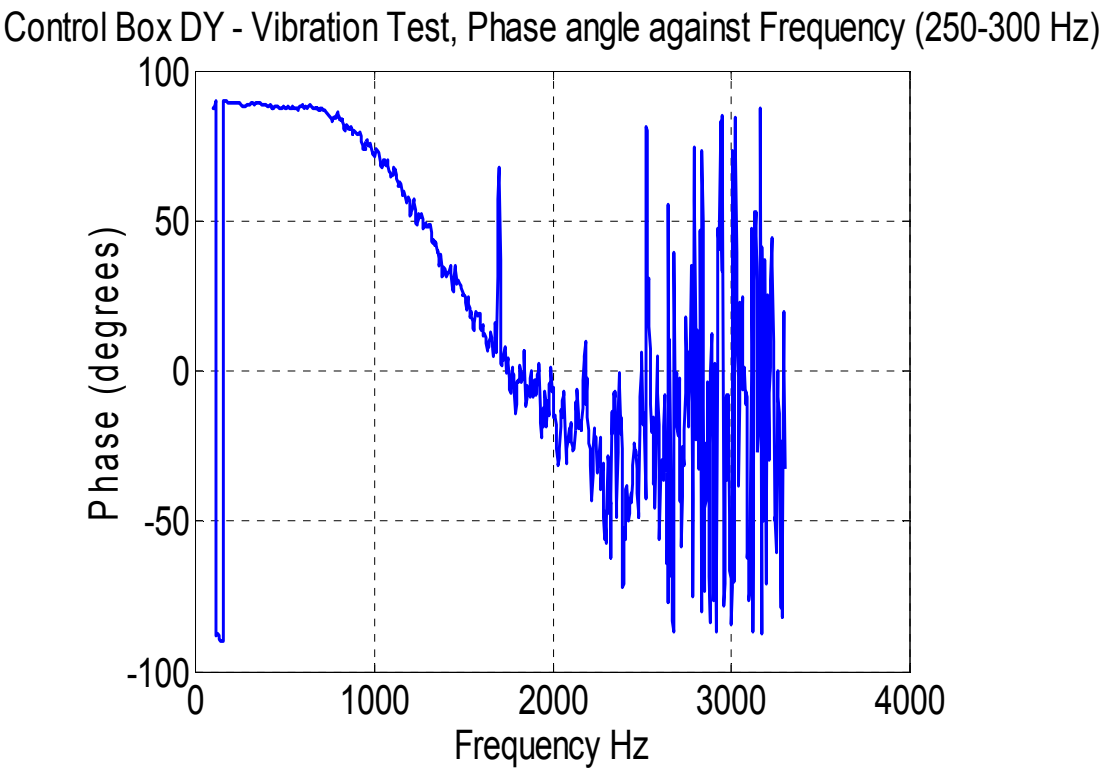

Figure 5.50: Phase angle of control box from vibration testing

Chapter 6: Conclusions and Recommendations for Future Work

An acoustic metamaterial composed of a one-dimensional array of MEMS size Helmholtz resonators was fabricated using standard microfabrication techniques. The acoustic metamaterial was fabricated on a standard four inch diameter silicon wafer in one inch squares. Each square had an array of micro Helmholtz resonators etched into the surface of the silicon. Each micro Helmholtz resonator was designed to attenuate noise at 14.5 kHz The individual squares were anodically bonded to glass to seal the cavity of the resonator, and then the individual squares were assembled into a box open on one side. This box was placed over a microphone which was subjected to high frequency and high power acoustic noise. The resonator box proved effective in attenuating noise as much as 18 dB more than the control box, which was a box of the same material and dimensions with no resonators. The bandwidth of attenuation is in the form of a notch filter with the largest attenuation occurring at approximately 14.4 kHz with gradually decreasing attenuation on either side as shown in Figure 5.1. The main goal of this research was to prove if this type of acoustic metamaterial could be designed to attenuate noise at a desired frequency and to prove if the micro sized resonators demonstrated significant attenuation. In the limited scope of this study, this theory was proven correct.

The design of the box itself played an unexpected role in the results. The dimensions of the box allowed for the creation of standing waves inside the box, which caused fatigue of the glue bonds holding the box together. This resulted in a degraded output in the effects of the resonators. In the future, the design of the box itself should be considered as well as the design of the resonators. Additionally, the physical handling of the box can cause irreparable damage to the necks of the resonators; this also could have played a role in the output degradation over

time. More testing is required to determine if this type of acoustic metamaterial will be effective at attenuating noise over long periods of time.

The acoustic metamaterial design can be refined to increase performance. Methods to increase the bandwidth and amount of attenuation should be investigated and applied. One possible method would be the pattern of the resonators. Some research has shown that the pattern of the resonators has an affect on the attenuation, such as staggered patterns or elliptical patterns of resonators instead of a standard square array. It should also be determined if the resonators can be designed to attenuate noise at another target frequency other than 14.5 kHz. Also, methods should be examined to practically package this acoustic metamaterial with a MEMS gyroscope and test in real environments. Due to hardware limitations, the testing was conducted with only one microphone. The boxes were switched between each batch of tests. Unexpectedly, it was later determined that picking the box up and replacing it caused a slight change in the response. In the future, the boxes should be tested at the same time with two microphones.

Bibliography

[1] Gad-el-Hak, M., 2001, *MEMS Handbook*, CRC Press.

[2] Dean, R., Flowers, G., Hodel, S., MacAllister, K., Horvath, R., Matras, A., Robertson, G., and Glover, R., 2002, "Vibration Isolation of MEMS Sensors for Aerospace Applications," Proceedings of the IMAPS International Conference and Exhibition on Advanced Packaging and Systems, Reno, NV, pp. 166-170.

[3] Yunker, W. N., Soobramaney, P., Black, M., Dean, R. N., Flowers, G. T., and Ahmed, A., 2011, " The Underwater Effects of High Power, High Frequency Acoustic Noise on MEMS Gyroscopes," American Society of Mechanical Engineers 2011 International Design Engineering Technical Conferences, Proceedings of the 23rd Biennial Conference on Mechanical Noise and Vibration, Washington D. C., D.C., 47180.

[4] Dean, R., Flowers, G., Sanders, N., MacAllister, K., Horvath, R., Hodel, A. S., Johnson, W., Kranz, M., and Whitley, M., 2005, "Damping Control of Micromachined Lowpass Mechanical Vibration Isolation Filters Using Electrostatic Actuation with Electronic Signal Processing," Proceedings of SPIE - The International Society for Optics and Photonics, **5760**, pp. 11-22.

[5] Dean, R. N., Flowers, G. T., Hodel, A. S., Roth, G., Castro, S., Zhou, R., Moreira, A., Ahmed, A., Rifki, R., Grantham, B. E., Bittle, D., and Brunsch, J., 2007, "On the Degradation of MEMS Gyroscope Performance in the Presence of High Power Acoustic Noise," IEEE International Symposium on Industrial Electronics, pp. 1435-1440.

[6] Castro, S., Dean, R., Roth, G., Flowers, G. T., and Grantham, B., 2007, "Influence of Acoustic Noise on the Dynamic Performance of MEMS Gyroscopes," ASME 2007 International Mechanical Engineering Congress and Exposition, Seattle, Washington, **9**, pp. 1825-1831.

[7] Burch, N. H., Black, M. N., Dean, R. N., and Flowers, G. T., 2010, "Microfibrous Metallic Cloth for Damping Enhancement in Printed Circuit Boards", Proc. SPIE 7643, 76431U.

[8] Smith, D. R., Padilla, W. J., Vier, D. C., Nemat-Nasser, S. C., and Schultz, S., 2000, "Composite Medium with Simultaneously Negative Permeability and Permittivity," The American Physical Society Physical Review Letters, **84**(18), pp. 4184-4187.

[9] Liu, Z., Zhang, X., Mao, Y., Zhu, Y. Y., Yang, Z., Chan, C. T., and Sheng, P., 2000, "Locally Resonant Sonic Materials," Science, **289**(5485), pp. 1734-1736.

[10] Fang, N., Xi, D., Xu, J., Ambati, M., Srituravanich, W., Sun, C., and Zhang, X., 2006, "Ultrasonic Metamaterials with Negative Modulus", Nature Materials, **5**, pp. 452-456.

[11] Yang, Z., Dai, H. M., Chan, N. H., Ma, G. C., and Sheng, P., 2010, "Acoustic Metamaterial Panels for Sound Attenuation in the 50–1000 Hz Regime," American Institute of Physics Applied Physics Letters, **96**(4), 041906.

[12] Panton, R. L., and Miller, J. M., 1975, "Resonant Frequencies of Cylindrical Helmholtz Resonators," Journal of the Acoustical Society of America, **57**(6), pp. 1533-1535.

[13] Chen, K. T., Chen, Y. H., Lin, K. Y., and Weng, C. C., 1998, "The Improvement on the Transmission Loss of a Duct by Adding Helmholtz Resonators," Applied Acoustics, **54**(1), pp. 71-82.

[14] Han, S. H., and Rhim, Y. C., 2009, "Noise-level Reduction of a Slim-type Optical Disk Drive Using the Idea of a Helmholtz Resonator," IEEE Transactions on Magnetics, **45**(5), pp. 2217-2220.

[15] Acar, C., and Shkel, A., 2009, *MEMS Vibratory Gyroscopes Structural Approaches to Improve Robustness,* Springer.

[16] Maluf, M., 2004, *An Introduction to Microelectromechanical Systems Engineering*, Artech House Inc.

[17] Franden, J., 1993, AIP *Handbook of Modern Sensors Physics, Designs and Applications*, American Institute of Physics Press.

[18] Beeby, S., Ensell, G., Kraft, M., and White, N., 2004, *MEMS Mechanical Sensors*, Artech House, Inc.

[19] Duwel, A., Gorman, J.,Weinstein, M., Borenstein, J., and Ward, P., 2003, "Experimental Study of Thermoelastic Damping in MEMS Gyros," Sensors and Actuators A: Physical, **103**(1-2), pp. 70-75.

[20] Hsu, T., 2002, *MEMS & Microsystems Design and Manufacture*, McGraw-Hill, pp. 121-124.

[21] Dean, R., Flowers, G., Sanders, N., Horvath, R., Kranz, M., and Whitley, M., 2005, "Micromachined Vibration Isolation Filters to Enhance Packaging for Mechanically Harsh Environments," Microelectronics and Electronic Packaging, **2**(4), pp.223-231.

[22] Brown, T. G., 2003, "Harsh Military Environments and Microelectromechanical (MEMS) Devices," Proceedings of IEEE Sensors, 2, pp. 753-760.

[23] Weinberg, M. S., and Kourepenis, A., 2006, "Error Sources in In-plane Silicon Tuning-fork MEMS Gyroscopes," Microelectromechanical Systems, **15**(3), pp. 479-491.

[24] Engheta, N., and Ziolkowski, R. W., 2006, *Metamaterials Physics and Engineering Explorations*, John Wiley & Sons.

[25] Zhang, S., 2010, "Acoustic Metamaterial Design and Applications," University of Illinois at Urbana-Champaign.

[26] Veselago, V. G., 1968, "The Electrodynamics of Substances with Simultaneously Negative Values of ε and μ," Soviet Physics Uspekhi, 10(4), pp. 509-514.

[27] Caloz, C., and Itoh, T., 2006, *Electromagnetic Metamaterials Transmission Line Theory and Microwave Applications*, John Wiley & Sons Inc.

[28] Li, J., and Chan, C. T., 2004, "Double-negative Acoustic Metamaterial," The American Physical Society Physical Review E, **70**(5), 055602.

[29] Cui, T. J., Smith, D. R., and Liu, R., 2010, *Metamaterials Theory, Design, and Applications*, Springer Science+Business Media, LLC.

[30] Premaratne, M., and Agrawal, G., 2011, *Light Propagation in Gain Media Optical Amplifiers*, Cambridge University Press.

[31] Schurig, D., Mock, J. J., Justice, B. J., Cummer, S. A., Pendry, J. B., Star, A. F., and Smith, D. R., 2006, "Metamaterial Electromagnetic Cloak at Microwave Frequencies," Science, **314**(5801), pp. 977-980.

[32] Pendry, J. B., 2000, "Negative Refraction Makes a Perfect Lense," American Physical Society Physical Review Letters, **85**(18), pp. 3966-3969.

[33] Luo, C., Johnson, S. G., Joannopoulos, J. D., and Pendry, J. B., 2003, "Subwavelength Imaging in Photonic Crystals," American Physical Society Physical Review B, 68(4), 045115.

[34] Tsakmakidis, K. L., Boardman, A. D., and Hess, O., 2007, "'Trapped Rainbow' Storage of Light in Metamaterials," Nature, **450**, pp. 397-401.

[35] Fok, L., Ambati, M., and Zhang, X., 2008, "Acoustic Metamaterials," MRS Bulletin, **33**, pp. 931-934.

[36] Yang, Z., Mei, J., Yang, M., Chan, N. H., and Sheng, P., 2008, "Membrane-Type Acoustic Metamaterial with Negative Dynamic Mass," American Physical Society Physical Review Letters, **101**(20), 204301.

[37] Ambati, M. S., 2008, "Active Plasmonics and Acoustic Metamaterials," University of California, Berkeley.

[38] Khelif, A., Aoubiza, B., Mohammadi, S., Adibi, A., and Laude, V., 2006, "Complete Band Gaps in Two-dimensional Phononic Crystal Slabs," The American Physical Society Physical Review E, **74**(4), 046610.

[39] Herbison, S., Declercq, N. F., Moiseyenko, R., and Laude, V., 2010, "Diffraction of Bulk Waves on Phononic Crystals," Proceedings of 20th International Congress on Acoustics, Sydney, Australia.

[40] Chen, H., and Chan, C. T., 2007, "Acoustic Cloaking in Three Dimensions Using Acoustic Metamaterials," American Institute of Physics Applied Physics Letters, **91**(18), 183518.

[41] Zhang, S., Xia. C., and Fang, N., 2011, "Broadband Acoustic Cloak for Ultrasound Waves," American Physical Society Physical Review Letters, **106**(2), 024301.

[42] Zhang, S., Yin, L., and Fang, N., 2009, "Focusing Ultrasound with an Acoustic Metamaterial Network," American Physical Society Physical Review Letters, **102**(19), 194301.

[43] Li, J., Fok, L., Yin, X., Bartal, G., and Zhang, X., 2009, "Experimental Demonstration of an Acoustic Magnifying Hyperlens," Nature Materials, **8**, pp. 931-934.

[44] Kinsler, L., Frey, A., Coppens, A., and Sanders, J., 2000, *Fundamentals of Acoustics 4th Edition*, John Wiley & Sons.

[45] Strutt, C. R., 1964, "The Optics Research of Robert John Strutt, fourth Baron Rayleigh," Applied Optics, **3**(10), pp. 1113-1113.

[46] Sugimoto, N., Masuda, M., Hashiguchi, T., and Doi, T., 2001, "Annihilation of Shocks in Forced Oscillations of an Air Column in a Closed Tube," Journal of the Acoustical Society of America, **110**(5), pp. 2263-2266.

[47] Raghunathan, R. S., Kim, H. D., and Setoguchi, T., 1998, "Impulse Noise and its Control," Progress in Aerospace Sciences, **34**(1), pp. 1-44.

[48] Tayong, R., Dupont, T., and Leclaire, P., 2010, "On the Variations of Acoustic Absorption Peak with Particle Velocity in Micro-perforated Panels at High Level of Excitation," Journal of the Acoustical Society of America, **127**(5), pp. 2875–2882.

[49] Konishi, S., Yoda, M., Sugiyama, S., and Akishita, S., 2000, "Tunable Acoustic Absorber Using a Micro Acoustic Hole Array," Electronics and Communications in Japan (Part II: Electronics), **83**(1), pp. 1-6.

[50] Müller, M. O., Bernal, L. P., Moran, R. P., Washabaugh, P. D., Parviz, B. A., Allen Chou T. A., Zhang, C., and Najafi, K., 2000, "Thrust Performance of Micromachined Synthetic Jets," American Institute of Aeronautics and Astronautics, Denver, CO, 2000-2404.

[51] http://www.bksv.com/doc/Bp0100.pdf

Appendix A: User Guide

Appendix A contains a user guide for conducting the acoustic tests described in this thesis.

Test Setup

The acoustic testing was performed in the acoustic isolation chamber in Wilmore laboratory. The test setup and hardware are all described in detail in chapter four of this thesis. Once the microphones and speakers are setup as shown in chapter four, the speaker VHF-100 Driver made by Community Speakers, is connected directly to the Crown XTi-1000 Amplifier. Only one of the two Crown XTi-1000 Amplifiers was used for this experiment because only one speaker was used for this experiment. It should be noted that the programming has been altered on the bottom amplifier, for this reason I used only the top amplifier. A former graduate student had to reprogram the amplifier for it to perform correctly.

The microphone used was a Brüel & Kjaer type 4135 and it was connected directly to the Brüel & Kjaer type 2827-002 shown below in Figure A.1. The connection for the microphones is the black connection on the left side of the Brüel & Kjaer type 2827-002. The blue Ethernet cable connects the Brüel & Kjaer type 2827-002 to the laptop shown in Figure A.2. For this experiment, only one connection was necessary. The port that each microphone was plugged into was programmed into the software package shown below in Figure A.3. The program written for this experiment is called “two mics” and it is saved on the desktop of the laptop shown in Figure A.2. This laptop belongs to Dr. Crocker’s graduate student, Wesley Smith, and is kept in the

acoustics laboratory in Wilmore. The software package, Brüel & Kjaer PULSE Labshop version 10.1, was used to collect the acoustic test data is shown in Figure A.3.

Figure A.1: Brüel & Kjaer type 2827-002 on top of two Crown XTi-1000 Amplifiers

Figure A.2: Laptop that contains Brüel & Kjaer PULSE Labshop software

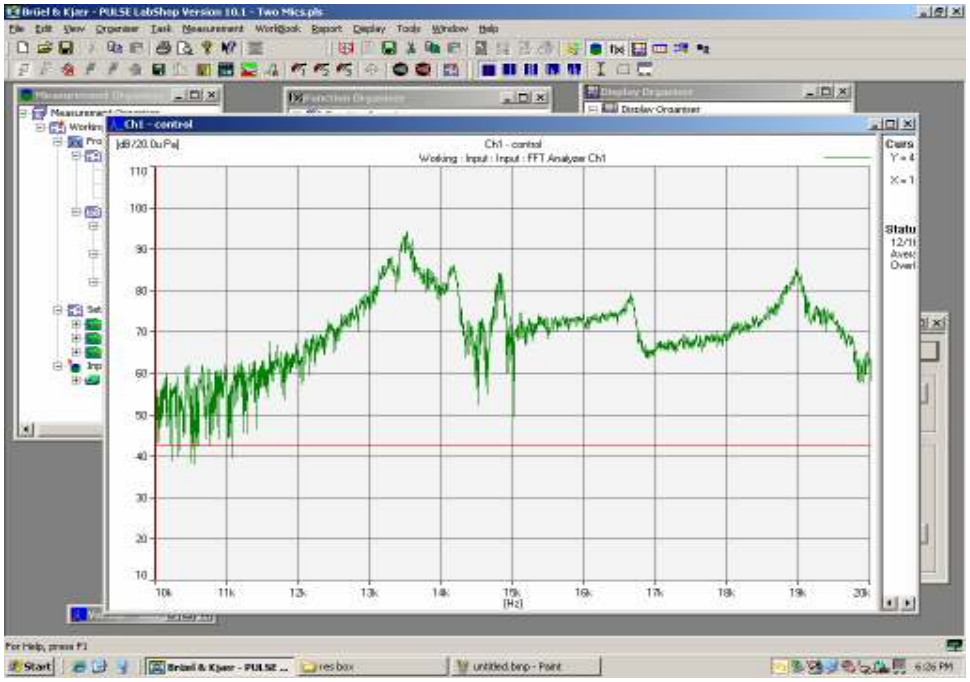

Figure A.3: Brüel & Kjaer PULSE Labshop version 10.1 software

Brüel & Kjaer PULSE Labshop

The software program is saved on the computer for reference under the name "two mics," although ironically only one microphone was used for this experiment. However, the experiment was originally designed for two, and the program is written to accommodate two microphones. To gather data using this program, simply open the "two mics" file and click the start button as shown in Figure A.4. Click the stop button when the data is done recording as shown in Figure A.5. Figure A.6 shows were the preferences for data collection can be altered by right clicking on FFT Analyzer and selecting properties. The data collection allows for three types: Exponential, Linear, and Peak. For the sine sweep data collection, the Peak option was chosen. The two channels under setup correspond to the two microphones that were intended to be used, however only one microphone was used for these tests.

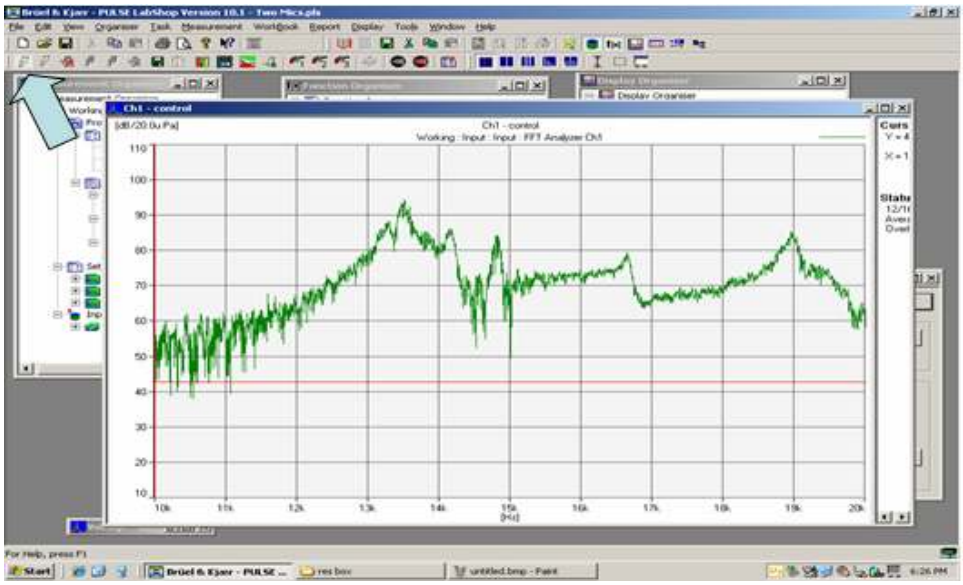

Figure A.4: Start button for Brüel & Kjaer PULSE Labshop

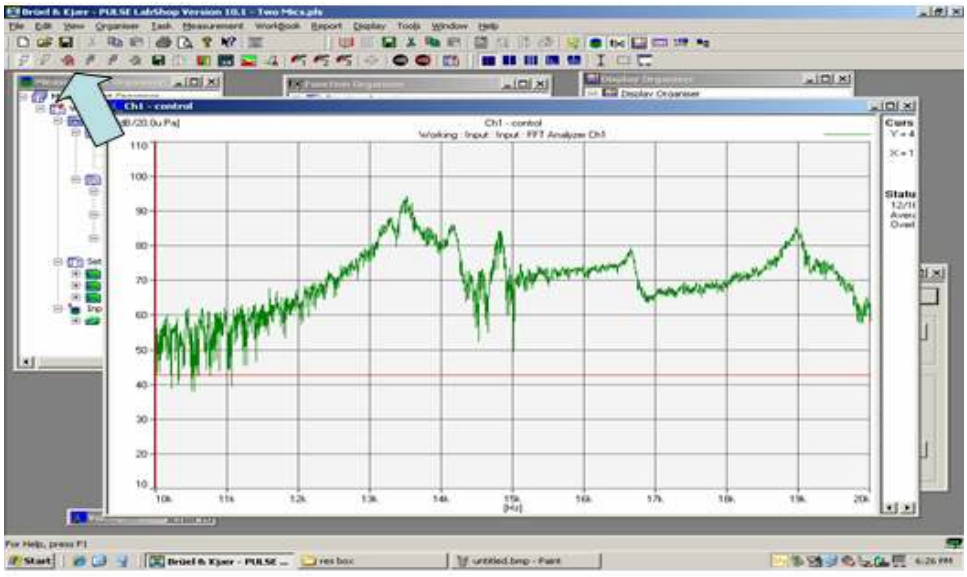

Figure A.5: Stop button for Brüel & Kjaer PULSE Labshop

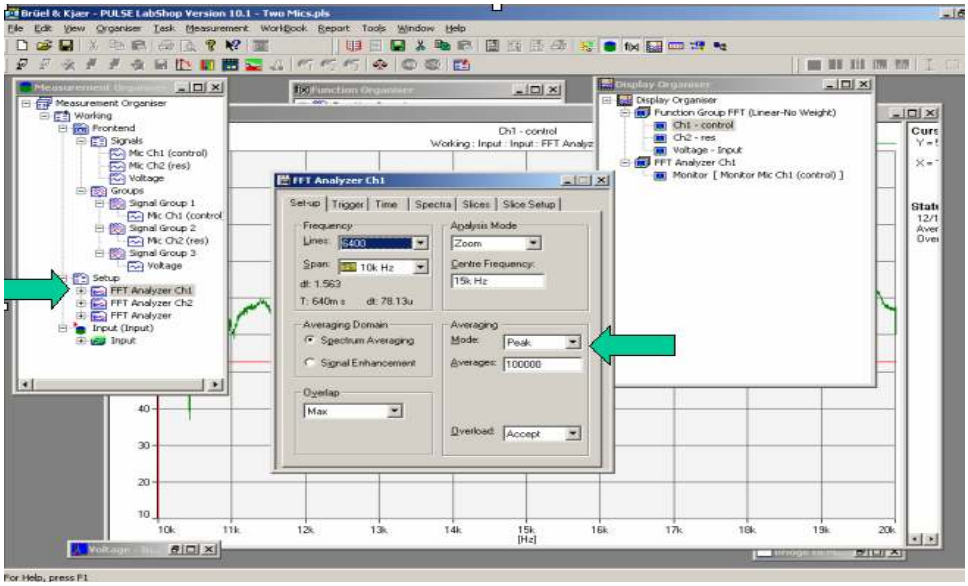

Figure A.6: Preferences for data collection can be changed here

NCH Tone Generator

Information on the NCH Tone Generator is shown in the manual for gyroscope testing that is kept near the computers in the acoustics laboratory in Wilmore. The NCH Tone Generator is connected directly to the sound card of the computer and is then connected directly to the Crown XTi-1000 Amplifiers. For the purposes of this experiment, only the sine sweep function was used for data collection. The sine sweep tone is shown below in Figure A.7. The frequencies and duration can be changed by double clicking on the values. The arrow shows where the tone can be changed. Tone selections include continuous, sine sweep, white noise, and many other types of noise. The NCH Tone Generator software is kept on the desktop of the computer directly to the right of the laptop shown in Figure A.2.

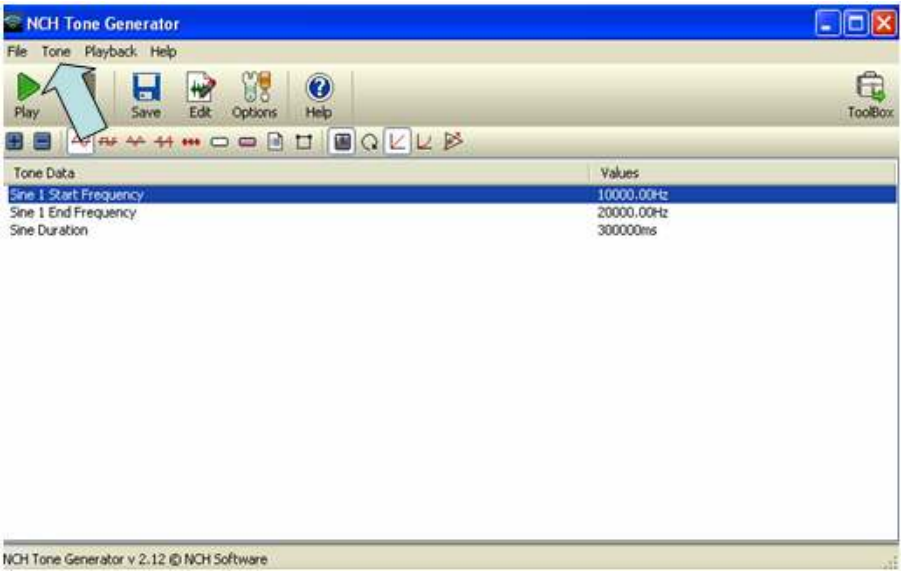

Figure A.7: NCH Tone Generator software